DIPARTIMENTO DI INGEGNERIA INDUSTRIALE

Dottorato di Ricerca in Ingegneria Meccanica

X Ciclo N.S. (2008-2011)

"Optimization of SI and CI engine control strategies via integrated simulation of combustion and turbocharging"

Ing. Ivan Criscuolo

Il Tutor

Ch.mo Prof. Ivan Arsie

Il Coordinatore

Ch.mo Prof. Vincenzo Sergi

Table of contents

Index of figures

Index of tables

CHAPTER 1

Introduction

Combustion engines have been for a long time the most important prime mover for transportation globally. A combustion engine is simple in its nature; a mix of fuel and air is combusted, and work is produced in the operating cycle. The amount of combusted air and fuel controls the amount of work the engine produces

The engine work has to overcome friction and pumping losses, and a smaller engine has smaller losses and is therefore more efficient. Increasing engine efficiency in this way is commonly referred to as downsizing. Downsizing has an important disadvantage; a smaller engine cannot take in as much air and fuel as a larger one, and is therefore less powerful, which can lead to less customer acceptance.

By increasing the charge density the smaller engine can be given the power of a larger engine, and regain customer acceptance. A number of charging systems can be used for automotive application, e.g. supercharging, pressure wave charging or turbocharging. Turbocharging has become the most commonly used charging system, since it is a reliable and robust system, that utilizes some of the energy in exhaust gas, otherwise lost to the surroundings.

There are however some drawbacks and limits of a turbocharger. The compressor of a single stage turbo system is sized after the maximum engine power, which is tightly coupled to the maximum mass flow. The mass flow range of a compressor is limited, which imposes limits on the pressure build up for small mass flows and thereby engine torque at low engine speed. Further, a turbo needs to spin with high rotational speed to increase air density, and due to the turbo inertia it takes time to spin up the turbo. This means that the torque response of a turbocharged engine is slower than an equally powerful naturally aspirated engine, which also lead to less customer acceptance

A two stage turbo system combines two different sized turbo units, where the low mass flow range of the smaller unit, means that pressure can be increased for smaller mass flows. Further, due to the smaller

inertia of the smaller unit, it can be spun up faster and thereby speed up the torque response of the engine. The smaller unit can then be bypassed for larger mass flows, where instead the larger turbo unit is used to supply the charge density needed [71].

1.1 Generalities on engine modeling

In the past years, the recourse to experimental analyses on the test bench was the only way to design an engine, analyze the pollutant emissions and develop engine control strategies. This method laid heavy in terms of human resources, facilities and time and, then, on the development costs. These aspects influenced both the final cost on the customer and the product time-to-market.

Starting from the need of limiting time and costs, the engine models have been developed to estimate engine performances and pollutant emissions with a narrow set of experimental data. The use of mathematical models in an automotive control system is gaining increased interest from the industry. This increased interest comes from the complex engine concepts used, where additional actuators and degrees of freedom are added to the systems. Model based control is proposed as a way of handling the increased complexity.

According to the description of phenomenon, the use of experimental data and computational time, the models can be classified into:

- White box
- Grey box
- Black box

The white box models are based on the resolution of partial differential equations (PDE) and the need of experimental data is very limited. This means that the white box models are untied from engine geometry and characteristic with an high degree of generalization. The drawback is the high computational effort, therefore only steady state condition can be simulated with these kind of models.

The black box models use a large number of experimental data in order to make up to the lack of a physical mathematical description. The benefit of the black box models is the limited computational demand.

Thank to this peculiarity, they are suitable for real-time applications such as on-board and ECU implementation.

The gray box models are the right settlement between the generalization of white box models and the fast computational time of black box models: they merge the experimental and physical information about the process. They are frequently used for the engine control tuning, assumed a given geometry.

The choice about the model to be used derives from the kind of engine under test. Indeed the most critical phenomena to model are different depending on the fuel, the modality of combustion and the presence of the turbocharger.

For a compression ignition engine (CI), especially for a Common Rail multiple injection Diesel engine, the attention has to be focused on the combustion phase and on the in-cylinder events because they are the most critical phenomena in the engine cycle. The reason consist in the modality of the mixture formation. Almost all the modern Diesel engines adopt the direct injection: the fuel is injected directly in the combustion chamber and the air turbulence has to provide the sufficient energy for the mixture before reaching the flammability conditions. In a Multijet engine, there are several injection per engine cycle (till 8 per cycle in the Multijet II system). The first interesting effect is that the composition in the combustion chamber cannot be considered homogeneous. Furthermore the ignition timing cannot be decided and determined a priori. It is evident that, in order to have a good estimation of the engine cycle, the phenomena above described must be modeled with an high degree of physical concepts.

In a spark ignition engine (SI) with indirect fuel injection, the combustion is easiest to simulate because the mixture come in the combustion chamber already mixed and its composition can be assumed homogenous. Besides the combustion starts depending on the sparking plug timing. The most common used combustion models are based on quasi-dimensional approach, with semi-empirical Wiebe law for the heat release rate simulation. For these engines the inertia and dynamic effects in intake and exhaust systems have greater influence. One-dimensional models of gas dynamics, representing the flow and the heat transfer in the piping and in the other components of the engine system are often used for SI engine simulation.

The recent years have seen the extension of the superchargers system

(mostly turbochargers) also to smaller engines equipping the city cars. This justifies the increasing interest of manufacturers about turbochargers and the development of a wide numbers of turbocharger models.

1.2 Combustion modeling

The combustion models can be divided in three categories: zero-dimensional models, quasi-dimensional models and multi-dimensional models [19][33][88][98].

The zero-dimensional models or single zone models suppose that at any time the composition and the temperature of the in-cylinder gases are uniform. These kind of models are able to forecast very well the performances of the engine with a low computational effort as shown in [8][14][17][18][113]. Nevertheless they are not suitable for the estimating of the gradients of gas composition and temperature in the combustion chamber, which are fundamentals for the pollutant emissions calculation.

In opposition to the zero-dimensional models, there are the multi-dimensional models, in which the differential equations, that describe the in-cylinder fluid motion, are solved by using very fine grids. However, some processes are still simulated by means of phenomenological submodels and the simulation results are strongly influenced by the used calibration parameters. Consequently, it is not possible guarantee for each operating condition an adequate level of accuracy. In addition, the computational time and memory request impose the application only for the design of the combustion chamber and not for the definition of control strategies.

In the middle there are the quasi-dimensional models. They combine the benefit of both types of models, through the resolution of balance equations of mass and energy without explicitly integrating the balance equations of momentum. These models are able to provide information about the spatial distribution of temperature and composition of in-cylinder gases with lower detail than multi-dimensional but with a much lower computational burden. Over the years several quasi-dimensional models have been developed with only two zones ([7] e [91]) up to models with more than one hundred zones ([63], [14], [70] e [86]). These models, as well as the number of zone, differ in the level of detail and

accuracy of the submodels used in the description of processes of penetration, atomization, evaporation, mixing and combustion. Some multi-zone models simulate the mixing and subsequent burning without considering the dynamics of the spray ([68] e [77]). For example, in [68], an instantaneous vaporization of the fuel injected into the cylinder is assumed. Other models, such as that proposed in [77], consider the processes of atomization and evaporation so rapid compared to the mixing that can be neglected: the spray is described as a jet of steam and the liquid phase is not considered. Strictly speaking, the processes of atomization and evaporation can be neglected only if the in-cylinder conditions are close to the fuel critical point. Therefore, it is not possible to apply this type of models in a wide range of engine operation. One of the most advanced multi-zone models is undoubtedly the one proposed by Hiroyasu and Katoda ([63]) and later taken by Jung and Assanis ([67]), where the spray is divided into many zones, both along the axial and radial direction, simulating the time evolution of each of them. The angle formed at the base of the spray penetration, the Sauter mean diameter and the breakup length are simulated using experimental correlations obtained through studies in environments with constant pressure. In addition, the effect of swirl motion and the collision of the jet with the cylinder walls is considered through appropriate empirical coefficients. An important point has to be taken in account: in the latest generation of Diesel engines, the fuel injection pressure and the in-cylinder pressure and temperature at the time of injection are significantly higher than those considered in these models. It should be noted that among the mentioned multi-zone models, there are few examples of combustion submodels that can simulate adequately both the diffusive and premixed combustion. For example, in the model proposed in of Ramos J. I.[92], the burning rate depends on the amount of air incorporated during the premixed combustion without taking into account the mixing. Many works, as [63] and [118], assume that the fuel burns in a stoichiometric mixture. These models overestimate the temperature in the combustion chamber and therefore overestimate the NO_x emissions. In addition, they are extremely sensitive to the amount of entrained air which is often calibrated appropriately through coefficients that take values very different among the different authors [67]. At last, in other works ([23]) the combustion submodel is based on a turbulent simplified approach, in order to take into account the effect that the mixing has on the combustion. Many Multi-zone models do not consider

radiative heat exchange ([63] and [118]): its contribution to the overall heat transfer may vary significantly (5 ÷ 50%) [62].

In almost all multi-zone models the emissions of NO_x and SOOT are estimated using, respectively, the well-known Zeldovich mechanism ([62]) and the formation mechanism of oxidation proposed by Hiroyasu et al. [63]. In some recent works the oxidation model proposed by Nagle and Strickland-Constable was also applied [67][88].

1.3 Turbocharger performance representation

State-of-the-art analyses on turbocharger modeling, as the one proposed in [71], evidence that turbocharger performances are usually presented through maps based on corrected variables. The corrections are important, since the performance maps are otherwise only valid for the conditions under which they were measured. The basis for the corrections is the dimensional analysis [106] and the correction equations relevant for a turbochargers are presented in [38][76][115]. The correction equations scale the turbine and compressor performance variables, based on the current inlet temperature and pressure. An experimental investigation of the correction quantities for the compressor is presented in [75]. There are standards describing the procedures involved in measuring a turbo map, see [95][96][13][31]. The definition of when surge occurs, which gives the smallest mass flow point for a corrected compressor speed, have been discussed in recent works [1][47]. A summary of some different turbocharger test facilities is presented in [47]. Methodology to measure turbo performance on an engine in a test stand is presented in [73].

1.3.1. Compressor map

There are four performance variables for the compressor map: corrected mass flow, pressure ratio, corrected shaft speed and adiabatic efficiency. The corrected compressor mass flow is given by the eq. (1.1)

$$\dot{m}_{c,corr} = \dot{m}_c \frac{\sqrt{\frac{T_{01}}{T_{c,std}}}}{\frac{p_{01}}{p_{c,std}}} \tag{1.1}$$

where $\dot{m}_c$ is the compressor mass flow, T_{01} is the compressor inlet temperature, and p_{01} is the compressor inlet pressure. The temperature $T_{c,std}$ and the pressure $p_{c,std}$ are the reference states. The reference states must be supplied with the compressor map, since these states are used to correct the performance variables. The compressor pressure ratio is given by the eq. (1.2)

$$\Pi_c = \frac{p_{02}}{p_{01}} \tag{1.2}$$

where p_{02} is the compressor outlet pressure. The corrected shaft speed is defined as eq. (1.3)

$$N_{c,corr} = N_{tc} \frac{1}{\sqrt{\frac{T_{01}}{T_{c,std}}}} \tag{1.3}$$

where N_{tc} is the turbo shaft speed. The adiabatic efficiency of the compressor is defined as eq. (1.4)

$$\eta_c = \frac{\left(\frac{p_{02}}{p_{01}}\right)^{\frac{\gamma_c - 1}{\gamma_c}} - 1}{\frac{T_{02}}{T_{01}} - 1} \tag{1.4}$$

where γ_c is the ratio of specific heats for air. The adiabatic efficiency describes how efficient the compression of the gas is, compared to an ideal adiabatic process. Or in other words, how much the pressure increases, compared to how much the temperature increases. Points measured with equal $N_{c,corr}$ are connected in the compressor map, and

are referred to as speed lines. A speed line consists of a number of measurements of Π_c and $\dot{m}_{c,corr}$ and gives the characteristics of the compressor. Compressor efficiency η_c is also measured for each point, and contours of constant η_c are normally superimposed over the speed lines. The mass flows measured on each speed line range from the surge line into the choke region. An example of a compressor map is shown in Figure 1.1

The surge line is the boundary of stable operation of the compressor. A compressor will enter surge if the mass flow is reduced below this point. Surge is an unstable condition, where the mass flow oscillates. These oscillations can destroy the turbo. Compressor choke is found for high mass flows, and indicates that the speed of sound is reached in some part of the compressor. Measurements are conducted at different $N_{c,corr}$ up to the maximum allowable, and mechanical failure of the turbo can result if the speed is increased further.

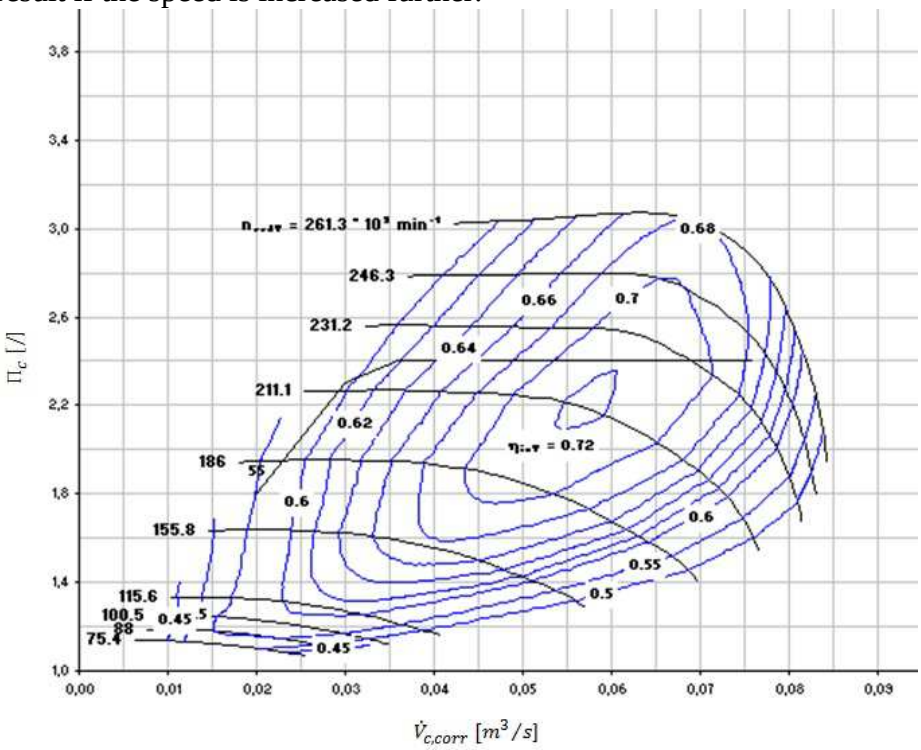

Figure 1.1 Example of compressor map

1.3.2. Turbine map

As for the compressor map, there are four performance variables used in the turbine performance map: corrected mass flow, expansion ratio, corrected speed and adiabatic efficiency. It is further common to define two more variables for the turbine: turbine flow parameter and turbine speed parameter. The corrected turbine mass flow is given by the eq. (1.5)

$$\dot{m}_{t,corr} = \dot{m}_t \frac{\sqrt{\frac{T_{03}}{T_{c,std}}}}{\frac{p_{03}}{p_{c,std}}} \tag{1.5}$$

where $T_{c,std}$ and $p_{c,std}$ can be other standards states, than are used in the compressor maps. The turbine mass flow $\dot{m}_t$ is the combustion products and thus normally the sum of fuel and air. The pressures p_{03} and p_{04} are the turbine inlet and outlet pressure, respectively, and T_{03} and T_{04} are the turbine inlet and outlet temperature, respectively. It is common to neglect the standard states in eq. (1.5), and present turbine data using the turbine flow parameter or TFP

$$TFP = \dot{m}_t \frac{\sqrt{T_{03}}}{p_{03}} \tag{1.6}$$

The turbine expansion ratio is given by the eq. (1.7)

$$\Pi_t = \frac{p_{03}}{p_{04}} \tag{1.7}$$

Some authors prefer to have the pressure after the component divided by the pressure before, as is the case for the compressor pressure ratio, as eq. (1.2). The corrected turbine shaft speed is given by the eq. (1.8)

$$N_{t,corr} = N_{tc} \frac{1}{\sqrt{\frac{T_{03}}{T_{t,std}}}} \tag{1.8}$$

It is common to neglect T_{std} in eq. (1.8) and define the turbine speed parameter (TSP) as the eq. (1.9)

$$TSP = N_{tc} \frac{1}{\sqrt{T_{03}}} \tag{1.9}$$

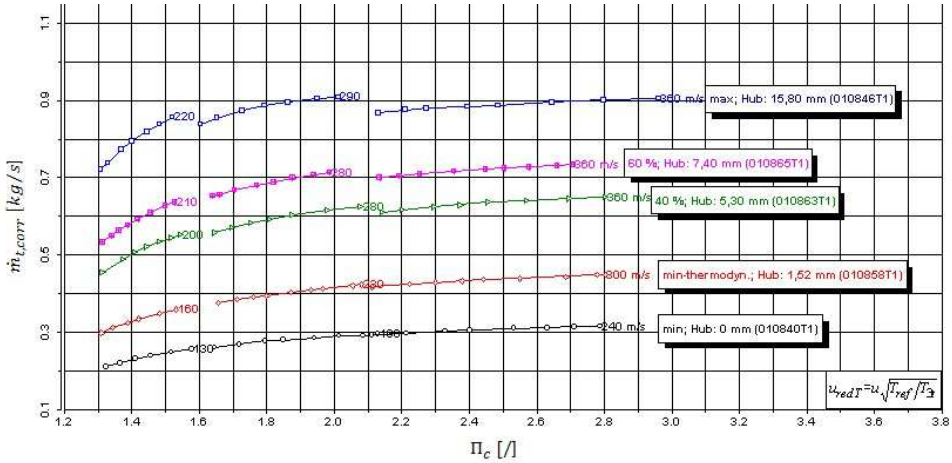

Figure 1.2 Example of turbine map

Since p_{std} and T_{std} are constants, neglecting them in eq. (1.5) and (1.8) to give eq. (1.6) and (1.9) respectively, gives only a scaling.
The adiabatic efficiency of the turbine is given by the eq. (1.10)

$$\eta_t = \frac{1 - \frac{T_{03}}{T_{04}}}{1 - \left(\frac{p_{04}}{p_{03}}\right)^{\frac{\gamma_t - 1}{\gamma_t}}} \tag{1.10}$$

where γ_t is the ratio of specific heats for the exhaust gas.

The high temperatures on the turbine side cause large heat fluxes. Measurement of T_{04} can have substantial systematic errors, due to the heat

fluxes. An alternative efficiency definition for the turbine side is therefore commonly used, where no measurement of T_{04} is needed. The heat transfer effects are less pronounced on the compressor side, and the compressor power

$$P_c = \dot{m}_c \cdot c_p (T_{02} - T_{01}) \tag{1.11}$$

can be used to define an alternative efficiency. This alternative turbine efficiency definition includes the shaft friction, and the equation is

$$\tilde{\eta}_t = \eta_t \cdot \eta_m = \frac{\dot{m}_c \cdot c_{p,c} \cdot (T_{02} - T_{01})}{\dot{m}_t \cdot c_{p,t} \cdot T_{03} \cdot \left(1 - \left(\frac{p_{04}}{p_{03}} \right)^{\frac{\gamma_t - 1}{\gamma_t}} \right)} \tag{1.12}$$

where the shaft friction is included in the mechanical efficiency η_m. Figure 1.2 shows an example of a turbine map.

1.4 Turbochargers modeling

Modeling of nominal turbochargers operation is divided into three subsections, depending on the model structure.

1.4.1. 3D and 1D models

Gas motion can be modeled in 3D, e.g. solving the Navier-Stokes equations of gas motion numerically. Such modeling needs accurate geometric information of the system, see e.g. the complex impeller geometries of Figure 1.3.

Figure 1.3 Compressor impeller

The boundary conditions of the model are further important, i.e. how the gas enters and leaves the modeled component. Due to the complexity and the computational effort, these models are most often only used to model components of the engine [119][57][60]. The solutions obtained, give valuable information of for example the gas motion, that can be used also for less complex model families. Also the reverse is true [29]; good models from less complex model structures can be used on a component level for a 3D simulation. Another level of detail that is frequently used, is the 1D model family. They model the gas flow along pipes and account for properties in this dimension. However 1D models of compressors are rarely found. The computational cost is reduced, compared to 3D models, and large parts of an engine system can be simulated with reasonably short simulation times.

1.4.2. Physical 0D compressor models

For the physical compressor model, an ideal compression process is frequently assumed, and different losses are then described and subtracted from the ideal component performance. This model structure often makes use of the velocity triangles, exemplified for the impeller entry in Figure 1.4. This section follows a gas element through the compressor, and describes important losses along the way, that are compiled to the model. The air flow into the compressor is assumed to have no circumferential velocity, i.e. no pre-whirl, and the diffuser section is assumed to be vane-less. An automotive compressor is normally vane-less and without intentional pre-whirl, due to the fact that a vaned diffuser normally has a

narrower flow range, and a pre-whirl system is avoided due to additional cost and packaging constraints.

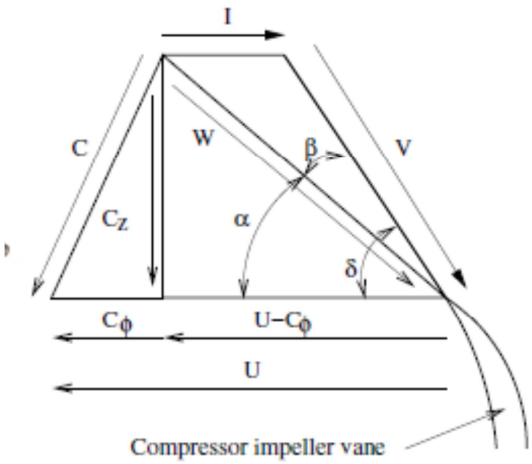

Figure 1.4 Velocity triangle

The first losses occur since the gas has to comply with the vane geometry at the impeller inlet. These losses are referred to as incidence losses [53], and are due to that the inducer relative velocity vector W does not agree with the vector parallel to the vane surface, V, see Figure 1.4. The impeller vane angle varies with the radius of the impeller, since the outer points on the impeller have higher relative velocities [49]. Studying Figure 1.4, the incidence losses are minimized if I = 0, but [53] states that the actual velocity vectors are not given simply by the geometries of the compressor, due to inertial effects of the gas. The fluid friction losses due to the gas viscosity and motion through the compressor are modeled in [115][55][52], where slip is used to model the gas flow through the impeller. Slip describes how well the gas is guided by the impeller vanes, and is discussed and modeled in [38][76][90]. Generally, the less guidance the gas attracts from the vanes the more slip. The more guidance, the more friction. Due to the potentially large pressure gradient through the compressor, flow can recirculate unintentionally. These flow recirculation losses occur due to the clearance between the impeller, rotating at high velocity, and the compressor housing. Flow recirculates both from the pressure side of the impeller vanes to the suction side, and along the compressor housing, from after the impeller, to the impeller entry. Models of these losses are presented in [53][66].

The air that recirculates to the impeller entry, is already heated by the compression process. The temperature of the recirculated air increases with increased compressor pressure ratio, and the amount of recirculated air is a function of pressure ratio and not turbo speed. This recirculation occurs where the local gas pressure is high and velocity is low [60]. Experimental data of recirculation is also presented in the literature [1]. The radial temperature profile at the impeller entry is experimentally shown in [1]. For compressors with vaned diffusers, an incidence loss can be associated with the air leaving the impeller, and entering the diffuser passages. These losses are however not simply given by the geometries of the impeller and diffuser vanes, but also of the flow physics inside the impeller [49]. Experimental investigations of the gas motion in the diffuser is found in [97]. The main cause of the diffusion process losses, are in [38] said to be separation of boundary layers and fluid friction. Losses in the volute [114], and losses due to disc friction [116] and choking [29] can also be modeled. The losses associated with the volute are more pronounced for a vaned diffuser, and are modeled in [53]. In [66] it is noted that the relative magnitude of the clearance, backflow and volute losses decreases with increasing mass flow, since the losses associated with incidence and friction increase more.

1.4.3. Curve fitting 0D based models

The curve fitting based approach is another subset of the 0D model family, and recognizes that all performance variables are conveniently given by the speed lines and the efficiency contours of the map. The modeling effort is then to fit different curves to the map, or to a transformed map.

Semi-physical modeling usually transforms the compressor map variables into the dimensionless head parameter Ψ and the dimensionless mass flow coefficient Φ. A connection between Ψ and Φ is then parameterized and used as a model [65][103][41]. Curve fitting directly to the map variables is another way to produce a model. The modeling effort is then to create functions describing the speed lines and iso-contours of efficiency of the map. A summary of curve fitting models for automotive control applications is presented in [79], and both speed line shapes [22] and efficiency contours are modeled [2][101][44]. Both the models of [72] and [74] use a parametrized ellipse to represent the speed lines of the

map, and are therefore of the curve fitting family.

1.4.4. Choke flow and restriction modeling

The previous section described nominal compressor operation and these section presents research relevant for modeling choked flow, and when the compressor only restricts the air, e.g. compressor operation with a pressure ratio lower than unity. If the inlet section of the compressor chokes, the choking is independent of compressor speed. This since the flow is choked, before it reaches the impeller blades. A varying choke mass flow with shaft speed, can be expected if choking conditions are established further into the compressor. This since the density of the gas arriving at the choking section, can be increased through an increase in compressor speed. In [52] the choke mass flow, assuming that choking occurs in the impeller, is described as an increasing function in shaft speed. A model that extrapolates compressor performance maps to smaller pressure ratios, including choking effects, is described in [29]. For pressure ratios lower than unity the compressor is assumed to work as an restriction for the flow, and the behavior of the compressor is compared to a nozzle discharge [81], where further a constant efficiency of 20 % is assumed in this operating region. [74] uses a choke mass flow model that is affine in corrected shaft speed. This is physically motivated by that a compressor impeller that stands still has a non-zero choke flow, and an increase in choke flow can be expected for increases in corrected shaft speed, up to the point where the compressor inlet chokes. The speed line model in [72] focuses on a the nominal compressor map, but the speed lines are extended to also cover pressure ratios less than unity. Constant compressor efficiency is assumed in this region in [72][74]

1.4.5. Surge and zero mass flow modeling

The last region of the compressor map is the one left of the surge line in Figure 1.1. When the compressor operating point moves beyond this line, surge will occur since the compressor is unable to maintain flow. When the flow breaks down completely, the highly pressurized air travels upstream, reversing the mass flow. This reversed flow reduces the pressure ratio, until the compressor is able to maintain positive mass flow. The pressure ratio then increases again and, if no other changes are applied to the system, the compressor enters a new surge cycle. Surge in

automotive applications can be encountered for example during a gear change in an acceleration phase. When the accelerator pedal is released, a sharp reduction in throttle mass flow results. Due to the inertia of the turbo, the compressor wheel does not slow down fast, and the compressor continues to build pressure.

To model surge many authors follow the Moore-Greitzer approach [56]. An extra state is introduced in the model to handle changes in mass flow through the compressor, where, due to the gas inertia, the compressor mass flow deviates from stationary performance curves for a transient [48]. Surge can be established from low to high turbo speeds [59]. The frequency of the surge phenomenon is mainly given by the system properties, where the downstream volume is most important. Most of the time in a surge cycle, is spent in either emptying or filling the downstream volume [47][22][56], and measurements of a clear connection between increased surge frequency and decreased downstream volume is presented in [48]. The filling period of the cycle is longer than the emptying, due to the flow through the throttle downstream of the compressor in a SI engine [56]. The surge frequency also depends on the compressor characteristic, and compressor speed will therefore also affect the surge frequency [47][56]. The surge phenomenon has a hysteresis effect, where the breakdown of the flow does not follow the same path in the compressor map as the build up of flow [1][56]. Mass flow measurements of surge presented in [1], show that the flow reversal is conducted at nearly constant pressure, followed by an increasing mass flow at lower pressure, and finally a rapidly increasing mass flow to a steady flow compressor speed line. The unstable branch of a compressor speed line is modeled using a third order polynomial, and is said to influence the modeled surge cycles to a small degree, since the time spent there is small [59]. Compressor pressure ratio at zero mass flow has been modeled in different versions in [48][107][54]. The negative flow branch of an extended compressor map, is modeled using a parabola with good accuracy in [59]. The Moore-Greitzer approach is followed in [72]and [74], and a third order polynomial in corrected mass flow is used in both papers for the unstable branch. This polynomial is parametrized to give zero derivative for the zero mass flow pressure build up point. The model of [74] then uses a turbine flow characteristic for the negative flow branch, while [74] uses the third order polynomial also for reversed flow. Constant compressor efficiency is assumed for surging mass flows in

[72][74].

1.5 Summary

The present manuscript is divided in three macro-areas concerning modeling, optimization and control of engines and components.

In the next chapter the optimization of the control variables for a turbocharged CI engine is faced [3]. The optimization analysis is based on an engine simulation model, composed of a control oriented model of turbocharger integrated with a predictive multi-zone combustion model, which allows accounting for the impact of control variables on engine performance, NO_x and soot emissions and turbine outlet temperature. This latter strongly affects conversion efficiency of after treatment devices therefore its estimation is of great interest for both control and simulation of tailpipe emissions. The proposed modeling structure is aimed to support the engine control design for common-rail turbocharged Diesel engines with multiple injections, where the large number of control parameters requires a large experimental tuning effort. Nevertheless, the complex interaction of injection pattern on combustion process makes black box engine modeling not enough accurate and a more detailed physical model has to be included in the loop. An hybrid modeling approach, composed of black and grey box models is implemented to simulate compressor flow and efficiency maps. The grey box model is used at low engine speeds while the black box model, based on a moving least squares method, provides compressor data at medium- high speed. Both models appear to perform best in their respective area. On the other hand a classical grey box approach is implemented for the turbine, along its overall working range. Compressor and turbine models are implemented in a computational scheme for integration with a predictive multi-zone combustion model that simulates the fuel jet and its interaction with surrounding gases by dividing the jet core into many parcels in order to describe the thermal gradient and the chemical composition within the combustion chamber. The whole engine model allows simulating in-cylinder pressure and temperature, NO and soot emissions as well as turbine outlet temperature, depending on engine control variables (i.e. injection pattern, Exhaust Gas Recirculation - EGR, Variable Geometry

Turbine - VGT). Model validation is carried out by comparing simulated in-cylinder pressure trace and exhaust temperature with a wide set of experimental data, measured at the test bench in steady-state conditions on a small automotive Diesel engine. In the paper the overall modeling approach is presented with a detailed description of in-cylinder, compressor and turbine models and the results of the experimental validation vs. measured data are shown. Furthermore, the optimization results over a set of operating points selected among those of interest for the ECE-EUDC test driving cycle are presented and discussed.

The third chapter deals with the impact of alternative fuels on engine control strategies [5][4]. Internal combustion engines for vehicle propulsion are more and more sophisticated due to increasingly restrictive environmental regulations. In case of heavy-duty engines, Compressed Natural Gas (CNG) fueling coupled with Three Way Catalyst (TWC) and Exhaust Gas Recirculation (EGR) can help in meeting the imposed emission limits and preventing from thermal stress of engine components. To cope with the new issues associated with the more complex hardware and to improve powertrain performance and reliability and after-treatment efficiency, the engine control strategies must be reformulated. The paper focuses on the steady-state optimization of control parameters for a heavy-duty engine fueled by CNG and equipped with turbocharger and EGR. The optimization analysis is carried out to design EGR, spark timing and wastegate control, aimed at increasing fuel economy while reducing in-cylinder temperature to prevent from thermal stress of engine components. The engine is modeled by a 1-D commercial fluid-dynamic code for the simulation of intake and exhaust gas flow arrangement. In order to speed-up the computational time, an empirical formulation based on the classical Wiebe function simulates the combustion process. Furthermore, an intensive identification analysis is performed to correlate Wiebe model parameters to engine operation and guarantee model accuracy and generalization even in case of high EGR rate. The optimization analysis is carried out by means of a co-simulation process in which the 1-D engine model is interfaced with a constrained minimization algorithm developed in the Matlab/Simulink® environment. Modeling approach and identification analysis are presented and the results of the experimental validation vs. measured data at the test bench are shown.

Both CI and SI engine control design and optimization have to face

with turbocharger control through wastegate or VGT (Variable Geometry Turbocharger) actuation. The fourth chapter concerns with turbocharger control. Particularly a model-based design of a PID controller for the boost pressure by means of an actuation systems acting on the turbine wastegate valves is handled [34][110]. Actuation systems for automotive boost control incorporate a vacuum tank and PWM controlled vacuum valves to increase the boosting system flexibility. Physical models for the actuator system are constructed using measurement data from a dynamometer with an SI GM 2.0 liters engine having a two stage turbo system. The actuator model is integrated in a complete Mean Value Engine Model and a boost pressure controller is constructed. Based on the actuator model a nonlinear compensator, capable of rejecting disturbances from system voltage, is developed. A boost pressure controller is developed for the vacuum actuator and engine, using IMC. The complete controller is evaluated in an engine test cell where its performances are quantified and system voltage disturbance rejection is demonstrated.

In the last chapter the conclusions will be presented.

CHAPTER 2

Turbocharged CI engine

The interest in Diesel engines for automotive application has dramatically grown in the last decade, due to the benefits gained with the introduction of common-rail system. A strong increase in fuel economy and a remarkable reduction of emissions and combustion noise have been achieved, thanks to both optimized fuelling strategy and improved fuel injection technology. Namely, the improvement of injector time response, injection pressure and nozzle characteristics have made feasible the operation of multiple injections and have enhanced the fuel atomization. Altogether these benefits make the combustion cleaner and more efficient, thus reducing both particulate emissions and fuel consumption. Furthermore, the presence of early pilot and pre injection may enable the occurrence of a quasi-homogeneous combustion with a reduction of noise and main combustion temperature and with a decrease of NO_x emissions. Despite the technological improvements of fuel injection systems and the increase of electromechanical actuators (e.g. EGR, VGT, waste-gate) the engine control design process evidences a methodological gap of Diesel engine compared to SI engine. Nowadays the design of SI engine control is supported by complex computational architectures (i.e. Hardware-In-the-Loop, optimization, rapid prototyping) where the main features are compliant with the opposite requisites of high accuracy and limited computational demand. In the field of electronic control for Diesel engines, it is likely to expect the implementation of methodologies derived from the SI engine in order to gain all the potential benefits of the common-rail system. Massive use of advanced mathematical models to simulate powertrain and system components (mechanical and electronic devices) is needed to speed up the design and optimization of engine control strategies. This problem is particularly felt in presence of a large number of control parameters (i.e. injection pattern, EGR, VGT), as it is the case of current Diesel engines, where the exclusive recourse to the experiments is extremely expensive in terms of money and time. The complexity of Diesel engine combustion, which is governed by the

turbulent fuel-air-mixing, causes an unresolved trade-off between computational time and accuracy. Single zone models based on empirical heat release laws [17], largely used to simulate SI engine performance and emissions, are inadequate to simulate the heterogeneous character of Diesel combustion. This problem is particularly felt for emissions prediction; in that case a huge effort has to be spent for the identification analysis to reach a satisfactory accuracy. Therefore, in order to achieve suitable precision, most of the studies in the field of Diesel Engine modeling have been addressed to the basic phenomena involved into fuel injection/evaporation, air entrainment, combustion and emission formation, with particular emphasis on particulate matter (mainly soot). On the other hand many advanced models are available in the literature, based on the complete 3D description of turbulent, multi-phase flow field inside the cylinder [88][33][98]. Despite their accuracy, these models present a large computational demand and are indeed oriented to engine design (combustion chamber shaping, fuel jet/air interaction, swirl) rather than to control design application. As experienced for the SI engine control design [9], the implementation of fast and flexible models of reduced order is required. The proper solution can be found in a modular approach from single zone toward more physical multi-zone models. These models are coupled with algebraic relationships (i.e. regressions) to relate model parameters to engine state variables on the whole working range. Phenomenological two-zone or multi-zone combustion models have been proposed in literature to meet the requirements for engine control design. Such models are accurate enough to predict fuel evaporation, air entrainment, fuel-air distribution and thermal stratification with a reasonable computational demand [70][6]. Particularly, the recourse to two-zone models, coupled with a detailed identification analysis of the main model parameters, makes it possible to have a predictive tool for simulating, with a reduced computational burden, the effects of control injection variables on combustion process and exhaust emissions formation [91][12]. The interaction of in-cylinder processes with intake/exhaust systems is simulated by coupling the predictive multi-zone model with a control-oriented turbocharger model. Particularly a quasi-steady approach based on the related characteristic curves has been followed to simulate compressor and turbine, according with the methodology usually proposed in literature for control-oriented application [80][27][28]. Simulation of intake/exhaust processes allows

predicting the gas temperature downstream the turbine which has great influence on the conversion efficiency of the after-treatment devices and consequently on tail pipe emissions

2.1.1. Model structure

The model structure is composed of a multi-zone phenomenological model for in-cylinder pressure and temperature simulation coupled with black-box and grey box models to simulate the steady-state behavior of turbine and compressor. The interaction between in-cylinder and turbocharger models is sketched in Figure.2.1 where a scheme of the overall computational structure is shown. The external inputs are the engine speed (*N*) and the control variables: injection pattern, EGR rate and VGT rack position (ξ). In steady state operation, the mutual interaction of compressor and turbine models is considered through the power balance at the turbocharger shaft. In order to calculate temperature and pressure into the exhaust manifold from in-cylinder data at Exhaust valve Opening (EVO), the assumption of ideal four stroke process with constant pressure turbocharging is considered to model the open valve cycle from EVO to Intake Valve Closing (IVC) [45].

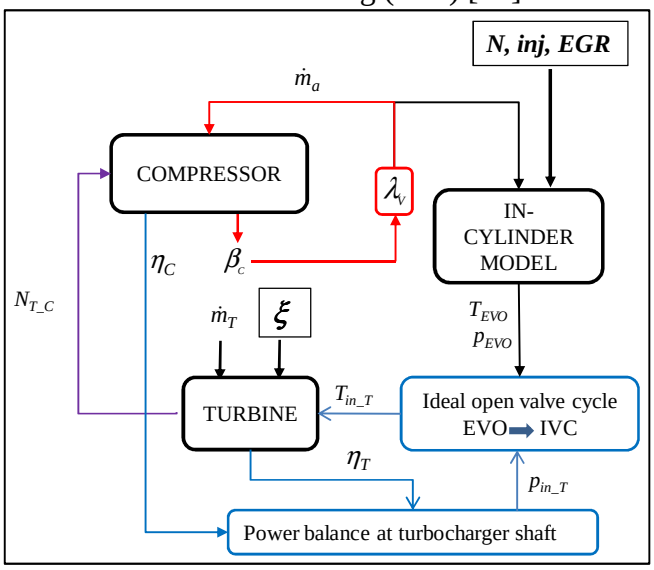

Figure.2.1 Scheme of the overall model structure, including in-cylinder, turbine and compressor models

Figure 2.2 shows the superposition of indicated and ideal exhaust

process, evidencing the isentropic expansion at Bottom Dead Center (BDC).The former assumption simplifies the evaluation of gas properties (i.e. pressure and temperature) during the exhaust process, thus reducing the computational time with respect to the simulation of the real exhaust blowdown process. Therefore the gas is supposed to continue its expansion from EVO to BDC with the same thermodynamic law as before EVO. The characteristic parameters (i.e. polytropic data) of the expansion process are computed from the simulated pressure cycle.

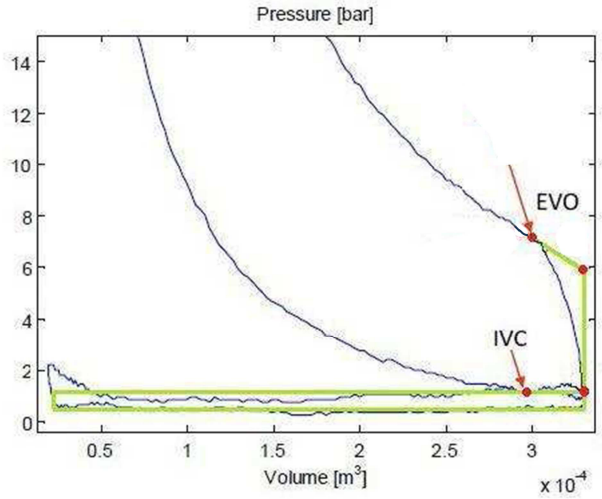

Figure 2.2 Superposition of indicated and ideal intake/exhaust strokes from EVO to IVC

At BDC it is assumed that the gas expands adiabatically and its properties are computed again with common thermodynamic laws. During the exhaust stroke, the adiabatic constant pressure assumption is considered to evaluate the temperature, which remains constants from BDC to TDC. In the next sections a satisfactory comparison with experimental data is provided for the temperature estimated at turbine inlet. During intake stroke the constant pressure process is assumed and the first law of thermodynamics is exploited to compute inlet temperature and gas density at IVC [45]. Again a comparison between simulated and measured intake variables was performed with satisfactory agreement, thus guaranteeing the proper accuracy of the exhaust/intake submodel.

It is worth reminding that the assumptions made are consistent with the turbocharged Mean Value Engine Model approach for steady-state

operating condition simulation [80][27]. Such an approach is well suited for the purpose, thus solving effectively the trade-off between accuracy and computing speed.

2.2 Common-rail injector

The electro-injector is the heart of the common-rail multiple injection system and its scheme is shown in Figure 2.3. It is fed by a single high pressure fuel line which is divided in two parts. The largest amount of fuel goes to the nozzle and the smallest attends to control the rod. Both parts are used to oil the internal moving connection of the element. The injector can be divided in two main parts:

- the atomizer composed by spin and nozzle;
- the solenoid valve controller.

The control volume (Vc) (see Figure 2.3) is permanently fed with the fuel by means of the hole Z, while the discharge of the fuel is left to the hole A, controlled by the solenoid valve. The force acting on the pressure rod is proportional to the pressure ruling in the Vc. The dynamics of the pressure rod depends mainly by the equilibrium of the following forces:

- F_e: acting in closing direction due to the spring on the spin.
- F_c: acting in closing direction due to the pressure of the fuel in the control volume at the top of the spin
- F_a: acting in opening direction due to the pressure of the fuel in the control volume on the anchor

When the solenoid valve is not excited (see left-hand of Figure 2.3), the pressure in the atomizer and in the control volume are equal and corresponds to the rail pressure so that $F_c + F_e > F_a$. In this case the closing forces are greater than the opening force and the injector keep closed. In order to open the injector, the condition $F_c + F_e < F_a$ has to be satisfied. In this case the lack of balance on the spin causes the nozzle opening and the injection of the fuel (right-hand of Figure 2.4).

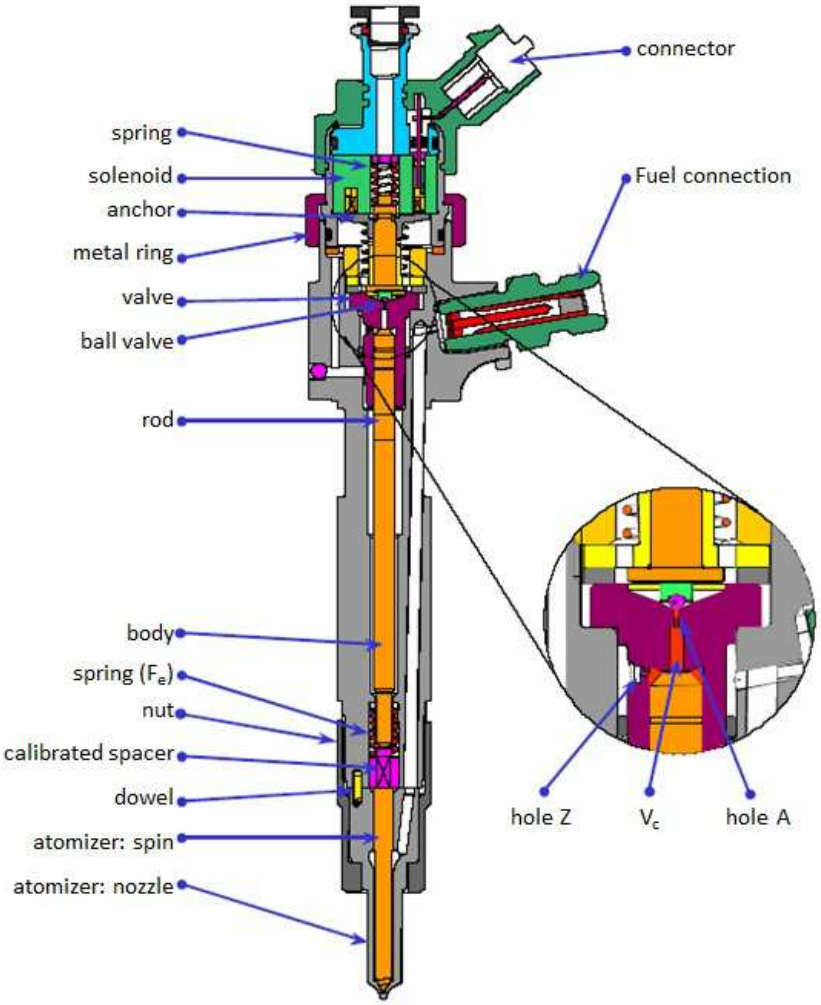

Figure 2.3 Scheme of the common-rail injector [32]

The solenoid valve throws off the forces. In resting position the solenoid is not excited and the valve is closed by means of a spring. In the control volume, fed by the hole Z, there is the rail pressure and then the closing forces (F_c+F_e) are greater than the opening force (F_a). For this conditions, there is no injection of fuel in the cylinder. By exciting the solenoid valve, the raising of the anchor is obtained, allowing the ball

valve to open the hole A. This hole has a discharge diameter greater than that of hole Z, and then the control volume empties.

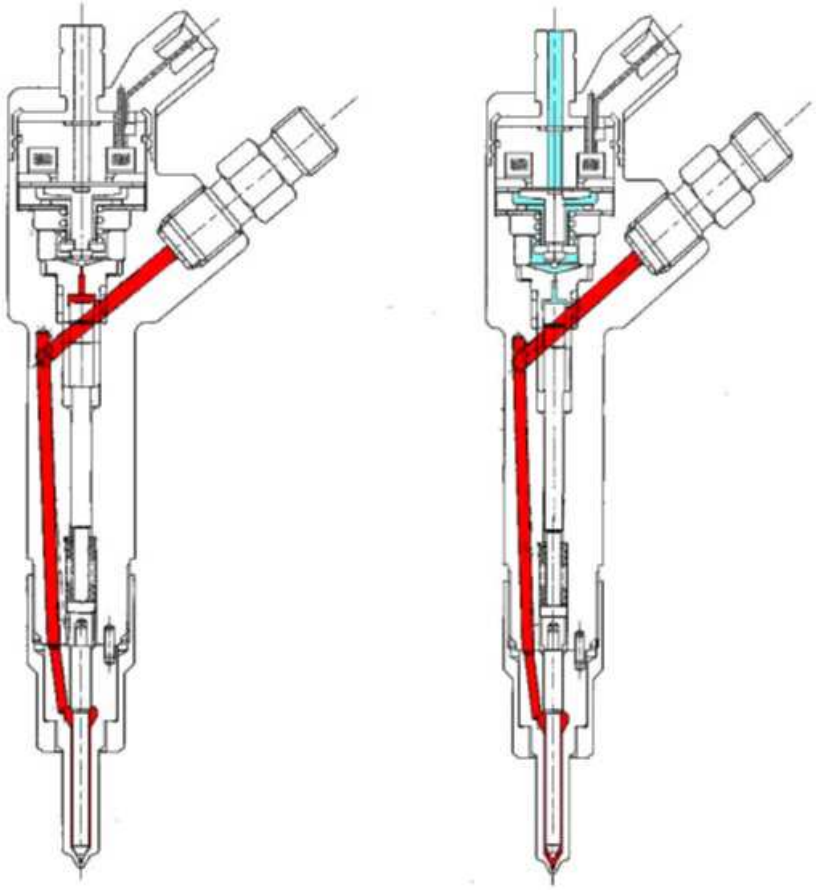

Figure 2.4 Injector in closing and opening position [32]

This generates a pressure drop in the control volume that causes a decrease in the force F_c. When the force drop verifies the inequality $F_c + F_e < F_a$, the rod begins to raise causing the opening of the atomizer. In this condition the fuel injection starts. The stop in the solenoid alimentation causes the closing of the hole A and a fast increasing of the control volume pressure till the equilibrium conditions for the closing of the injector. The quick movement of the rod, in order to guarantee a fast interruption of the injection, is due to a spring.

Because of the dynamics of the injector mechanical components, it is clear that there is no time synchrony between the electrical signal feeding

the solenoid valve (ET energizing time) and the opening of the injector, as shown in Figure 2.5 and in Table 2.1.

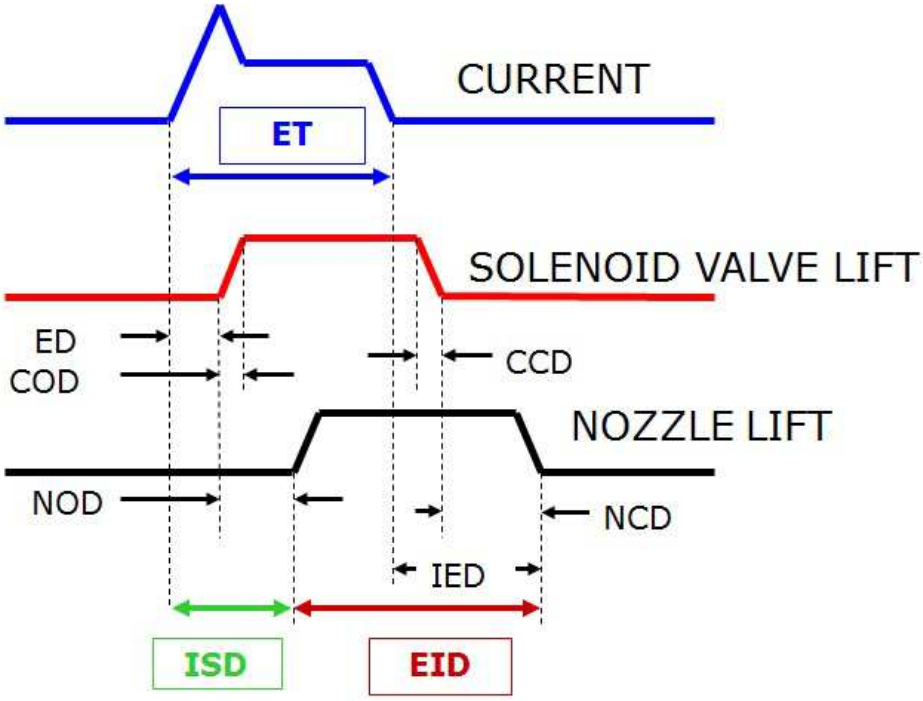

Figure 2.5 Time correlation between current, solenoid valve lift and nozzle lift

The only measurable variable for automotive application is the energizing time. This means that the correct injection timing (ISD) and the correct fuel volume injected in the cylinder cannot be measured by experimental test.

Detailed models of the dynamical behavior of the injector and possible improvement are available in literature [30][25][32]. These concern about the injector modeling from electrical features to fluid dynamic and mechanical features [25][32] and the possible improvement in order to avoid a pressure drop during the injection [30].

In par. 2.3.1 a simplified model of the injector is presented. The values of ISD and EID are estimated depending of the amount of injected fuel and the energizing time of each injection.

Table 2.1 Acronyms of Figure 2.5

ET	**Energizing Time**
ED	Energizing Delay
COD	Control Valve Opening Delay
CCD	Control Valve Closing Delay
NOD	Needle Opening delay
ISD	**Injection Start Delay**
NCD	Needle Closing Delay
IED	Injection End Delay
EID	**Effective Injection Duration**

2.3 In-cylinder simulation

Multi-zone model is structured so that a main routine interacts with a series of sub-routines for dynamic simulation of the jet, turbulence, combustion and emissions of pollutants. The combustion chamber is outlined in several zones with the same pressure but different temperature and composition. Each zone consists of a homogeneous mixture of ideal gases in chemical equilibrium. The thermodynamic properties of each area are measured as a function of pressure, temperature and composition [45]. Simulation of in-cylinder pressure is accomplished by a thermodynamic model, which is based on the energy conservation for an open system and on the volume conservation of the total combustion chamber [14][63][6][24]:

$$\dot{E}_i = \dot{Q}_i - \dot{W}_i + \sum_{j,i\neq j} \dot{m}_{i,j} \times h_{i,j} \tag{2.1}$$

$$V_{cyl} = V_a + \sum_i V_i \tag{2.2}$$

where i is the current zone and j are the zones affected by mass and energy exchange. $\dot{E}$ represent the temporal variation of the current zone, $\dot{Q}$ the thermal power transmitted to current zone, $\dot{W}$ the mechanical power transmitted from the current zone to the piston, $\dot{m}_{i,j}$ the mass flow, $h_{i,j}$ specific enthalpy, V_{cyl} the instantaneous cylinder volume and V_a and V_i the instantaneous volume of air zone and current zone.

During the compression stroke, the in-cylinder volume is filled by an homogeneous mixture of air and exhaust gases of the previous engine cycle, as shown in Figure 2.6

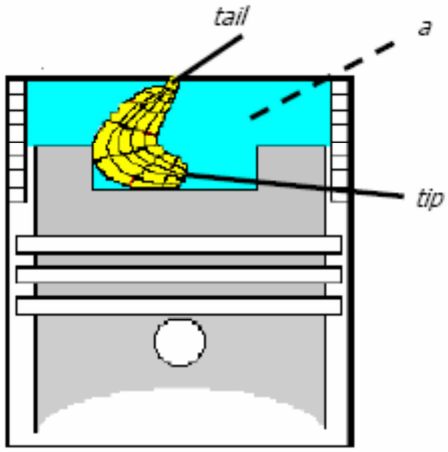

Figure 2.6 Scheme of the combustion chamber with air zone (a) and spray discretization in axial and radial direction

The composition is constant till the fuel injection which forms a spray for each injector hole. The spray is divided in radial and axial zones assuming that each zone has the same amount of fuel. In order to evaluate the thermal gradient each zone is divided in two more: burned and

unburned zone. The first one is an homogeneous mixture of combustion result, instead the second one is composed by an homogeneous mixture of air, vaporized fuel and exhaust gases of the previous engine cycle.

In order to complete eq. (2.1) and eq. (2.2), equations obtained from several submodels that describe physical phenomena, are used (e.g. for the injection, spray dynamic, evaporation, turbulence, ignition delay, combustion and pollutant emissions).

2.3.1. Injection

For estimating correctly the start of injection (SOI) and its duration from the electric signal sent by the ECU, an appropriate submodel has been developed by using the following equations:

$$t_{inj,d} = \frac{C_1}{V_{f,inj}} \tag{2.3}$$

$$\Delta t_{inj} = C_2 \cdot V_{f,inj} \cdot ET \tag{2.4}$$

where C_1 and C_2 are the model calibration constants, $V_{f,inj}$ is the amount of injected fuel for each injection and ET is the injector energizing time.

2.3.2. Spray dynamic

This submodel regards the position, the velocity end the momentum of each single zone in the spray. The spray model, called real from now, is based on the analysis of an ideal spray following these condition [82]:

- the density of the liquid fuel is much larger than that of the gas in which is injected;
- the velocity profile is constant along sections perpendicular to the axis;
- the injection speed is constant;
- fuel and entrained air move at the same speed;
- the jet has a conical shape;
- the velocity along the axis of the ideal jet is equal to that of the real jet;
- the momentum in each section perpendicular to the axis of the ideal jet is equal to that of the real jet.

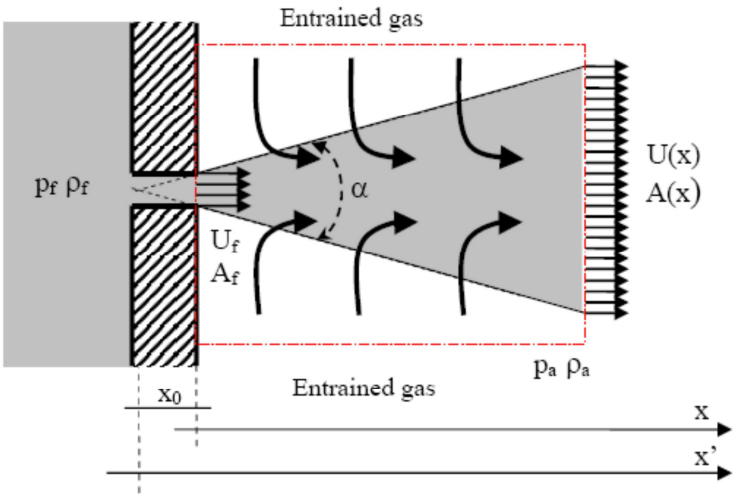

Figure 2.7 Ideal jet reference

Considering the red hatched control surface in Figure 2.7, the following mass and momentum conservations equations can be written between a generic section x and the section where x=0:

$$\rho_f A_f(0) U_f = \rho_f A_f(x) U_f(x) \tag{2.5}$$

$$\rho_f A_f(0) U_f^2 = \rho_f A_f(x)\left[U(x)\right]^2 + \rho_a A_a(x)\left[U(x)\right]^2 \tag{2.6}$$

$$A_a(x) = A(x) - \delta_f A_f(x) \tag{2.7}$$

where δ_f is a variable parameter between 0 and 1, ρ_f the fuel density, A_f the fuel passing area, U_f the fuel velocity, ρ_a the air density, A_a the air passing area, A the passing area and U the velocity. By means of the three previous equations, the velocity of the spray, at any section, can be calculated. Starting from the velocity section by section and using the momentum conservation, the mass of entrained air is computed:

$$\dot{m}_{ae} = -C_3 \frac{m_{f,inj} \times U_f}{\left(\frac{dS}{dt}\right)^2} \times \frac{d^2 S}{dt^2} \tag{2.8}$$

C_3 is a calibration parameter that takes into account the effects about the collision of the spray with the head of the piston and the cylinder walls, $m_{f,inj}$ is the mass of injected fuel, U_f is the fuel speed and S is the penetration is the central zones of the spray.

2.3.3. Vaporization

The injected fuel moves as a liquid column, until the break-up time elapses when the spray disintegrates and several little droplets form. After the break-up distance, the droplets begin to interact with the surrounding air and to fall more and more their diameter until atomization and vaporization. The injected fuel, vaporizing, merges with the surrounding air supporting the combustion. Related to the break-up distance, there is the break-up time expressed as in eq. (2.9)

$$t_b = 4.351 \frac{\rho_l d_n}{C_d^2 \left[\rho_a \left(p_f - p_a\right)\right]^{0.5}} \tag{2.9}$$

where ρ_l and ρ_a are, respectively, the density of the fuel and of the air, p_f and p_a are, respectively, the pressure of the fuel and of the air, d_n is the injector hole diameter and C_d is the discharge coefficient. The break-up distance is shown in Figure 2.8. Gone over the break-up distance, the spray vaporizes.

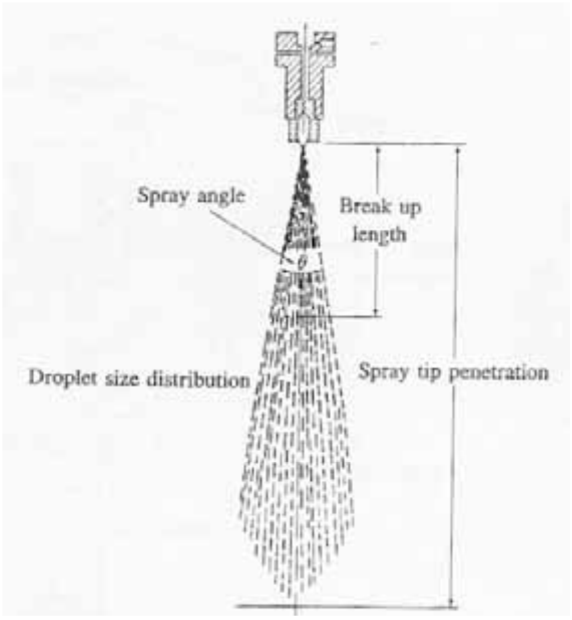

Figure 2.8 Break-up distance and spray angle

In this submodel the fuel phase transition is modeled in accordance with some hypothesis:

- vaporization follows the spray pulverization;
- the droplets have spherical geometry;
- the droplets are composed by only one component: in this case the tridecane ($C_{13}H_{28}$)
- the droplet temperature is uniform
- section by section, all the droplets have the same diameter.

The diameter is assumed to be the Sauter mean diameter (SMD evaluated as follow:

$$\frac{dm_{fv}}{dt} = \pi d_l N D_v Sh \frac{p}{R_v T^m} ln\left(\frac{p}{p - p_{vsurf}}\right) \tag{2.10}$$

where m_{fv} is the vaporized fuel mass, D_v the binary diffusion coefficient evaluated at the mean temperature of the boundary layer (film temperature) T^m, Sh the Sherwood number, p the in-cylinder pressure, p_{vsurf} vapor pressure evaluated at surface temperature of the liquid and d_l

the spherical and non-deformable droplet diameter.

2.3.4. Turbolence

The in-cylinder flow field cannot be computed point by point, so that the turbulence is taken into account in reference to the mean value. In order to make clear this phenomenon, the concept of homogeneous and isotropic turbulence is introduced: the statistical characteristics are independent from the space position and are the same in all the directions. Following this hypothesis, and merging it with the equilibrium between production and dissipation of the turbulence, the model of differential turbulence is formulated [92]:

$$\frac{dk}{dt} = \frac{2}{3}\frac{k}{\rho}\frac{d\rho}{dt} - \varepsilon \tag{2.11}$$

$$\frac{d\varepsilon}{dt} = \frac{4}{3}\frac{\varepsilon}{\rho}\frac{d\rho}{dt} - \frac{2\varepsilon^2}{k} \tag{2.12}$$

where k is the turbulent kinetic energy and ε is its velocity of dissipation. In eq. (2.11) and (2.12) the first terms of the right-hand member represent respectively the k and ε production due to compression whereas the second terms are their dissipation. Eq. (2.11) and (2.12) are a system of ordinary differential equation and, for integrating them, two congruent initial condition are needed: the first one for the turbulent kinetic energy and the other one for the dissipation velocity. In order to determine the initial conditions, it is needed to define the turbulence profile which portrays the flow motion of the fluid aspirated at initial moment of the integration range. In the internal combustion engines, the turbulence intensity is assumed to be proportional to the flow mean speed entering in the cylinder at the intake valve closing. This speed is correlated to the piston mean speed (V_{mp}) by mean of a proportional factor B_I [94]. The integral scale of the length L_I stands for the biggest dimension if the turbulent vortex at the intake valve closing. So that the conditions are:

$$k_{IVC} = \frac{2}{3}\left(B_I V_{mp}\right)^2 \tag{2.13}$$

$$\varepsilon_{IVC} = \frac{k_{IVC}^{1.5}}{L_{I,IVC}} \tag{2.14}$$

2.3.5. Ignition

To resolve the problem of the delay between the fuel injection and its ignition a model is needed. The in-cylinder pressure raising is made explicit by an evident deviation than the compression stroke. The ignition delay considers both the physic delay, corresponding to the time required to enter the first droplet in the combustion chamber, vaporize and mix with the surrounding air, and the chemical delay, corresponding to the typical time of the processes of chemical kinetic connected with the fuel burning. Generally, the ignition delay is a complicated function of mixture temperature, pressure, air-fuel ratio and fuel properties. In this model the delay is estimated through an Arrhenius correlation [67]:

$$\tau_{id} = A_{id}\, p^{-1.02} e^{\frac{2100}{T}} \tag{2.15}$$

where p and T are the in-cylinder pressure and temperature, respectively and A_{id} is an empirical parameter and was set to 3.45 according with literature data [62]. Starting from the SOI, and taking in account the pressure and temperature variations, the star of combustion is founded by means of eq. (2.16)

$$\int_{SOI}^{SOC} \frac{dt}{\tau_{id}} = 1 \tag{2.16}$$

2.3.6. Combustion

The speed with which the mass entrained in each zone in the flame burns is calculated with the turbulent combustion model proposed in [92]:

$$\frac{dm_b}{dt} = \frac{m_e - m_b}{\tau_b} \tag{2.17}$$

where the characteristic time τ_b is the same for each chemical reactants. In order to account for the interactions between turbulent and chemical reactions the characteristic time is calculate as the weighted sum

of the laminar timescale ($\tau_{b,lam}$) and the turbulent timescale, ($\tau_{b,turb}$):

$$\tau_b = \tau_{b,lam} + \gamma \tau_{b,turb} \tag{2.18}$$

with the weight γ given as (see also Figure 2.9):

$$\gamma = \frac{1 - e^{-x}}{0.632} \tag{2.19}$$

where x is the combustion fraction defined as:

$$x = \frac{m_b}{m_v} \tag{2.20}$$

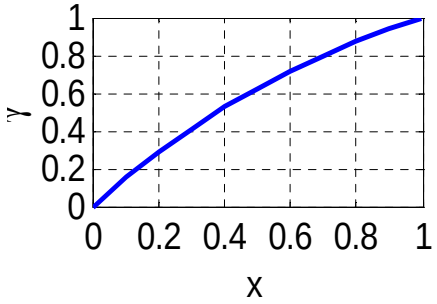

Figure 2.9 Dependence of γ from x

Zeroing the concentration of fuel at equilibrium, the laminar time scale is computed as:

$$\tau_{b,lam} = \left(7.68 \times 10^8 \left[n_{fv} \right]^{-0.75} \cdot \left[n_{O_2} \right]^{1.5} exp\left(- \frac{E}{R_0 T_b} \right) \right)^{-1} \tag{2.21}$$

where E = 77.3 103 J/mol and R_0= 8.3144 J/(mol K).

Finally the turbulent combustion time is considered proportional to the eddy turnover:

$$\tau_{b,turb} = C_4 \frac{k}{\varepsilon} \tag{2.22}$$

the proportional factor C_4 was set to 0.142 according with literature data [69][105][16][88].

2.3.7. Heat exchange

The heat exchange in an internal combustion engines if strongly non-stationary and depends on the crank angle and the measuring point. Some key-aspect of the phenomenon are:

- temperature, velocity and density of the gasses changing in time;
- geometry of the system change because of valve and piston motion;
- temperature of the cylinder walls and of the piston head changes point by point due to the different thickness of the material;
- heat exchange is influenced by the oil film and by the piston-cylinder friction;

By looking at the previous consideration, it is easy to understand that the modeling of the heat exchange in an internal combustion engine is very difficult. Applying the hypothesis that the thermal flow is constant along the cylinder walls and along the piston, the model used is [92]:

$$\dot{Q} = h_i \cdot A \cdot \left(T_g - T_w\right) + C_2 \cdot \sigma_0 \cdot A \cdot \left(T_g^4 - T_w^4\right) \tag{2.23}$$

where h_i is the coefficient of convection heat transfer, T_g and T_w are respectively the gas temperature and the wall temperature and σ_0 is the coefficient of radiation heat transfer for a blackbody.

2.3.8. Nitrogen oxide emission

The measured emission of NO_x at the tail pipe of an internal combustion emission are remarkably higher than the values calculated considering the chemical equilibrium at exhaust temperature. This means that the NO_x formation is not an equilibrium process driven by the kinetic of the chemical reactions so that is influenced by the temperature gradient in the burned gas areas. The model adopted is the well-known extended Zeldovich mechanism which use the following reactions:

$$\begin{cases} O + N_2 \leftrightarrow NO + N \\ N + 0_2 \leftrightarrow NO + O \\ N + OH \leftrightarrow NO + H \end{cases} \tag{2.24}$$

The model can be simplified assuming steady state conditions for the

atomic nitrogen under the very low concentration in the gasses. In addition, the energetic contribution of the formation and dissociation reactions of NO to the combustion is negligible so that these can be decoupled from the kinetic of the combustion reactions, characterized by shorter reaction time. Therefore it is allowed to bring near the concentration of O, O_2, OH, H and N_2 to the respective equilibrium concentration realized downstream the flame with gas completely burned. Following these assumptions, the Zeldovich mechanism allows to calculate the NO mole changing by means of the integration of the eq. (2.25) [10][62][92]

$$\frac{1}{V_b}\frac{dn_{NO}}{dt} = \frac{2R_1\left\{1-\left(\frac{[NO]}{[NO]_{eq}}\right)^2\right\}}{1+\left(\frac{[NO]}{[NO]_{eq}}\right)\frac{R_1}{R_2+R_3}} \tag{2.25}$$

where n_{NO} is the number of the moles of NO contained in the V_b volume of burned gas, eq. (2.25) is referred to the chemical equilibrium and R_1, R_2 and R_3 are:

$$\begin{aligned} R_1 &= k_1^+ [O]_{eq} [N_2]_{eq} \\ R_2 &= k_2^- [NO]_{eq} [O]_{eq} \\ R_3 &= k_3^- [NO]_{eq} [H]_{eq} \end{aligned} \tag{2.26}$$

And the velocity constant k are usually [92]:

$$\begin{aligned} k_1^+ &= 7.6\cdot 10^{13}\cdot exp\left(\frac{-38000}{T}\right) \\ k_2^- &= 1.5\cdot 10^{9}\cdot exp\left(\frac{-19500}{T}\right) \\ k_3^- &= 2\cdot 10^{14}\cdot exp\left(\frac{-23650}{T}\right) \end{aligned} \tag{2.27}$$

By looking at the previous equations, it is clear that the nitrogen oxide

formation is strongly connected with the maximum temperature reached during the combustion.

2.3.9. SOOT emission

The mechanism of particulate formation is one of the most critical tasks in Diesel engine modelling The basic phenomena which characterize the formation, the growth and the oxidation of the soot particles are not completely clear yet. The most common model used is proposed by Hiroyasu and models the formation and oxidation processes through two Arrhenius correlations [63]. The net soot mass is the difference between that produced and that oxidized

$$\frac{dm_s}{dt} = \frac{dm_{s,f}}{dt} - \frac{dm_{s,o}}{dt} \tag{2.28}$$

where $dm_{s,f}$ and $dm_{s,o}$, expressed by the eq. (2.29), are respectively the mass of formed soot and oxidized soot.

$$\begin{aligned} \frac{dm_{s,f}}{dt} &= A_f m_{f,p} p^{0.5} \cdot exp\left(-\frac{E_f}{RT}\right) \\ \frac{dm_{s,o}}{dt} &= A_0 m_s Y_{O_2} p^{1.8} \cdot exp\left(-\frac{E_0}{RT}\right) \end{aligned} \tag{2.29}$$

where $m_{f,p}$ is the net mass of soot, p is the in-cylinder pressure, Y_{O_2} is the oxygen fraction, A_f and A_0 are coefficients assumed both as $0.12 + N \cdot 3 \cdot 10^{-4}$, E_f and E_0 are the activation energies considered equal to 12500 [cal/mol] and 14000 [cal/mol] as proposed by [63].

2.4 Compressor model

Two approaches have been followed for the compressor model:

1. An interpolation method called the “moving least squares method”. This is a black box model.
2. A model with a few physical principles added, able to

extrapolate at low turbine speeds. This is a grey box model.

The target is to reproduce the experimental compressor map (Figure 2.10)

2.4.1. Black box model

The first alternative is a black box model called the moving least squares method [111][20]. Starting from data obtained (in this case from the compressor map), consider the data set $\left\{\overline{x_i}, \overline{y_i}\right\}_{i=1,2,..N}$ with $\overline{x_i}$ the coordinates and $\overline{y_i}$ the experimental points. Next a domain of influence $D\left(\overline{x_i}\right)$ is defined around each data point.

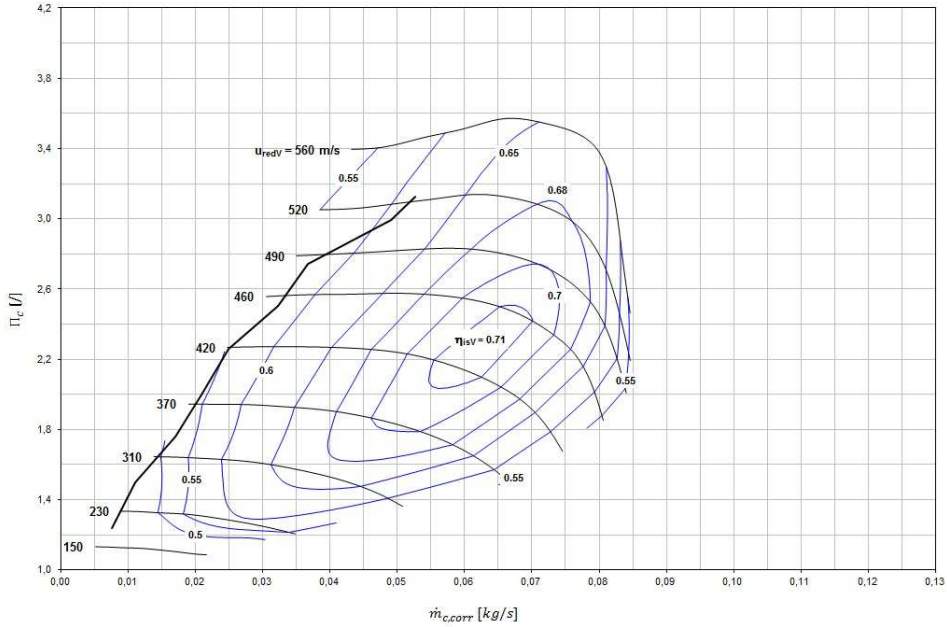

Figure 2.10 Compressor maps from the manufacturer

Within this domain a weight function $\delta\left(\overline{x}, \overline{x_i}\right)$ has influence:

$$\delta(\overline{x} - \overline{x_i}) = \begin{cases} \geq 0 if\ \overline{x} \in D(\overline{x_i}) \\ 0 if\ \overline{x} \notin D(\overline{x_i}) \end{cases} \tag{2.30}$$

The approximation on a coordinate $\overline{x}$ can be given by:

$$\bar{Y}(\bar{x}) = \sum_{j=1}^{m} p_j(\bar{x}) a_j(\bar{x}) \tag{2.31}$$

where p_j is the j-th basis, m = 3 for a linear basis ([1 x_1 x_2]) and m = 6 for a quadratic basis. $a_j(\bar{x})$ are the coefficients which have to be determined. The values for $a_j\left(\bar{x}\right)$ are determined by solving a regression problem for M experimental points in which the minimization of the error gives:

$$\bar{a}(\bar{x}) = \underline{A}^{-1}(\bar{x})\underline{B}(\underline{x})\bar{y} \tag{2.32}$$

where:

$$\begin{aligned} \underline{A}(\bar{x}) &= \sum_{i=1}^{M} \delta(\bar{x} - \bar{x}_i)\bar{p}(\bar{x}_i)\bar{p}^T(\bar{x}_i) \\ \underline{B}(\bar{x}) &= \left[\delta(\bar{x} - \bar{x}_1)\bar{p}(\bar{x}_1) \ldots \delta(\bar{x} - \bar{x}_n)\bar{p}(\bar{x}_n)\right] \end{aligned} \tag{2.33}$$

Hence the approximation $\bar{Y}$ is be given by:

$$\bar{Y}(\bar{x}) = \bar{p}^T(\bar{x})\underline{A}^{-1}(\bar{x})\underline{B}(\bar{x})\bar{y} \tag{2.34}$$

The principle of this approach is sketched in Figure 2.11. Consider a certain coordinate $\bar{x}$ and experimental points y_1, y_2 and y_3. The interpolated value $\bar{Y}$ on $\bar{x}$ will have a contribution of every measuring point which has $\bar{x}$ in its domain. In this example y_1 and y_2 will have influence, while y_3 has no influence at all. It can be seen that the more experimental points contribute to the approximation, the more accurate $\bar{Y}$ will be. This method could therefore be enhanced by distributing the experimental points more uniformly over the experimental domain using conformal mapping.

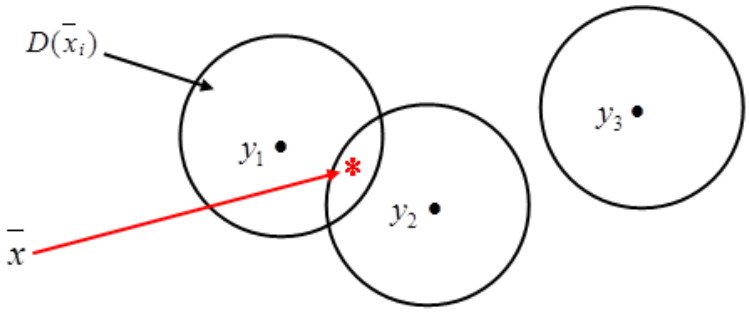

Figure 2.11 Sketch of the moving least squares method principle

Then the relative flow rate V_{rel} is transformed as follows:

$$\alpha(N_{rel}, V_{rel}) = \arctan\left(\frac{V_{rel}}{N_{rel}}\right) \tag{2.35}$$

$$V_{rel,trans} = \frac{\arctan\left(\frac{V_{rel}}{N_{rel}}\right) - \min\left\{\arctan\left(\frac{V_{rel}}{N_{rel}}\right)\right\}}{\max\left\{\arctan\left(\frac{V_{rel}}{N_{rel}}\right)\right\} - \min\left\{\arctan\left(\frac{V_{rel}}{N_{rel}}\right)\right\}} \tag{2.36}$$

A graphical representation of the domain transformation is presented in Figure 2.12. By distributing the coordinates more uniformly better accuracy can be achieved at areas where only a few data points are available.

After preparing the experimental domain and applying the moving least squares method the whole compressor map can be recreated as shown in Figure 2.13. The surge and choke lines are approximated by second and fourth order polynomials, respectively. The figure shows that the moving least squares method produces accurate results within the whole operating range of the compressor and is able to predict flow curves between two measured turbo compressor speeds. The error is found to be around ±1%.

The same procedure can be applied to approximate the efficiency of the compressor simply by replacing the experimental points of βc ($\bar{y}_i$) by the efficiency ηc.

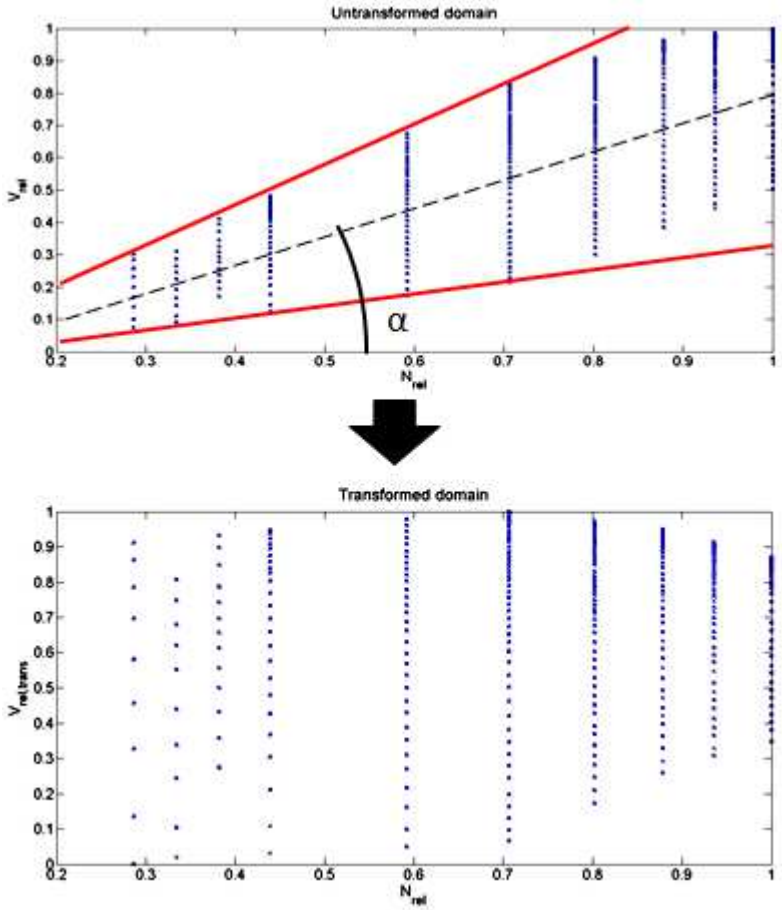

Figure 2.12 The experimental domain transformation using conformal mapping

There is one drawback to the moving least squares method. Although it performs well within the operating range of the compressor, it cannot extrapolate to low turbo compressor speeds (Figure 2.14). Extrapolating to low speeds is essential in order to study the behavior of the turbo compressor when the engine runs at low speed and low load. Therefore another method is proposed in 2.4.2.

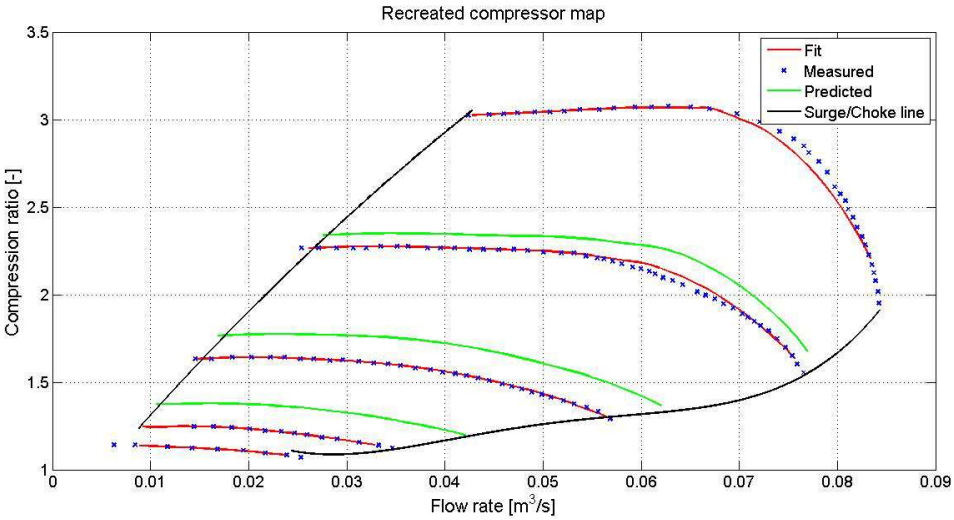

Figure 2.13 Graph of the recreated compressor flow map with fitted and predicted curves.

2.4.2. Grey box model

The second method is proposed by Marcello Canova and uses a few physical principles to both interpolate and extrapolate the compressor map [28].

For this approach the following parameters are used.

The inlet Mach number (Ma):

$$Ma = \frac{\frac{\pi}{30} N r_{tip}}{\sqrt{k_c R T_{ref}}} \tag{2.37}$$

The dimensionless flow parameter Φ:

$$\Phi = \frac{\dot{m}_{corr}\, R T_{ref}}{\frac{\pi^2}{30} r_{tip}^3\, p_{ref}\, N} \tag{2.38}$$

The head parameter Ψ:

$$\Psi = \frac{2c_{p,c}T_{ref}\left[\beta_c^{\frac{k,c-1}{k,c}} - 1\right]}{\left[\frac{\pi}{30} r_{tip} N\right]^2} \tag{2.39}$$

Ψ can be written as a function of Φ:

$$\Psi = \frac{k_1 + k_2\Phi}{k_3 - \Phi}, k_1, k_2, k_3 = f(N) \tag{2.40}$$

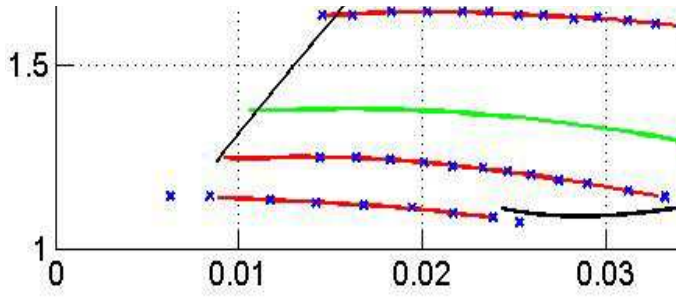

Figure 2.14 Low speed area of the compressor

The parameters k_1, k_2 and k_3 can be determined using the experimental data. First the data for each available speed is fitted using a third order polynomial, an example is shown in Figure 2.15.

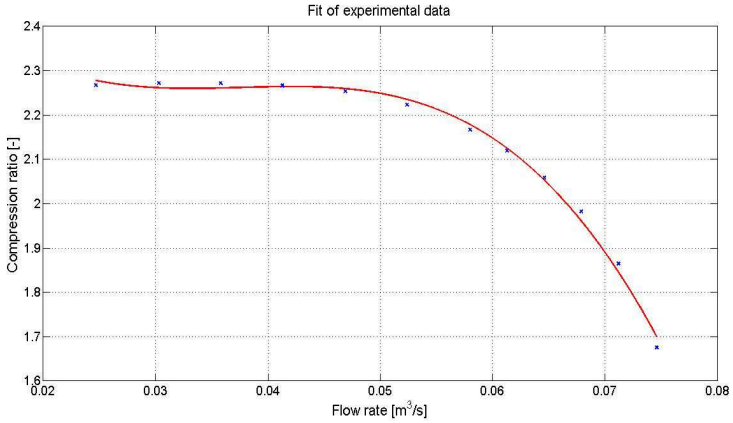

Figure 2.15 Example of a third order fit of a compressor flow curve

Now for each available turbine speed the parameters k_1, k_2 and k_3 can be determined. It should be noted that at $k_3 = \Phi$ a singularity will occur which might cause problems. The relation between the parameters k_i and N appears to be a linear function of the turbo compressor speed N, or the Mach number Ma:

$$k_i = k_{i,1} + k_{i,2} Ma \tag{2.41}$$

When the parameters k_i are known, the compressor map can be recreated using the relations above. This method is able to extrapolate to low turbo compressor speeds, as Figure 2.16 shows. The figure shows two fitted curves within the operating range and two extrapolated flow curves at 40.000 and 60.000 rpm. It can be observed that the results are accurate in the low speed area. When observing the results at high speeds it can be seen that significant errors occur. The singularity between flow rate 0.08 and 0.09 m^3/s in Figure 2.17 can be explained by the fact that k_3 approaches Φ.

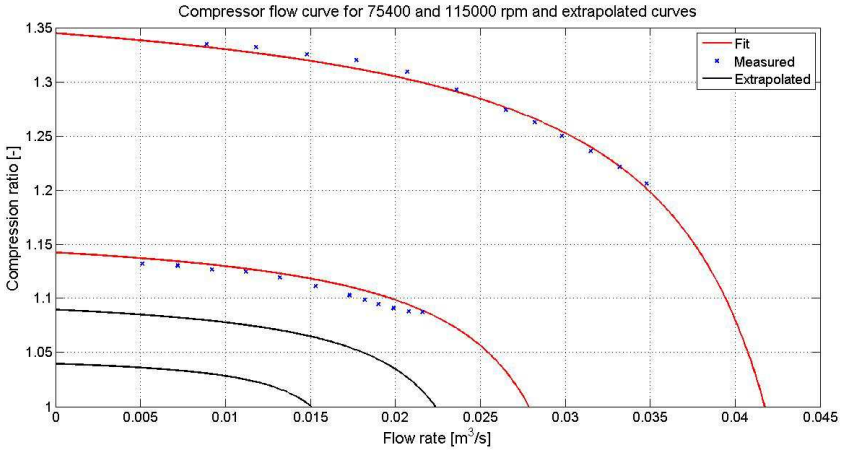

Figure 2.16 Fitted and extrapolate compressor flow curves in the low speed area

This singularity occurring at high speeds could question the applicability of this grey box method in this area. A combination of the black and grey box models could be useful. The efficiency calculation is based on the power output of the compressor. The power is related to the turbo compressor speed and the mass flow rate as follows:

$$P_{corr} \sim N_{corr}^3 \sim \dot{m}_{corr}^3 \tag{2.42}$$

So the corrected power output can be written as third order polynomial:

$$P_{corr} = b_1 \dot{m}_{corr}^{3} + b_2 \dot{m}_{corr}^{2} + b_3 \dot{m}_{corr} + P_{corr,0} \qquad (2.43)$$
$$b_1, b_2, b_3, P_{corr,0} = f(N_{corr})$$

$P_{corr,0}$ is the power output at mass flow zero. This value is obtained by linear extrapolation of the experimental data to mass flow zero, creating an extra data point as shown in Figure 2.18. For each turbo compressor speed the values for b_1, b_2 and b_3 can be found.

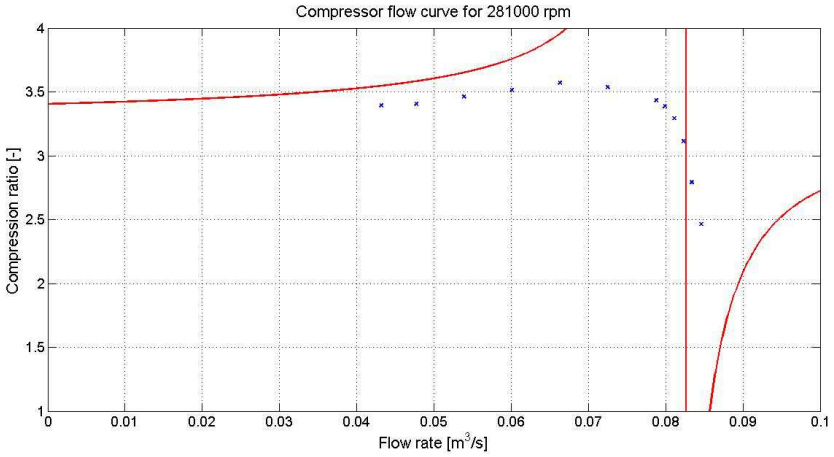

Figure 2.17 Fitted compressor flow curve in the high speed area

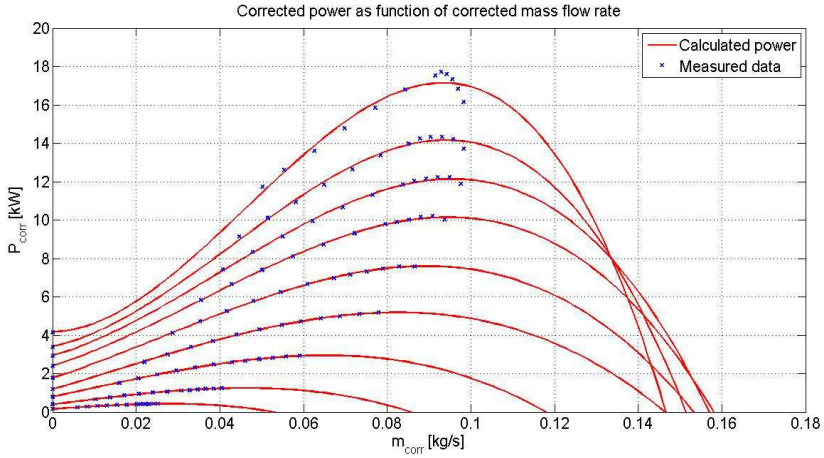

Figure 2.18 Fitted power curves

The relation between the coefficients b_i and $P_{corr,0}$ and N_{corr} is written as a third order function of the Mach number ($P_{corr} \sim Ma^3$) with an added constraint that the power goes to zero at Mach number zero. To do this, extra "measuring points" are created to force the fitted curve to zero as shown in Figure 2.19. This procedure is applied for all coefficients b_i and $P_{corr,0}$.

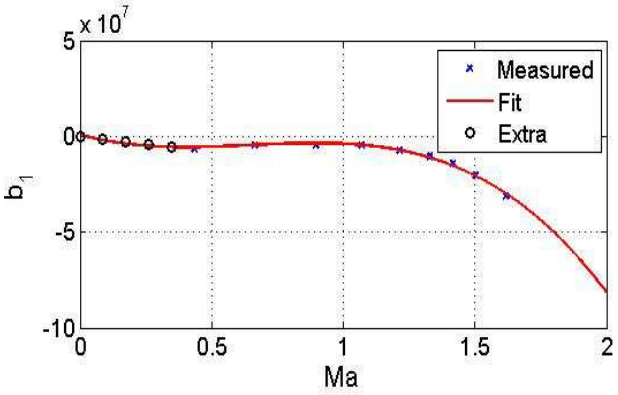

Figure 2.19 Fit of coefficient b1 as function of the Mach number

Once the corrected power is known, the definition for the work of the compressor is used:

$$P_{corr} = \dot{m}_{corr}\, T_a c_{p,c} \left(\beta_c^{\left(\frac{k,c-1}{k,c}\right)} - 1 \right) \frac{1}{\eta_c} \tag{2.44}$$

Now the compressor efficiency η_c can be determined. Figure 2.20 shows results of efficiency curves at low speeds, one fitted curve at 75,400 rpm and one extrapolated curve at 60,000 rpm. It can be seen that the results are accurate in this area. Figure 2.21 shows the results of a fitted efficiency curve at high speed, 281,000 rpm.

The situation between 0.08 and 0.09 kg/s is a result of the singularity caused in the flow calculation ($k_3 = \Phi$, eq. (2.40)). It can be concluded that the grey box model is applicable in the low speed area while the black box model is applicable in the whole operating range. An obvious suggestion is that both models are used: the grey box model in the low speed area and the black box model in the operating range.

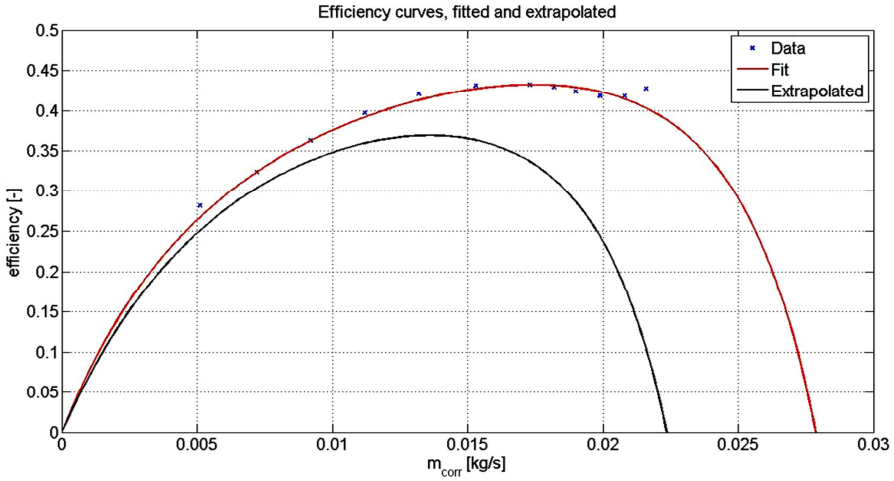

Figure 2.20 Fitted and extrapolated compressor efficiency curve in the low speed area

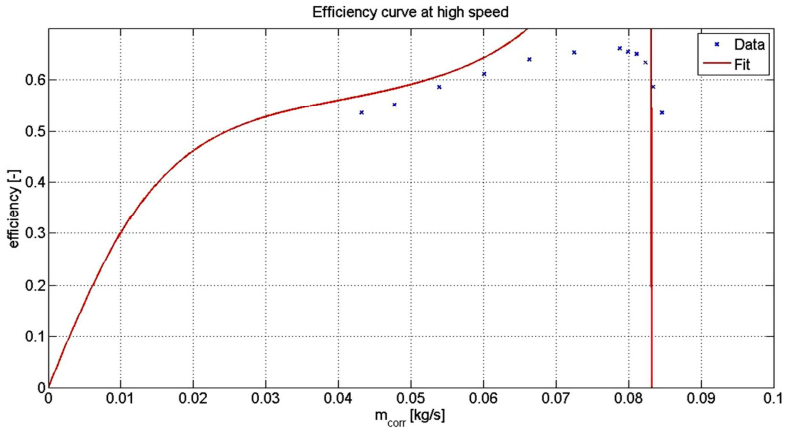

Figure 2.21 Fitted compressor efficiency curve in the high speed area

At last, Figure 2.22 shows the simulated compressor map recreated by the two models above descripted

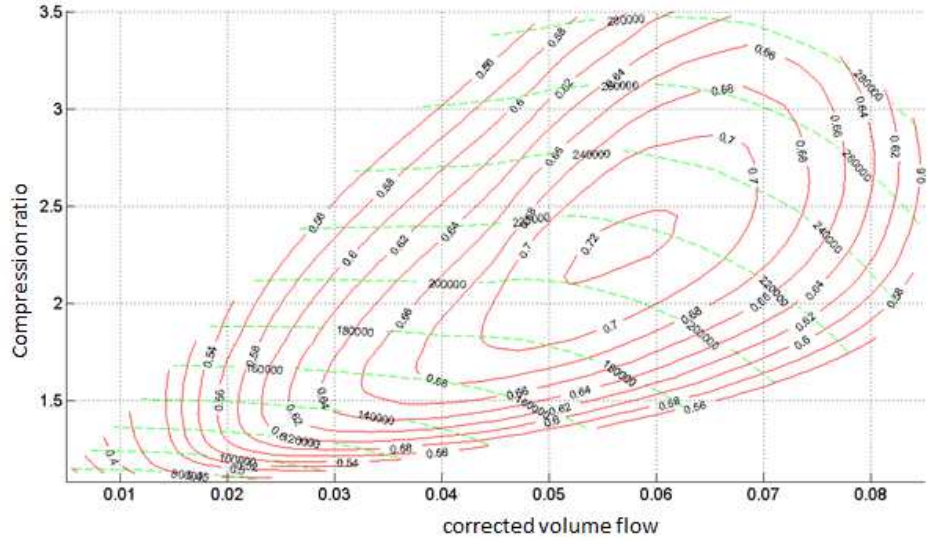

Figure 2.22 Simulated compressor map

2.5 Turbine model

The performance of the turbine is not only dependent on the turbo compressor speed, but also on the rack position of the vanes, in other words the turbine inlet area (as shown in Figure 2.23). A grey box approach proposed by Marcello Canova is used to describe the flow and the efficiency of the turbine using a few physical principles and the data from the turbine maps [28]. The turbine efficiency calculation is straightforward. The so called tip speed ratio is used:

$$\frac{U_t}{C_s} = \frac{\pi N_{corr} r_{in}}{30\sqrt{2c_{p,t}T_{ref}\left(1-\left(1/\beta_t\right)^{\frac{k,t-1}{k,t}}\right)}} \tag{2.45}$$

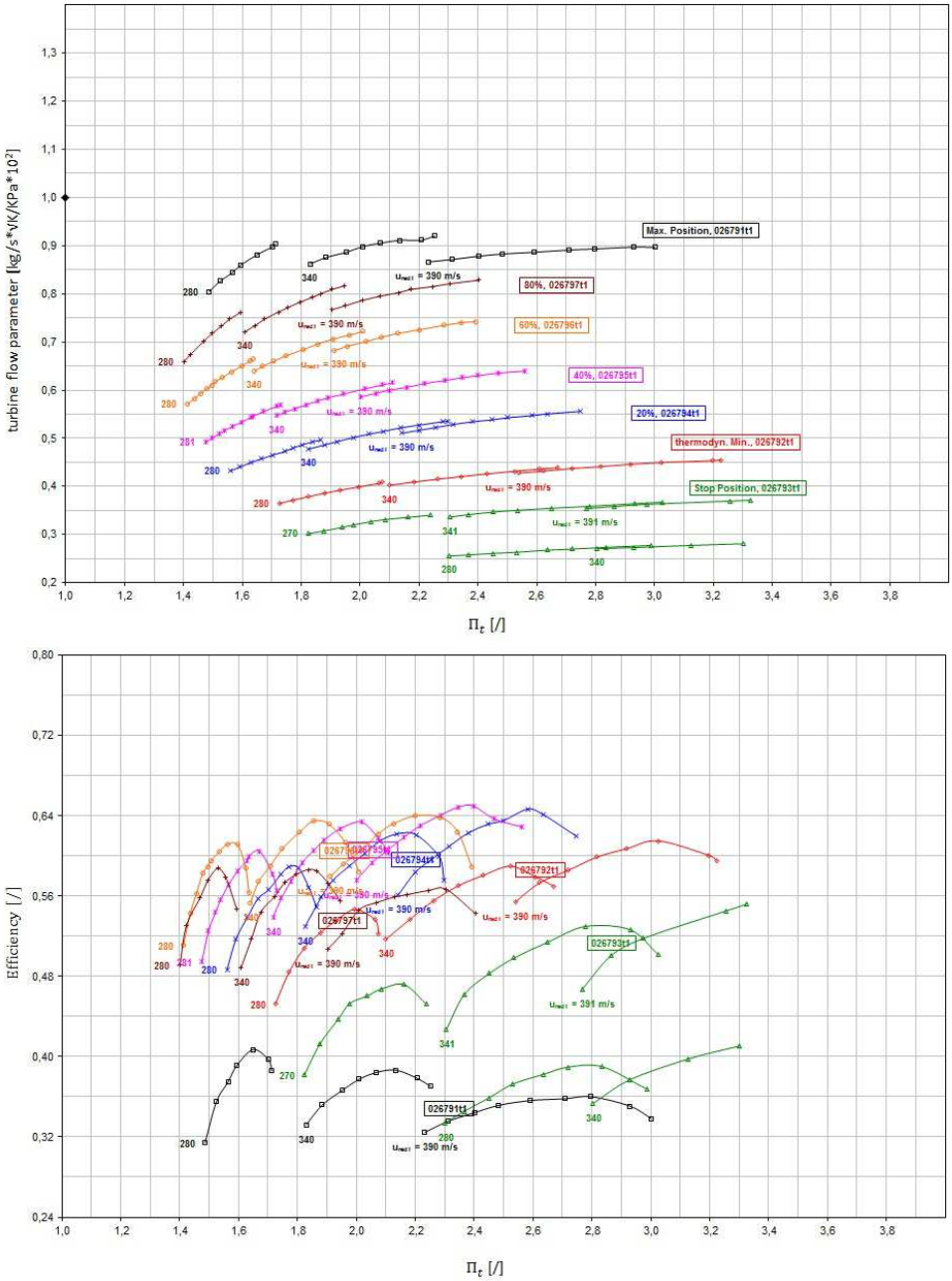

Figure 2.23 Turbine maps from the manufacturer

This is the ratio between the rotor tip speed and the speed the combustion gases would obtain after an isentropic expansion. The efficiency of the turbine can be written as a second order function of the tip speed ratio:

$$\eta_t = a_1 + a_2 N_{corr} + \left(a_3 + a_4 N_{corr}\right)\frac{U_t}{C_s} + \left(a_5 + a_6 N_{corr}\right)\left(\frac{U_t}{C_s}\right)^2 \qquad (2.46)$$

where

$$a_1, a_2, \ldots a_6 = f(\xi) \qquad (2.47)$$

The coefficients a_1, $a_{2\ldots}a_6$ can be found using the available turbine map data. This expression takes into account both the tip speed ratio and the rotational speed. Any efficiency curve can be recreated for one of the rack positions given by the experimental data. To calculate a curve between two given rack positions linear interpolation is used. Figure 2.24 shows three fitted efficiency curves and one predicted curve at a rack position of 40%.

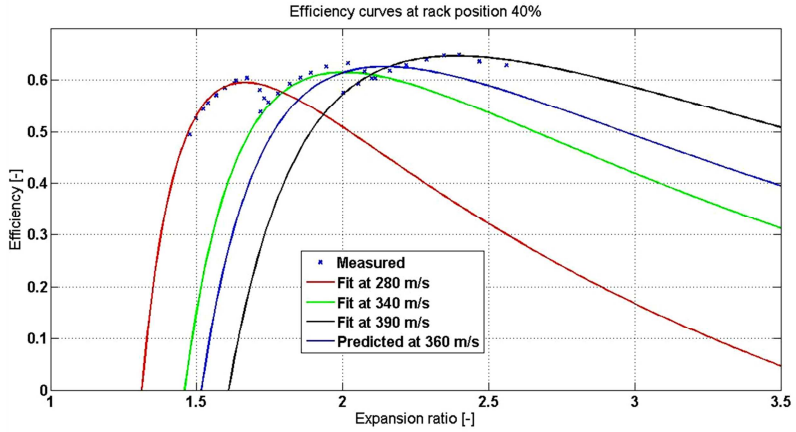

Figure 2.24 Fitted and predicted turbine efficiency curves

It can be observed that this method produces an accurate recreation of the turbine efficiency maps. The flow calculation is a bit trickier. The turbine is approximated as a non-isentropic orifice.

$$\dot{m}_{t,red} = \frac{\dot{m}_t\sqrt{T_3}}{p_3} = \frac{C_d\Omega}{\sqrt{R}} f(\beta_t) \qquad (2.48)$$

where C_d is the discharge coefficient and Ω the inlet area which is a function of the rack position ξ. The flow function $f(\beta_t)$ is given by:

$$f(\beta_t) = \begin{cases} \sqrt{\dfrac{2k_t}{k_t - 1}\left[\beta_t^{-\frac{2}{n}} - \beta_t^{-\frac{n+1}{n}}\right]} & \text{if } \beta_t \le \left(\dfrac{n+1}{2}\right)^{\frac{n}{n-1}} \\ \left(\dfrac{2}{n+1}\right)^{\frac{1}{n-1}} \sqrt{\dfrac{2k_t}{k_t - 1}\dfrac{n-1}{n+1}} & \text{otherwise} \end{cases} \tag{2.49}$$

The upper situation is for subsonic flow and the lower situation for choked flow. The polytropic coefficient n can be found from the definition of the isentropic efficiency:

$$\eta_t = \frac{1 - \frac{1}{\beta_t^{\frac{n-1}{n}}}}{1 - \frac{1}{\beta_t^{\frac{k,t-1}{k,t}}}} \tag{2.50}$$

The isentropic efficiency η_t and the expansion ratio β_t are known from map data. For convenience the value for n is averaged and taken constant for each rack position. This approach does not yet take into account the turbo compressor speed however. Therefore the expansion ratio β_t is written as:

$$\beta_t \rightarrow \beta_t - \beta_{t,0} + 1 \tag{2.51}$$

The parameter $\beta_{t,0}$ is the theoretical expansion ratio at mass flow zero. This is obtained by considering the energy equation for a fluid element in a centrifugal field:

$$\beta_0 = \left[1 + \frac{k_t - 1}{2k_t}\frac{1}{RT_{ref}}\left(\frac{\pi}{30}\right)^2 N_{corr}^2 \left(\frac{D_{in}^2 - D_{out}^2}{4}\right)\right]^{\frac{k,t}{k,t-1}} \tag{2.52}$$

The value for C_d and Ω are approximated as follows. First the data of the flow curves are extrapolated using a second order polynomial to estimate a maximum mass flow parameter as indicated in Figure 2.25.

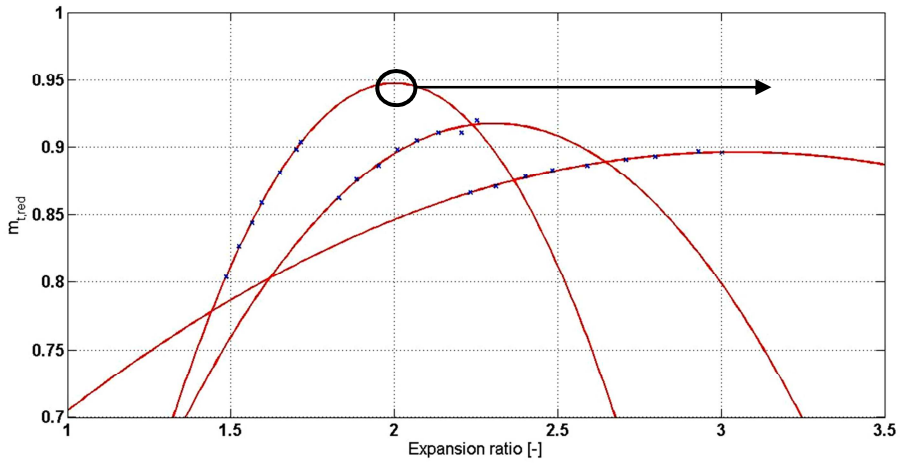

Figure 2.25 A second order fit of turbine flow maps is used to estimate a maximum reduced mass flow rate. An extra data point is created by fixing this maximum value to a high expansion ratio

A constraint is added by moving the found maximum far away (for example to $\beta_t = 20$) and fixing the value for C_d to 1 on this point. In other words, an extra data point is created. Now using eq. (2.48) and (2.49) on this point the value for Ω can be found (because $C_d = 1$). Once Ω is found (which is constant for constant vane rack position) C_d can be calculated for each data point using eq. (2.48) and (2.49). The found values of C_d are fitted using a second order polynomial, giving C_d as function of the expansion ratio for each rack position. It is assumed that C_d does not depend on the turbo compressor speed. With C_d, Ω and $f(\beta_t)$ known the flow curves can be calculated. An example of the recreated flow curves is given in Figure 2.26. Flow curves can be recreated for any turbo compressor speed on a certain rack position.

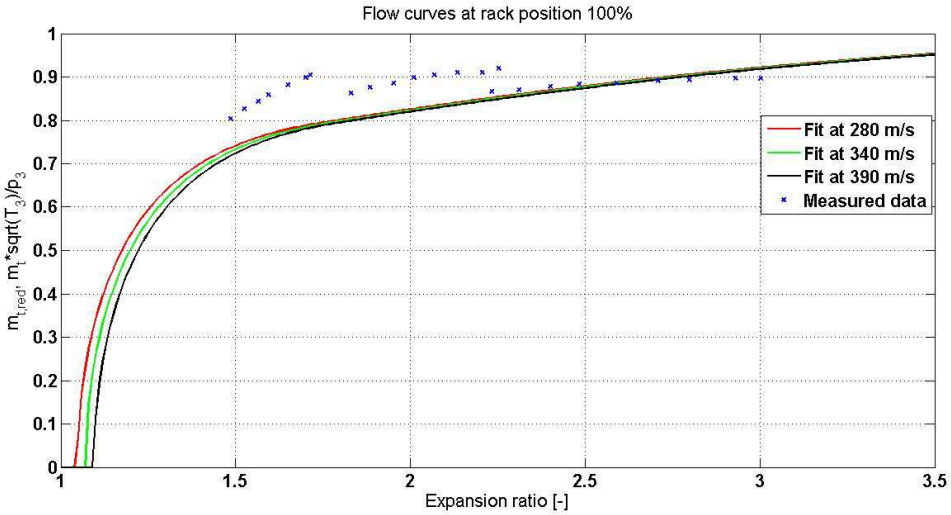

Figure 2.26 Fitted turbine flow curves

The error in the mass flow parameter goes up to 15%. This could be caused by:

- The approximation for the discharge coefficient C_d
- The assumption that the polytropic coefficient is kept constant at one rack position
- The constraint introduced at mass flow zero by $\beta_{t,0}$.

2.6 Model validation

The present section is devoted to analyze model accuracy by comparison against a wide set of experimental data measured at the test bench on a small automotive Diesel engine equipped with common-rail multijet injection system, EGR system and VGT. The engine data sheet is shown in Table 2.2

The model accuracy has been evaluated via comparison between predicted and measured in-cylinder pressure and turbine inlet temperature in a wide engine operating range

Table 2.2 Data sheet of the reference engine

FIAT 1.3 l COMMON-RAIL MULTI-JET ENGINE	
Cycle	Diesel
Number of stroke	4
Max power [kW]	66 @ 4000 rpm
Max torque [Nm]	200 @ 1750 rpm
Number of cylinders	4
Disposition	In line
Bore [mm]	69.6
Stroke [mm]	82
Displacement [cm^3]	1248
Compression ratio	17.6
Rod/crank ratio	0.3122
European emission standard	EURO 5

. Then the overall experimental data set was composed of 34 operating conditions, measured with engine speed ranging from 1000 to 4500 [rpm], BMEP ranging from 1 [bar] to full load, EGR rate ranging from 0 to 30 % and in correspondence of single, double or multiple fuel injections. Figure 2.27 - Figure 2.34 show the comparison between predicted and measured in-cylinder pressure and apparent heat release rate traces for four engine operating conditions, with different engine speed, load, number of fuel injection and EGR rate. In all cases the model exhibits a good accuracy in predicting the engine cycle, even in the most

critical conditions in case of high EGR rate (i.e. Figure 2.33). The model accuracy on the whole data set is shown in Figure 2.35 where the comparison between measured and predicted gross IMEP is shown. The figure evidences a good agreement with a correlation index R^2 equal to 0.9947. Figure 2.36 shows the comparison between measured and predicted turbine inlet temperature for the whole experimental data set, with a correlation index R^2 equal to 0.9964. Despite the assumption of ideal open-valve cycle, the results evidence the good accuracy of the model in predicting the gas temperature in the exhaust manifold. It is worth noting that the results exhibit the good features of the overall model that allows taking into account the impact of engine control variables (i.e. injection pattern, EGR, VGT) on performance, emissions and exhaust temperature which has a key role on the activation/efficiency of the after-treatment devices.

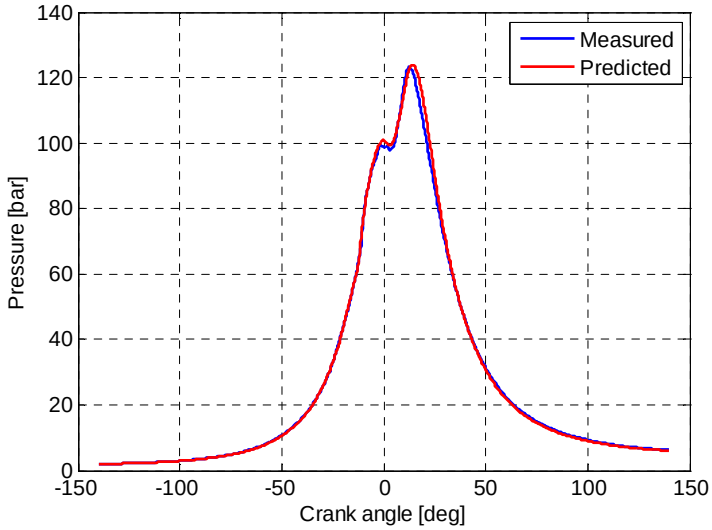

Figure 2.27 Comparison between measured and predicted in-cylinder pressure. Engine speed=1500 rpm, BMEP=13 bar, EGR=0%

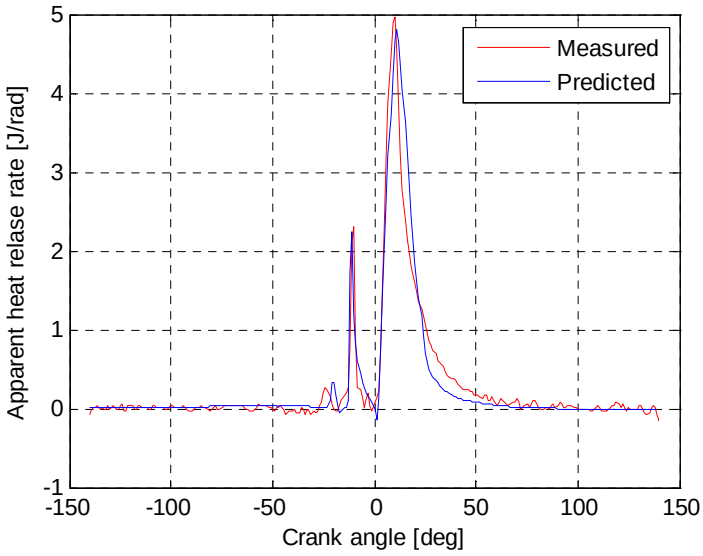

Figure 2.28 Comparison between measured and predicted heat release rate. Engine speed=1500 rpm, BMEP=13 bar, EGR=0%

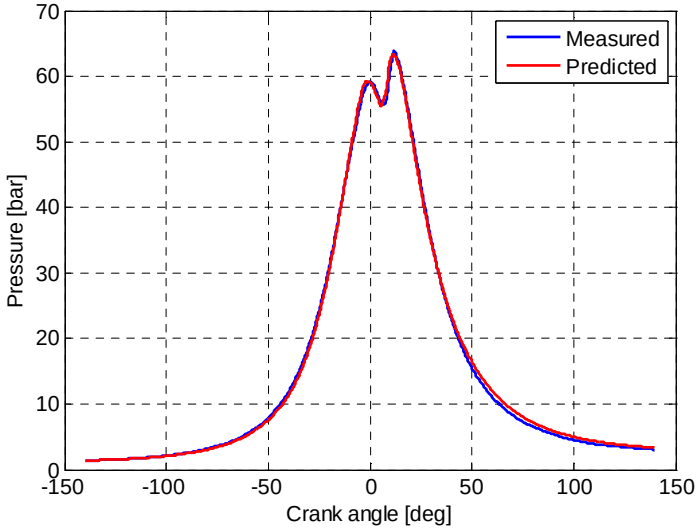

Figure 2.29 Comparison between measured and predicted in-cylinder pressure. Engine speed=2000 rpm, BMEP=13 bar, EGR=12%

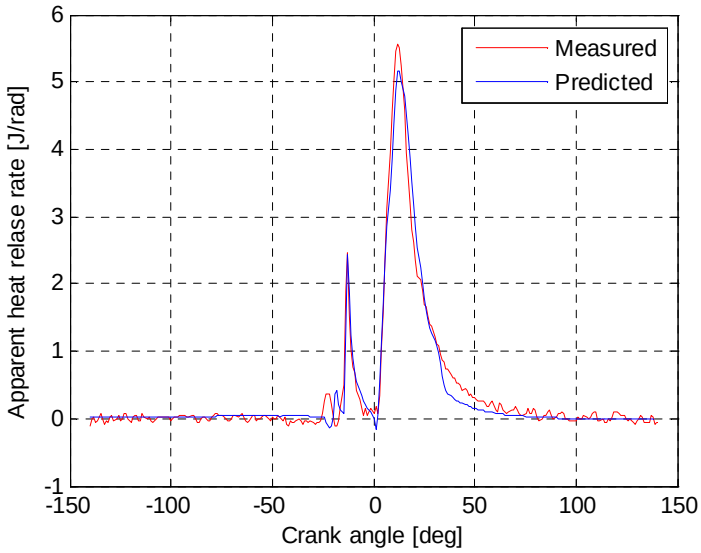

Figure 2.30 Comparison between measured and predicted heat release rate. Engine speed=2000 rpm, BMEP=13 bar, EGR=12%

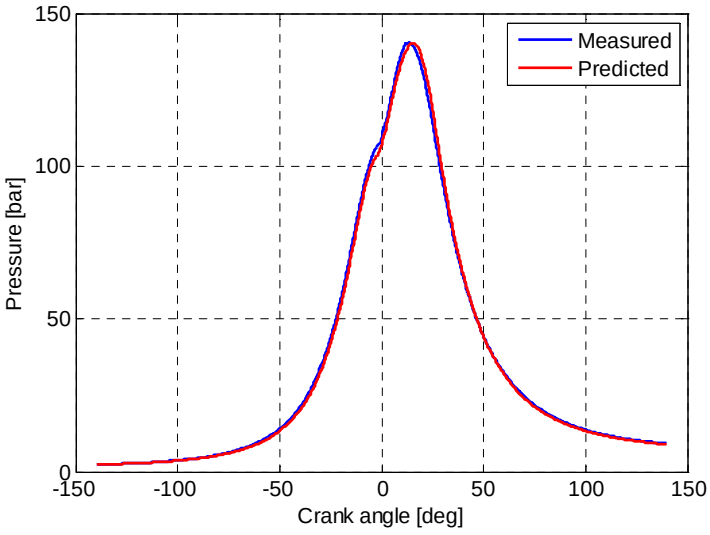

Figure 2.31 Comparison between measured and predicted in-cylinder pressure. Engine speed=2500 rpm, BMEP=19 bar, EGR=0%

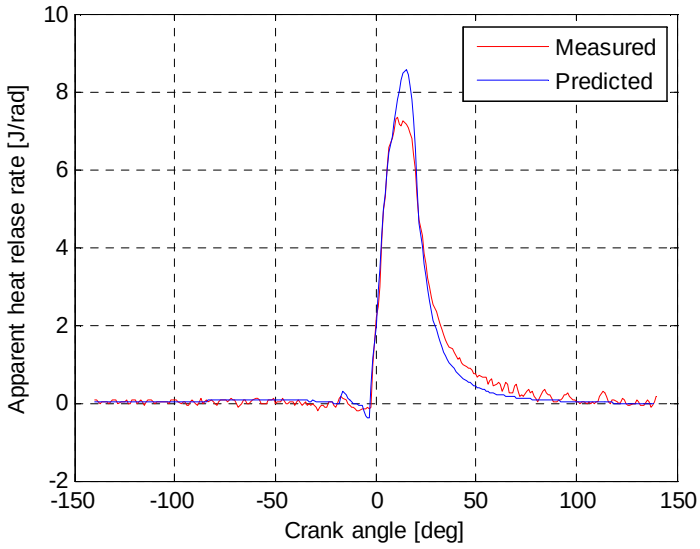

Figure 2.32 Comparison between measured and predicted heat release rate. Engine speed=2500 rpm, BMEP=19 bar, EGR=0%

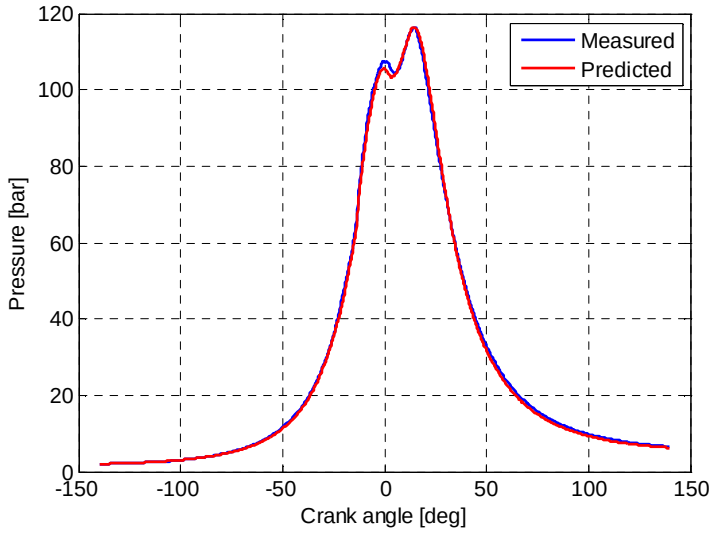

Figure 2.33 Comparison between measured and predicted in-cylinder pressure. Engine speed=3000 rpm, BMEP=4 bar, EGR=30%

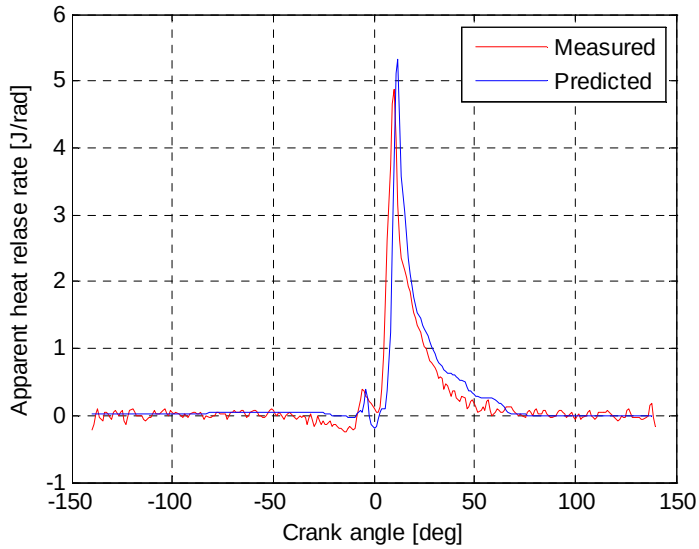

Figure 2.34 Comparison between measured and predicted heat release rate. Engine speed=3000 rpm, BMEP=4 bar, EGR=30%

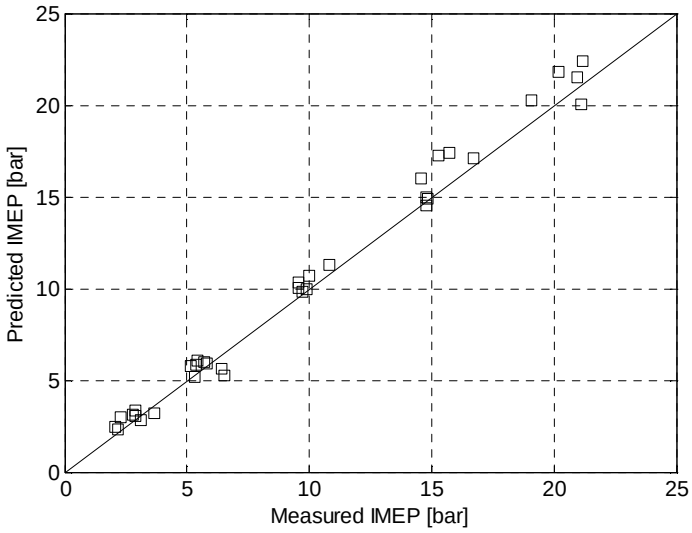

Figure 2.35 Comparison between measured and predicted Indicated mean Effective Pressure (IMEP) for the whole set of experimental data. R^2=0.9947

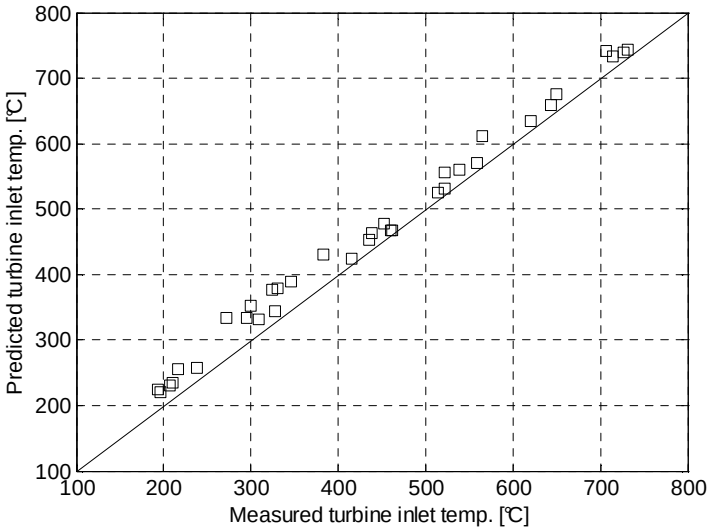

Figure 2.36 Comparison between measured and predicted turbine inlet temperature. R^2=0.9964

2.7 Optimization analysis

The optimization analysis is aimed at tuning the engine control variables in steady state operation to minimize the exhaust emissions with some constraints on performance and fuel consumption. Nevertheless the trade off between NO and soot emissions makes this target an arduous task, due to the need to simultaneously minimize both pollutants. Furthermore, the recourse to after treatment devices for particulate matter (e.g. Diesel Particulate Filter - DPF) or NO_x (e.g. DeNox catalyst, Selective Catalyst Reducer - SCR), can address the control design toward the minimization of just one of the two pollutants. In the current analysis the optimization was performed by targeting the minimum NO emissions assuming the feasibility of a successful after-treatment reduction of engine soot. This choice is supported by considering that DPF exhibits higher conversion efficiency than DeNOx catalysts and relatively easier and cheaper management than SCR, that needs additional and expensive components for the UREA management.

The minimization was carried out by optimizing the control variables

that are supposed to mainly affect the NO emissions, namely Start of Injection (SOI) and injected fuel amount (V_{inj}) of the main injection, EGR rate and VGT actuator (ξ). The optimization analysis was performed in four operating conditions selected among those of interest for the ECE/EUDC test driving cycle and reported in Table 2.3. Constraints were introduced to impose:

- constant IMEP during optimization in order to maintain the reference load condition for each test case;
- turbine outlet temperature greater than a threshold to ensure suitable oxidation efficiency in the pre-catalyst;
- limitation of soot increase with respect to the reference condition.

Table 2.3 Operating conditions selected as test cases for the optimization analysis

Test Case	Engine speed [rpm]	BMEP [bar]
1	1500	8
2	2000	8
3	2500	13
4	3000	13

Although soot emissions are supposed to be oxidized in the DPF, this latter constrain is introduced because measurement of pollutants along the test cycle include regeneration as well; therefore limitation of engine pollutants is always appreciated, regardless to after-treatment devices.

The following formulation is then assumed for the constrained minimization problem:

$$\begin{cases} \min\limits_{V_{inj},SOI,EGR,\xi} NO \\ \Delta Soot \le 5\% \\ \Delta IMEP \le 1\% \\ T_{out\_T} \ge 350°C \end{cases} \tag{2.53}$$

From eq. (2.53) it emerges that soot increase and IMEP variation are

restrained within 5% and 1%, while the turbine outlet temperature is imposed to be greater than 350 °C which is a safe threshold for efficient conversion in the after-treatment devices (e.g. DPF and/or De NOx catalysts).

The results of the optimization analysis are presented in Figure 2.37 - Figure 2.40 that show the comparison between initial and optimized engine emissions and control variables. Figure 2.37 and Figure 2.38 evidence that engine NO emissions are reduced in all conditions and that such reduction is achieved by an increase of EGR, that is more effective for the 4^{th} case where the benefit on NO emissions appears greater. These results can be explained by considering the impact of EGR on the in-cylinder temperature reduction which in turn inhibits the NO formation governed by kinetics. On the other hand the lower temperature and oxygen content following the greater EGR rate inhibits particles oxidation with a negative impact on soot emissions. Nevertheless the constraint imposed in the optimization problem (eq. (2.53)) allows bounding the soot increase within 5 % as shown in Figure 2.40.Figure 2.39 shows that in order to overcome the IMEP reduction following the EGR increase, the main injection is advanced, particularly in the last two cases due to the greater EGR upgrade. Actually the earlier SOI allows compensating for the longer ignition delay thus resulting in a more suitable heat release rate and greater in-cylinder pressure.

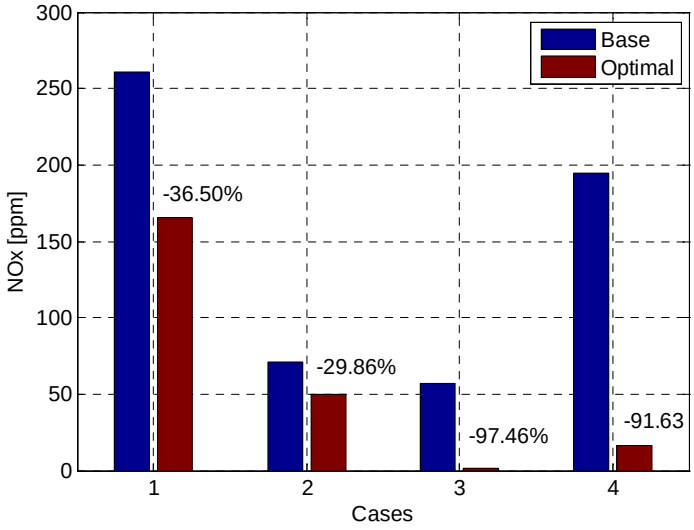

Figure 2.37 Optimization results: NO engine emissions in case of base and optimal control variables

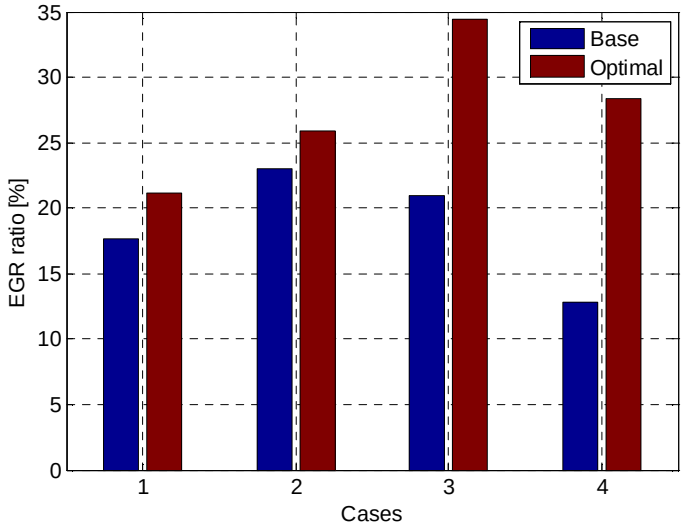

Figure 2.38 Optimization results: EGR rate in case of base and optimal control variables

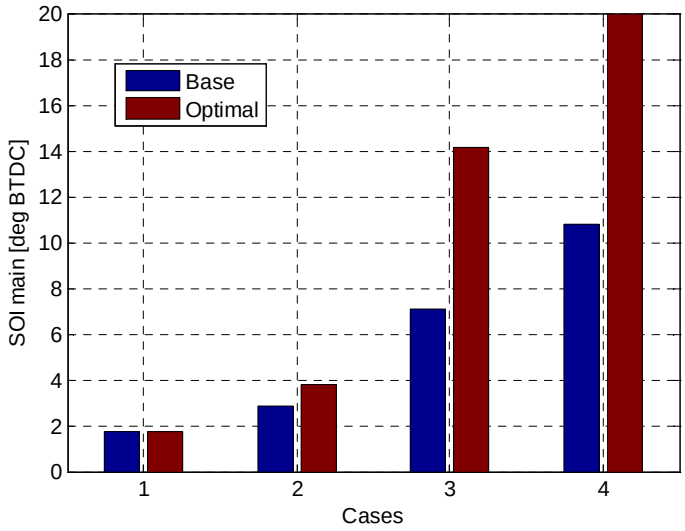

Figure 2.39 Optimization results: SOI for the main injection engine emissions in case of base and optimal control variables

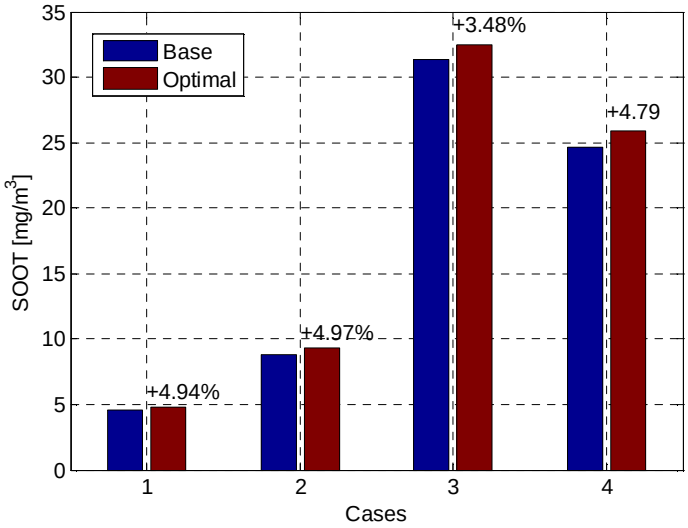

Figure 2.40 Optimization results: Soot emissions in case of base and optimal control variables

CHAPTER 3

Heavy-duty CNG engine

Compressed natural gas has proven to be a concrete alternative to gasoline and diesel fuels for vehicle propulsion. The mixed-fuel technology enables the usage of CNG also in Diesel engine with a reduction of both nitrogen oxides (NO_x) and particulate matter (PM) without increasing hydrocarbons (HC) and carbon monoxide (CO), though a strong effort is needed to design the engine control system. At the present time, most of CNG engines operate in spark ignition (SI) mode, for both light and heavy-duty applications. Particularly in this latter case the typical disadvantages of CNG (fuel tank weight and allocation) are overcome because of the wide space availability and the small relative weight increase. Moreover in case of public transportation in urban areas, the route is scheduled and therefore the NG option can be chosen according to the autonomy range. CNG wide inflammability limits enhances lean burn operation with benefits on efficiency and thermal stress. Nevertheless, to assure a good level of performance, an increase of NO_x and HC emissions is detected, due to poor catalyst conversion efficiency in case of lean mixture and low temperature, respectively [50]. For this reason most of CNG engines operate with stoichiometric mixture and are equipped with three way catalyst and closed-loop lambda control. The drawback of this configuration is represented by lower efficiency, due to engine throttling, and high in-cylinder temperature that results in thermal stress of engine components [50]. In order to overcome this issue and increase engine reliability, exhaust gas recirculation has been proved to be a good option [83] [37]. In fact, this technology allows reducing the thermal load of components particularly stressed (e.g. valves, engine and piston head) especially for diesel derived engines that are designed for lower temperature than SI engines. In addition EGR enhances engine efficiency for reduction in pumping and thermal losses. The recourse to EGR allows maintaining the stoichiometric operation with closed-loop lambda control, however it’s clear that the introduction of an additional control parameter imposes a reformulation of the engine control

strategies. Particularly an optimization of control maps for spark advance, throttling, EGR and boost pressure is mandatory to gain benefits in terms of fuel consumption, catalyst efficiency and thermal stress. Simulation models have been proven to be valid tools to design, calibrate and optimize engine control strategies, due to the stressed and continuous need to improve fuel economy and emissions. Their role in this process is more and more evident due to the manufacturers need to speed up the time to market of new engines/vehicles and to reduce the recourse to time consuming experiments. Many different modeling approaches have been proposed in literature, characterized by substantial differences in structure, goals and complexity [62][92]. A significant number of them are devoted to design engine control strategies and to develop new engine control technologies. They range from input-output black-box models, to gray-box mean-value models [61][9], with a simplified description of the most relevant physical processes, up to quasi-dimensional models for simulating engine combustion and emissions [10] or 1D models for the prediction of the unsteady gas flow in intake and exhaust pipes [99][85][26]. All these classes of model substantially differ in terms of computational time and experimental data required: for the validation of the simplest black-box models, hundreds or thousands of engine data could be needed to compensate for the lack of physical information, resulting in high experimental effort and lower model flexibility. On the other hand, the computational time of phenomenological models is not compatible with real-time application for control purposes. Hierarchical model structures have been proposed in literature to meet both reasonable computing time and limited experimental effort. They are based on a suitable mixed approach, in order to combine the advantages of different modeling techniques [11]. The approach followed in the present work is based on the integration of a commercial solver for engine simulation into Matlab/Simulink® environment to face with an optimization algorithm (co-simulation). In this framework, the commercial code simulates the 1D unsteady gas flow in intake and exhaust pipes and the engine combustion, thus providing the data to build-up the objective function of the optimization algorithm. This latter is in charge to evaluate the input parameters for the engine simulator (i.e. engine control parameters) that iteratively will lead to meet the target engine performance. The work is intended to furnish a detailed description of the methodology followed in order to:

- extend engine model accuracy in a wide operating range through proper identification analysis;
- integrate physical simulation models with optimization algorithms and prove the effectiveness of engine simulation for control maps optimization.

3.1 Modeling approach

Several commercial solvers for engine simulation are available, among the others Wave® from Ricardo North America, Boost® from Avl and GT-Power® from Gamma Technologies. This latter was used for the present application to simulate engine breathing and combustion processes. The fluid dynamics in all engine ducts and manifolds is approximated via a finite volume method, by discretizing the intake/exhaust system into many small sub-volumes and solving the equations of conservation of mass, momentum and energy [21]. These equations are integrated in space by means of a staggered mesh and in time with a variable time step based on the explicit technique with time step governed by the Courant condition [87].

For the in-cylinder intake and exhaust process, the time-dependent simulation is based upon the solution of the equations for mass and energy [62][92][45]. The combustion process was simulated assuming a two zone discretization and estimating the burned fuel fraction by means of the well known Wiebe function [45]:

$$x(\vartheta) = 1 - \exp\left[-a\left(\frac{\vartheta - \vartheta_s}{\vartheta_b} \right)^n \right] \tag{3.1}$$

where ϑ_s is the spark advance angle, ϑ_b is the combustion duration, a and n are pre-exponential and exponential parameters, respectively.

This approach allows speeding-up the computational time though, being based on an empirical formulation, the Wiebe function lacks any physical content.

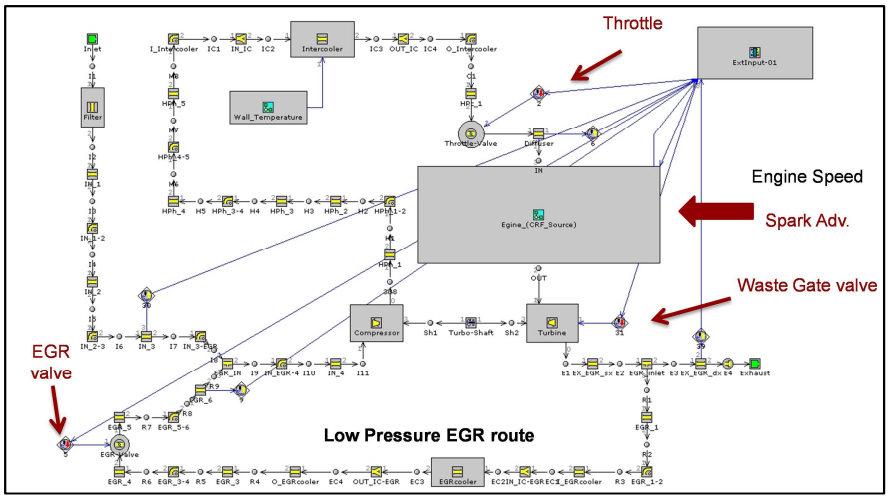

Figure 3.1 Scheme of the engine model developed in GT-Power®. The red arrows indicate the model input variables supplied by the Matlab/Simulink environment in the co-simulation process

Therefore identification of parameters ϑ_b, a and n is mandatory to achieve satisfactory accuracy in a wide engine operating range. This analysis will be presented in a next section. The dimensional and thermodynamic models provide among the others, in-cylinder pressure as well as thermodynamic and chemical properties of burned and unburned gases along the engine cycle. These data represent the boundary condition for the optimization algorithm, as it will be described in a later section. Figure 3.1 depicts a scheme of the engine model developed in GT-Power®, comprehensive of intake and exhaust systems, turbocharger and low pressure EGR circuit. The external input variables supplied by the Matlab/Simulink® environment in the co-simulation process are evidenced by the red arrows.

3.2 Reference engine and experimental set-up

The reference engine considered for the present work is a heavy-duty spark ignition engine, fueled with CNG, whose main characteristics are reported in Table 3.1. The engine was derived from a turbocharged Diesel engine that was supposed to operate in lean burn condition with low

combustion temperature.

Table 3.1 Data sheet of the reference engine

IVECO CURSOR 8 CNG ENGINE	
Rated power [kw]	200 @ 2100 rpm
Max. torque [Nm]	1100 @ 1100-1650 rpm
Number of cylinders	6
Disposition	In line
Bore [mm]	115
Stroke [mm]	125
Displacement [l]	6.8
Compression ratio	11:1

As the fuel was turned to CNG and the combustion was operated stoichiometric, to meet satisfactory TWC efficiency, an inlet charge dilution with inert gas was needed to decrease combustion temperature and reduce the thermal stress of some engine components (head, valves). Figure 3.2 shows the cooled low pressure EGR system the engine was equipped with to accomplish this task. The engine was installed on a dynamic test bed at Istituto Motori laboratories. A large set of experimental data were collected in steady-state operation, ranging the engine speed from 1100 to 2000 rpm, the load from 160 Nm to 1100 Nm and the EGR valve opening from 0 to 50%.

Furthermore a research ECU enabled the access to the main control parameters (air/fuel mixture, spark advance, wastegate duty cycle etc.) during engine operation. The measured data, both instantaneous (i.e. in-cylinder pressure) and mean (i.e. brake torque and fuel consumption) were used for identification analysis and model validation as it will be discussed in the next sections.

Figure 3.2 Cooled low pressure EGR system on the CGN engine

3.3 Parameters identification

As previously mentioned identification of Wiebe parameters is mandatory to achieve satisfactory model accuracy in the wide engine operation range investigated for the present work. This is particularly true in case of high EGR rate that gives rise to a significant variation of the heat release rate due to greater ignition delay and slower combustion process. The analysis was carried out vs. 33 operating conditions, ranging engine load from medium to high at various engine speeds and EGR rates. Engine operation at low load was not considered since EGR would be useless in such conditions. The three model parameters n, a and ϑ_b (see eq. (3.1)) were simultaneously identified, for each operating condition, by a least square technique, comparing predicted and apparent heat release rate derived from in-cylinder pressure measurements. Afterwards, in order to enhance model prediction in the whole engine operating range, multiple linear regressions were derived, expressing the parameters as function of operating and control variables:

$$n = k_1 + k_2 \cdot rpm^2 + k_3 \cdot EGR^2 + k_4 \cdot \vartheta_s \tag{3.2}$$

$$\vartheta_b = k_1 + k_2 \cdot rpm + k_3 \cdot p_b^2 + \frac{k_4}{p_b} + k_5 \cdot EGR^2 \tag{3.3}$$

A step-wise method was used to identify the more suitable functional form of the linear regressions, expressed by eq. (3.2) and (3.3) [93]. Particularly the resulting multiple regressions express dependence of parameter n on engine speed (rpm), EGR rate and spark advance (ϑ_s), and parameter ϑ_b on engine speed, EGR rate and boost pressure (p_b). Concerning the pre-esponential parameter a, a significant cross correlation was found against parameter n and the following relationship was identified:

$$a = k_1 + k_2 \cdot n + \frac{k_3}{n} \tag{3.4}$$

The identified coefficients k_i are reported in Table 3.2 for each parameter, together with the correlation index R between predicted and optimal values. The good accuracy achieved by the regression analysis is also evidenced by Figure 3.3 - Figure 3.6 that show comparison between experimental and predicted heat release rate, for three engine operating conditions with different engine speed, torque and EGR rate. It is worth noting the longer combustion duration in the former and last cases (i.e. Figure 3.3 and Figure 3.6) with respect to the second and third (i.e. Figure 3.4 and Figure 3.5), due to the higher EGR rate that results in a late combustion, over 45° ATDC.

Table 3.2 Coefficients of the polynomial regressions for the estimation of parameters n, a and θ_b

	k_1	k_2	k_3	k_4	k_5	R
n	4.28	$-4.68\ 10^{-8}$	$-1.6\ 10^{-3}$	-0.0459		0.92
a	- 4.20	0.392	11.4			0.94
θ_b	11.0	$3.40\ 10^{-3}$	4.20	0.177	0.030	0.99

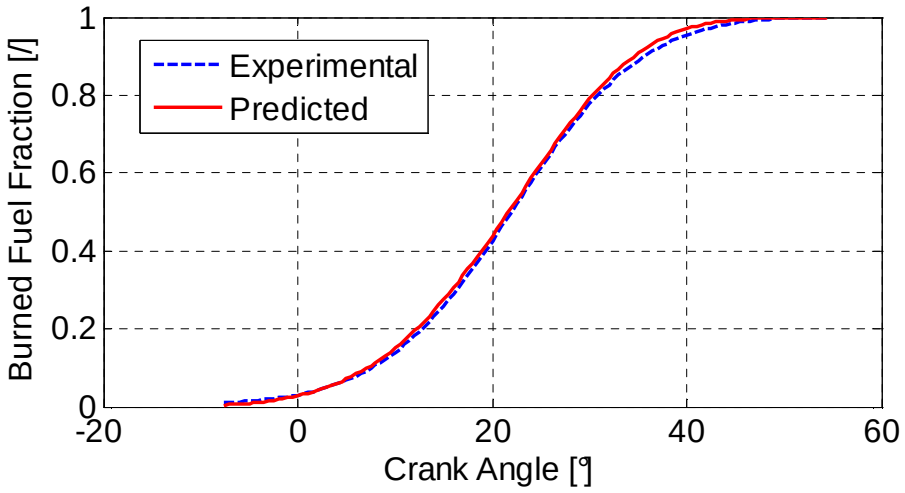

Figure 3.3 Predicted and experimental burned fuel fraction vs. engine crank angle. Engine speed=11000 rpm, brake torque=640 Nm, EGR rate=20%

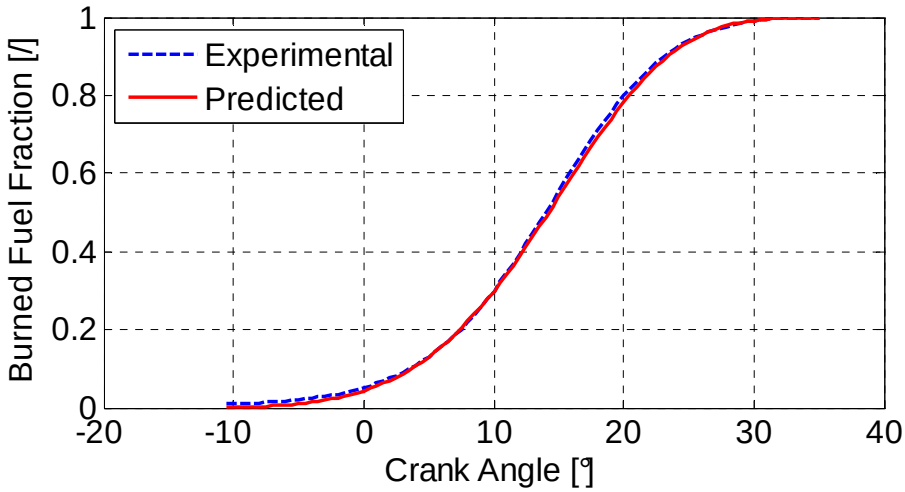

Figure 3.4 Predicted and experimental burned fuel fraction vs. engine crank angle. Engine speed=1500 rpm, brake torque=850 Nm, EGR rate=7%

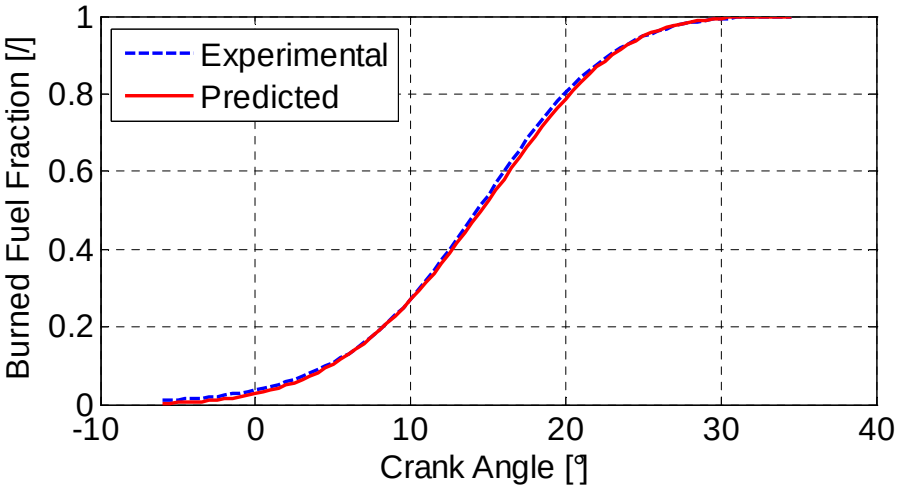

Figure 3.5 Predicted and experimental burned fuel fraction vs. engine crank angle. Engine speed=1500 rpm, brake torque=1050 Nm, EGR rate=0%

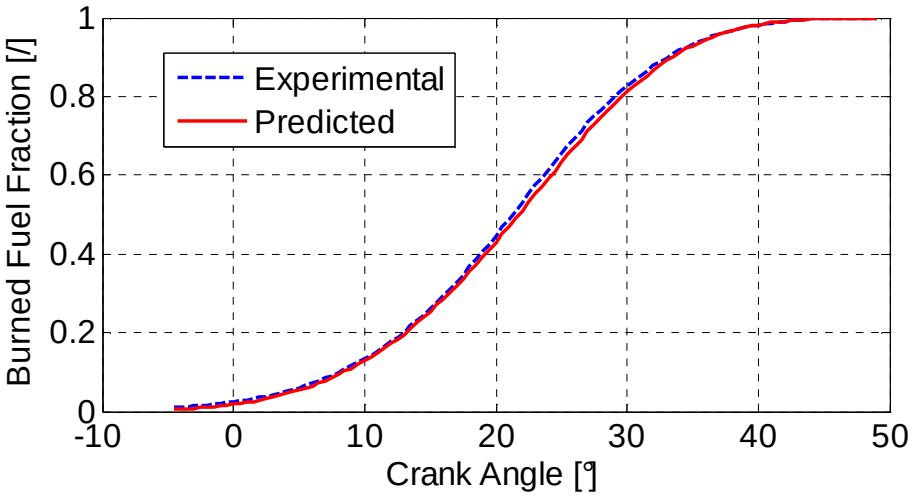

Figure 3.6 Predicted and experimental burned fuel fraction vs. engine crank angle. Engine speed=2000 rpm, brake torque=900 Nm, EGR rate=13%

3.4 Model validation

Model accuracy was validated by means of comparison between predicted and measured boost pressure, brake torque and in-cylinder pressure. The analysis was carried out at 12 engine operating conditions, corresponding to medium and high load at 1100, 1500 and 2000 rpm, with and without EGR rate. Figure 3.7 and Figure 3.8 show a comparison between predicted and measured boost pressure and brake torque for all the 12 conditions considered for model validation. The good accuracy achieved is evidenced by the correlation indexes R equal to 0.989 and 0.992, respectively. Figure 3.9 - Figure 3.12 show the comparison between predicted and measured in-cylinder pressure for four test cases, referred to two different engine working conditions, with and without EGR. In all cases the pressure peak is well predicted, both in amplitude and in position, confirming the accuracy of the regression models developed to predict the heat release rate and the effectiveness of the whole engine model to predict engine performance at various operating conditions.

3.5 Optimization analysis

The introduction of the EGR system to limit combustion temperature and prevent the thermal stress of engine components imposes a reformulation of engine control variables. This task was accomplished by means of a constrained optimization analysis aimed at minimizing fuel consumption as function of the engine control variables, namely spark advance (ϑ_s), EGR rate and wastegate valve opening (*WG*). In order to minimize the engine losses due to intake air throttling, the throttle was assumed fully open in all conditions.

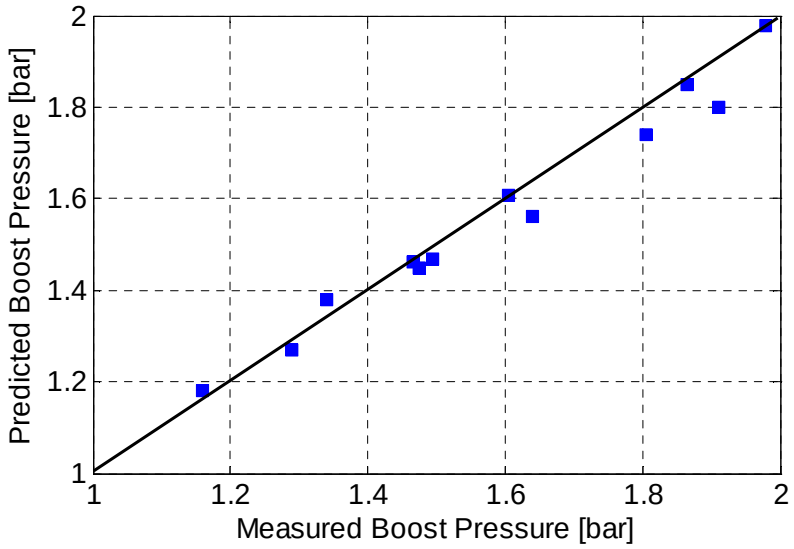

Figure 3.7 Comparison between measured and predicted boost pressure in the 12 operating conditions considered for model validation. R=0.989

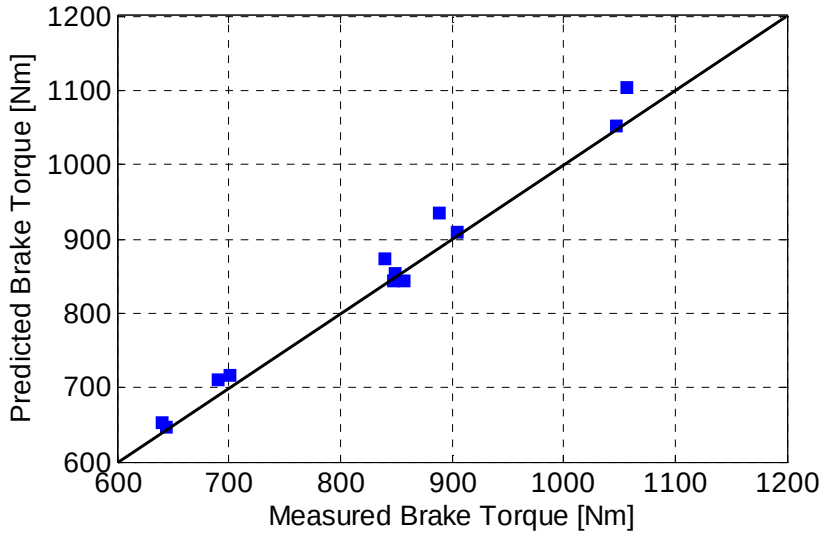

Figure 3.8 Comparison between measured and predicted brake torque in the 12 operating conditions considered for model validation. R=0.992

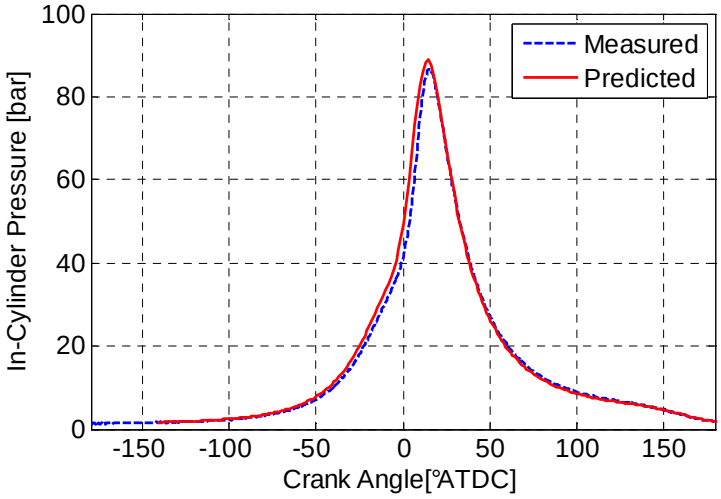

Figure 3.9 Measured and predicted in-cylinder pressure vs. Engine crank angle. Engine speed=1100 rpm, brake torque=850 Nm, EGR rate=0%

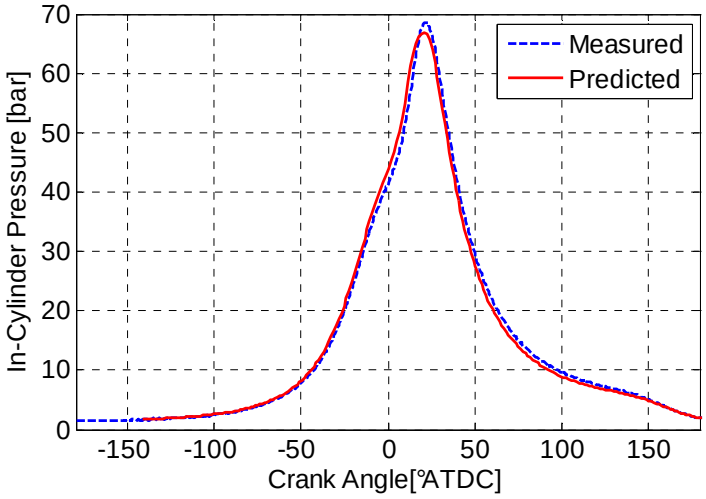

Figure 3.10 Measured and predicted in-cylinder pressure vs. engine crank angle. Engine speed=1100 rpm, brake torque=850 Nm, EGR rate=13%

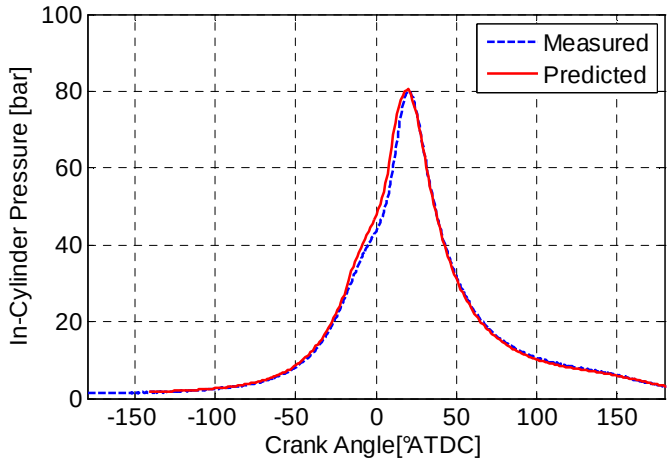

Figure 3.11 Measured and predicted in-cylinder pressure vs. engine crank angle. Engine speed=2000 rpm, brake torque=900 Nm, EGR rate=0%

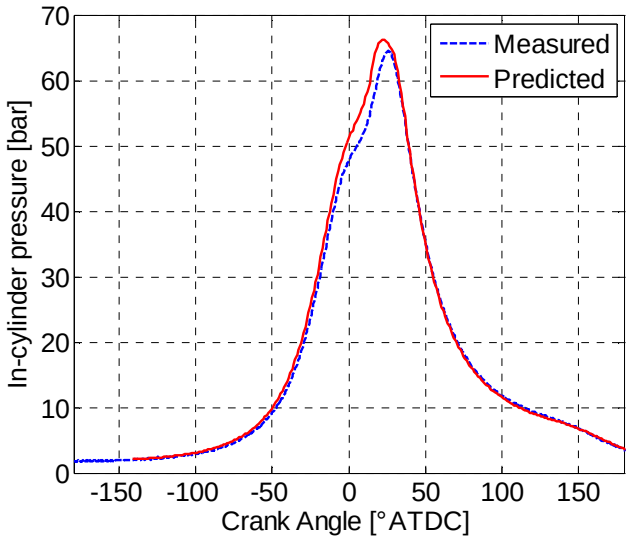

Figure 3.12 Measured and predicted in-cylinder pressure vs. engine crank angle. Engine speed=2000 rpm, brake torque=900 Nm, EGR rate=13%

The constraint to be satisfied refers to the mentioned need to limit the thermal stress of engine and piston head. This issue was faced by introducing a Thermal Load Factor (TLF), proportional to the heat power transferred to the cylinder wall which is expressed as:

$$\dot{Q}_w = S \cdot h_c \cdot \Delta T \tag{3.5}$$

where S is the heat transfer surface, h_c is the convective heat transfer coefficient (W/m^2K) and ΔT is the difference between gas and wall temperature. The heat transfer surface S is only dependent on engine geometry while, according to the correlation proposed by Woschni [62], the convective heat transfer coefficient h_c depends on engine operation through piston speed and in-cylinder pressure and temperature. The TLF was defined as proportional to the maximum value reached by the heat power along the engine cycle. Therefore, assuming that

1) the mean temperature difference ΔT can be correlated with the maximum in-cylinder gas temperature Tmax;
2) the mentioned dependence of h_c on engine operation can be condensed as function of fuel flow rate.

From eq. (3.5) the TLF was analytically expressed as:

$$TLF = \dot{m}_{fuel} \cdot T_{max} \tag{3.6}$$

It is worth noting that both fuel flow rate and in-cylinder temperature in eq. (3.6) are dependent on engine operation that is in turn affected by control variables. Figure 3.13 shows the normalized TLF, estimated from model simulations in case of engine speed ranging from 1100 to 2000 rpm without EGR. The simulations were carried out at full load (i.e. 1100 Nm) except for the condition at 2000 rpm where a max torque of 900 Nm was imposed to limit the maximum power. As expected from eq. (3.6), the most critical conditions are those at higher speed, where the thermal power transferred to the cylinder walls is greater. In order to set the TLF threshold to prevent from thermal stress, a set of thermocouples was located close to the engine head and temperature measurements were carried out at the operating conditions mentioned above (i.e. Figure 3.13).

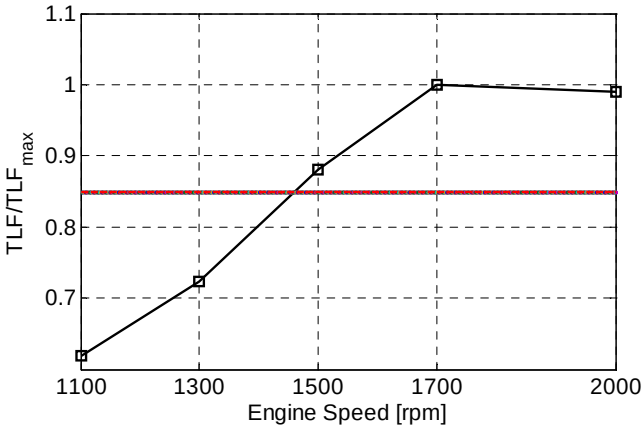

Figure 3.13 Estimation of the TLF at full load without EGR vs. engine speed

The experimental observations suggested to consider the temperature reached at 1500 rpm as safe upper limit, therefore the TLF relative value of 0.85 was chosen as threshold value to be considered in the optimization analysis.

The optimization analysis was performed in five operating conditions selected as the most critical with respect to the TLF, among the reference ETC for heavy-duty vehicles: 600, 800 and 1100 Nm at 1500 rpm, 1100 Nm at 1700 rpm and 900 Nm at 2000 rpm, as it is shown in Figure 3.14.

Apart from the TLF, a further constraint was introduced to impose an almost constant Brake Torque (BT) during optimization, in order to maintain constant engine speed and load with respect to the reference condition without EGR.

Finally, the following constrained minimization problem was solved, by a classical second order Quasi-Newton algorithm [51]:

$$\begin{cases} \min \dot{m}_f \left(\vartheta_s, EGR, WG \right) \\ \Delta BT \leq 1\% \\ TLF \,/\, TLF_{\max} \leq 0.85 \end{cases} \tag{3.7}$$

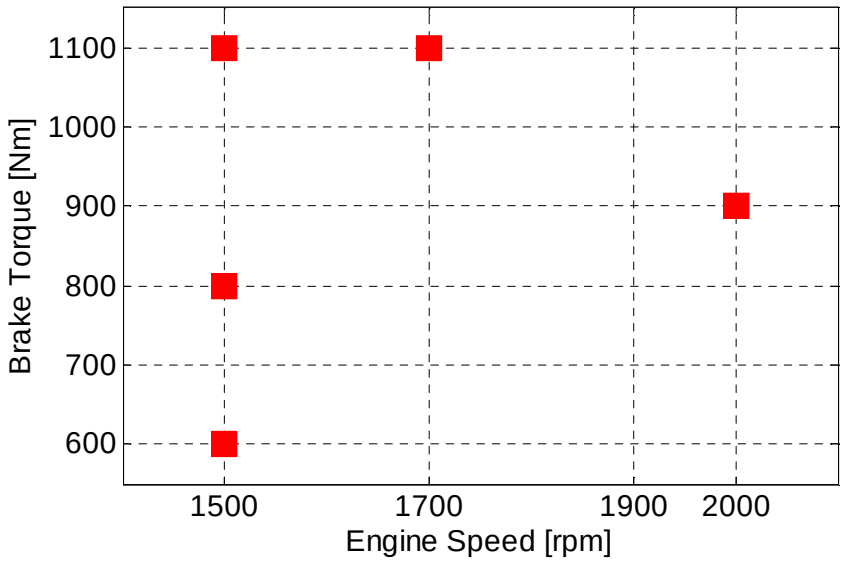

Figure 3.14 Load-speed map of the operating conditions considered as test cases for the optimization analysis

The optimization analysis was carried out by means of a co-simulation process in which the GT-Power® engine model was interfaced with the constrained minimization algorithm developed in Matlab/Simulink® environment. According to the scheme in Figure 3.15, for each of the five test cases considered, the minimization algorithm provides the control variables (i.e. ϑ_s, *EGR* and *WG*) for the engine model, that in turn feed-back the simulation results of interest, such as the variable to be minimized (i.e. fuel consumption) and those which have to meet the constraints (i.e. *BT* and *TLF*).

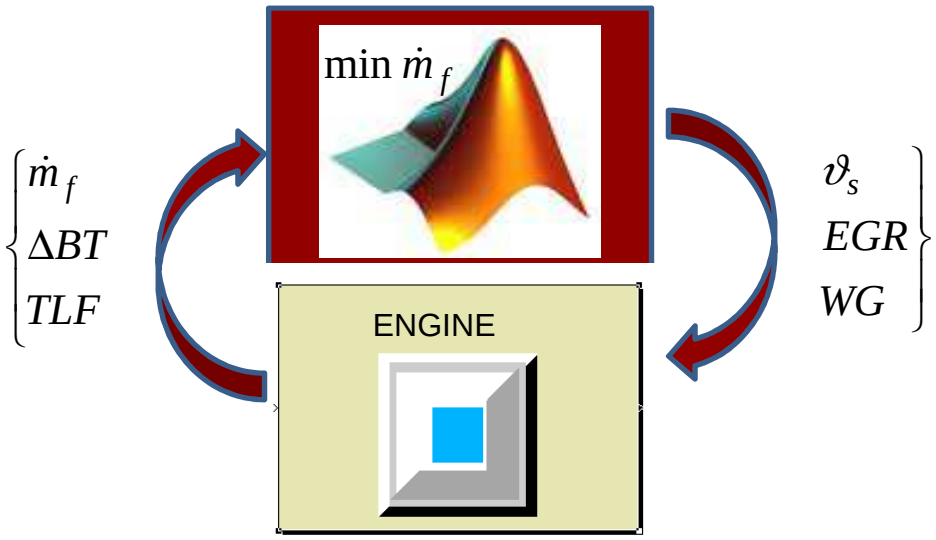

Figure 3.15 Scheme of the co-simulation process

The results of the optimization analysis are presented in Figure 3.16 - Figure 3.20 that show the values of TLF, BSFC and control variables (i.e. EGR rate, spark advance and WG) in case of base (i.e. without EGR) and optimized set-points. Figure 3.16 evidences that the TLF was reduced in all cases, especially the more critical ones (i.e. case 3, 4 and 5) where the initial values exceeded the threshold limit imposed to prevent from thermal stress. The BSFC was also reduced in all cases (see Figure 3.17) in a range between 3 % and 4.5 %. This reduction was due to the concurrent effects of increased throttle opening and WG closing (see Figure 3.20), that result in lower pumping losses and greater turbine work, respectively. More importantly, the EGR rate (see Figure 3.18) also contributed to the BSFC reduction, due to the reduced heat transfer to the cylinder wall following the in-cylinder temperature reduction. Figure 3.19 evidences the significant increase of spark advance, due to the need of compensating for the delaying effect of the EGR rate on the combustion process, thus ensuring an almost constant brake torque.

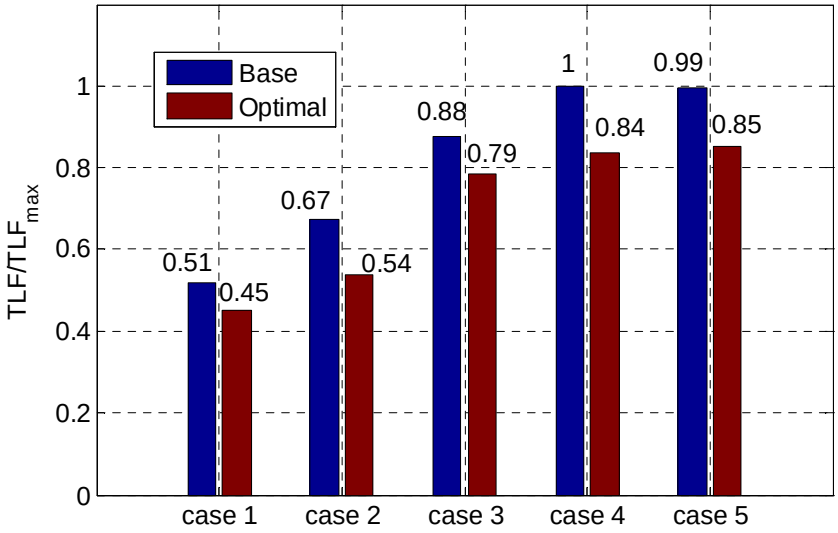

Figure 3.16 Optimization results: normalized TLF in case of base (no EGR) and optimal control variables

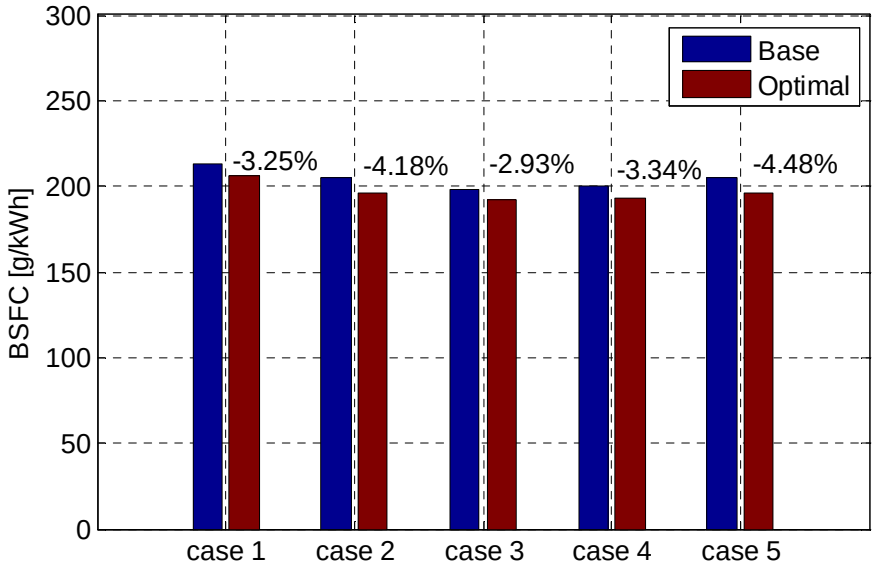

Figure 3.17 Optimization results: Brake Specific Fuel Consumption in case of base (no EGR) and optimal control variables

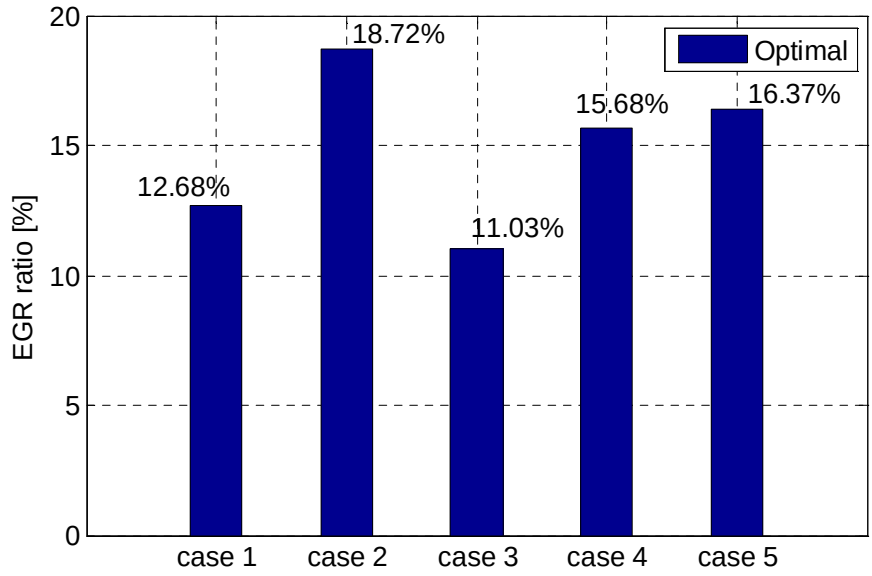

Figure 3.18 Optimization results: EGR rate in case of optimal control variables

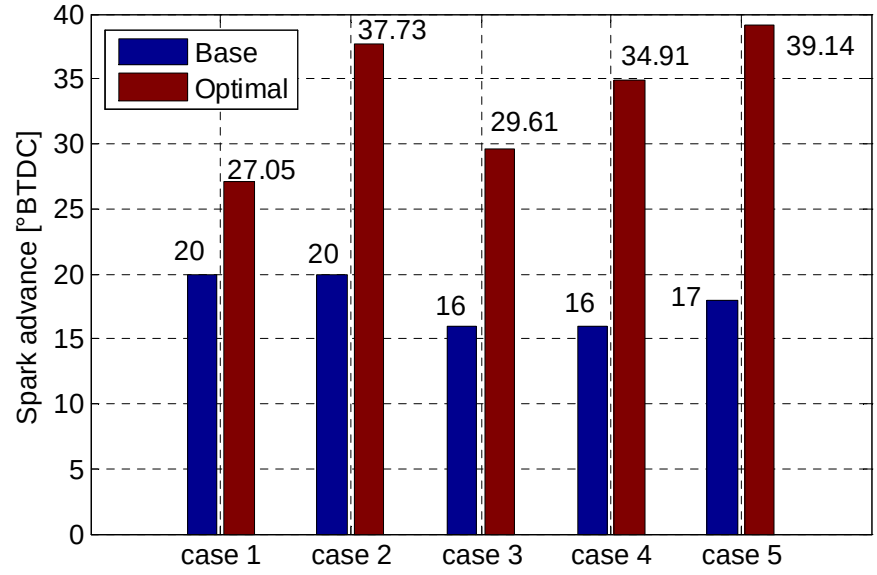

Figure 3.19 Optimization results: Spark advance in case of base (no EGR) and optimal control variables

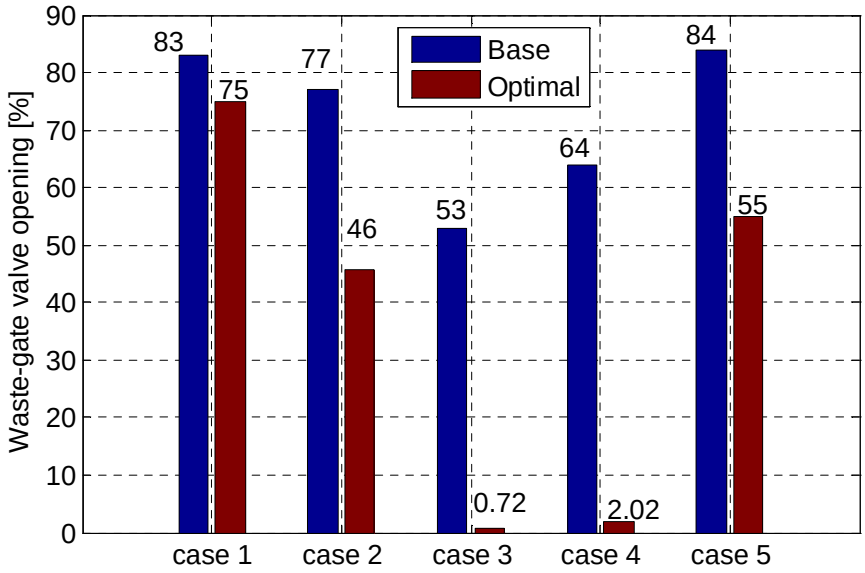

Figure 3.20 Optimization results: Waste-gate valve opening in case of base (no EGR) and optimal control variables

CHAPTER 4

Boost pressure control

The trend towards downsizing of internal combustion engines in the automotive industry has increased in recent years. The main goal is to decrease fuel consumption and emissions, while keeping the performance of the engine constant. A way of achieving this goal is the introduction of turbocharging, as proposed in [39][58][89]. By means of wastegate valve opening or closing, it is possible to control the flow through the turbine and thus the amount of energy available to compressor. Coordinated control of throttle and wastegate valves is important, since the control affects engine performance and efficiency [43][42].

As turbocharging develops, the demand on the wastegate valve control strategies increases. The wastegate valve actuation is usually performed by a pressure actuator. The actuator is connected to a solenoid valve that is electronically controlled by a PWM signal in order to reach the desired pressure in the actuator chamber. One important sub problem is that the system voltage can vary several Volt during driving which has a direct influence on the performance of the boost pressure controller. Figure 4.1 shows that a disturbance in supply voltage from 11.9 V to 11.1 V, causes an alteration in the chamber pressure of 2500 Pa which produces a change in wastegate valve position of about 10%. A boost pressure control system that follows the reference boost pressure has to be developed, while also rejecting the disturbance caused by system voltage changes

Next section briefly explains:

- the system layout of the two stage turbocharged gasoline engine, the operating principles of the pressure relief valve and its connection to the engine;
- the experimental data collected for modeling, together with the development of a physical including parameter identification and model validation;
- the wastegate valve position control focusing on the nonlinear compensator, its development and the obtained results;

- development the control system for the boost pressure in order to reach the desired pressure upstream the throttle valve in the intake manifold, pointing out the supply voltage disturbance rejection. The performance of the compensator and of the control system are demonstrated first using a complete Mean Value Engine Model (MVEM) of a Two Stage Turbo-Charged Spark Ignition (TSTCSI) engine, developed and validated in [41], and then on an engine in a test cell.

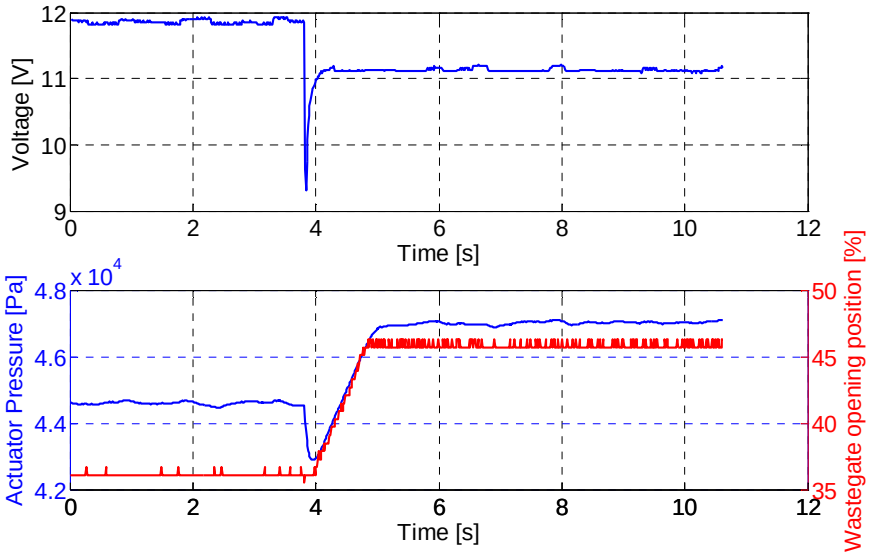

Figure 4.1 Effect of voltage disturbance on actuator chamber pressure and wastegate valve position

4.1 Mean value engine modeling

MVEM libraries have been designed with the aim of being flexible and reusable when building models for both naturally aspirated and turbocharged engines. Another design guideline has been to enable a modular design of the engine models and this is accomplished by ensuring that the implemented components adhere to simple rules concerning their causality. In particular the causality in these models for

NA engines and TC engines follow the principle of restrictions in series with control volumes, see [41] for a longer discussion on this topic. The control volumes have pressure and temperature as outputs, and the restrictions have mass flow and temperature of the flowing fluid as outputs. The components in the library is shown in Figure 4.2, where the upper components are components that have dynamic elements in them, i.e. they have states and this is marked by a shadowed block. There are also components that generate gas flows, engine torque, and some that influence temperature. Currently no generic components for turbo chargers are included in the library but they are planned to be included. However the generic equations used in these are described in the compressor and turbine sections in this document.

4.1.1. System decomposition and flow directions

A particular model for an engine is thus built up using control volumes in series with generalized flow restrictions (i.e. both restrictions and pumps). For the control volume there is only one type of model but for the generalized restrictions there are two main components, compressible and incompressible fluid. The implementations of the control volume and the two restrictions mentioned above all have an upstream and downstream side but they can handle flows in both directions. The convention that is used is described below. Through the engine there is a natural direction for the air and fuel flow, and these directions are used to define the upstream and downstream of the components. Some of the components implemented in the MVEM library do also handle unidirectional flows. In these components, that handle both flow directions, the following convention is used: A flow in the forward direction, from upstream to downstream, is positive, and a flow in the opposite direction is negative.

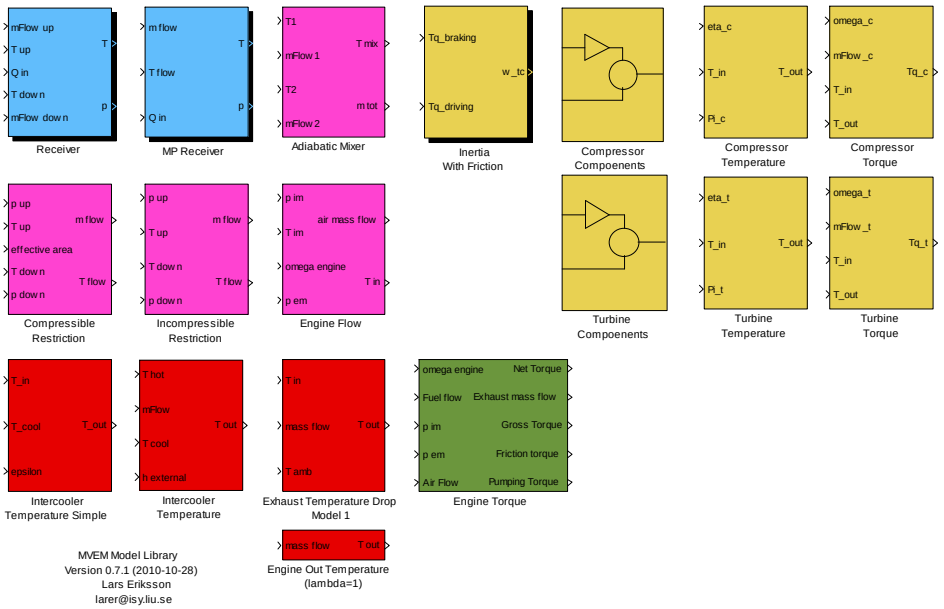

Figure 4.2 Top view of MVEN library. This top view shows the components that are utilized and reused when building engine models

4.2 System overview

Traditional turbocharged gasoline engines have a torque deficiency at low end engine speed. This comes from the trade-of between low end torque and maximum engine power since the compressor cannot supply a high boost pressure over the entire engine speed range.

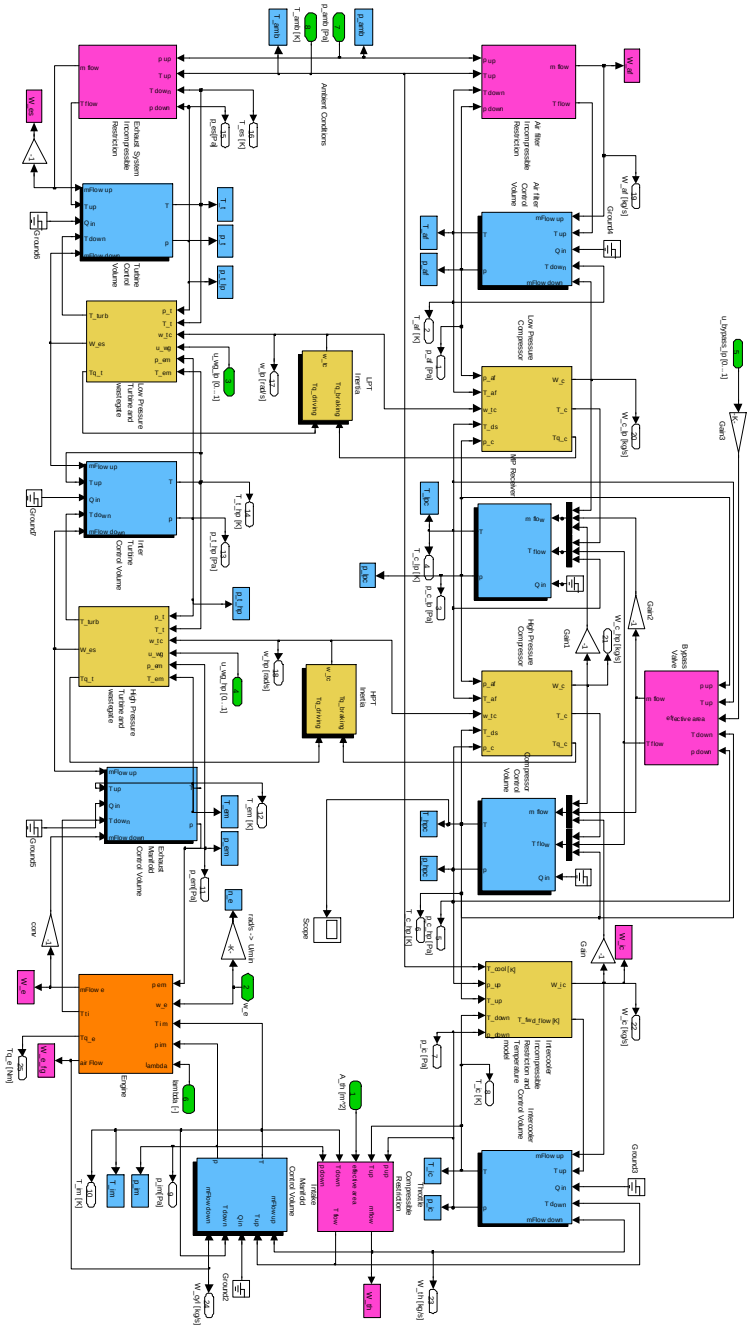

Figure 4.3 Mean Value Engine Model for a two stage turbocharger engine

One way to solve this problem, and get better driveability, is to use a two stage turbocharging system, allowing good performance in the full speed range of the engine.

4.2.1. Engine

The engine used for the experiments is a 2.0 liter GM four cylinder engine with direct injection, that has been equipped with a research two stage turbocharging system.

Figure 4.4 shows a sketch of the system. The advantage of this layout comes from the different sizes of the turbochargers, where the turbo of the low pressure stage is larger than the one of the high pressure stage. In this way, it is possible to utilize each turbocharger in its region of maximum efficiency.

For example, in a gasoline engine it is useful to divide the engine speed range in three regions: low speed (below 2000 rpm), medium speed (2000-3500 rpm) and high speed (above 3500 rpm). In the low speed region, where the mass flow is too small to power the larger low pressure stage, the smaller turbine and the smaller inertia of the high pressure stage allows high boost pressure and fast response. At high speed the high pressure compressor goes in the choke region and thus only the low pressure stage is used.

This strategy can be applied setting up the HPC by-pass valve and the HPT wastegate valve fully opened so as to completely by-pass the high pressure stage. In the middle region both turbochargers can be used in order to ensure a gradual transition between the two strategies. The operation of the wastegate and HPC bypass control valves is explained in the next section.

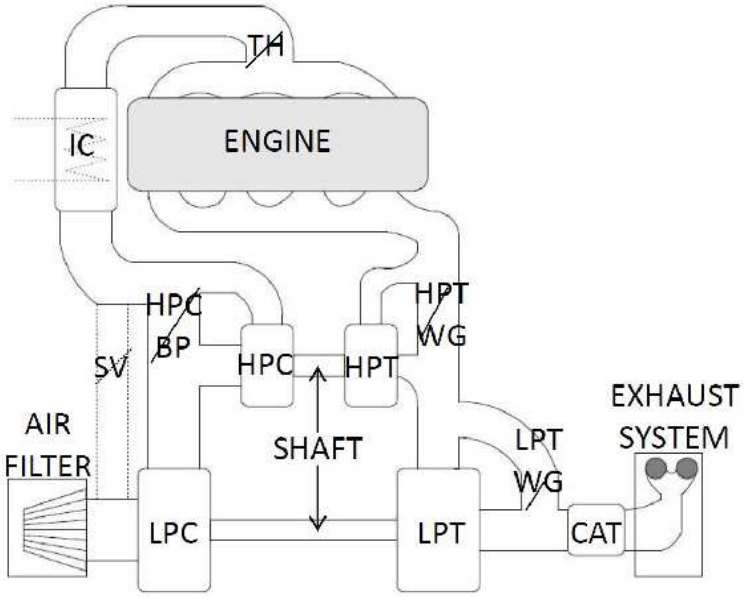

Figure 4.4 Two stage turbocharging system sketch. LPC, HPC, BP, SV, IC, TH, HPT, LPT, WG and CAT mean respectively low pressure compressor, high pressure compressor, by-pass, surge valve, intercooler, throttle, high pressure turbine, low pressure turbine, wastegate and catalyst

4.2.2. Actuation system

The main component of the actuation system is the solenoid valve that contains a plunger. The plunger position is controlled by the PWM signal and the valve is connected to other pneumatic components with three pipes, see Figure 4.5. On the solenoid the lowest pipe is connected to ambient air, the middle pipe to the actuator, and the top pipe to the vacuum tank. The valve controls the actuator chamber pressure and thereby the force on the membrane. Figure 4.6 illustrates the forces on the mechanical system that govern the membrane movement.

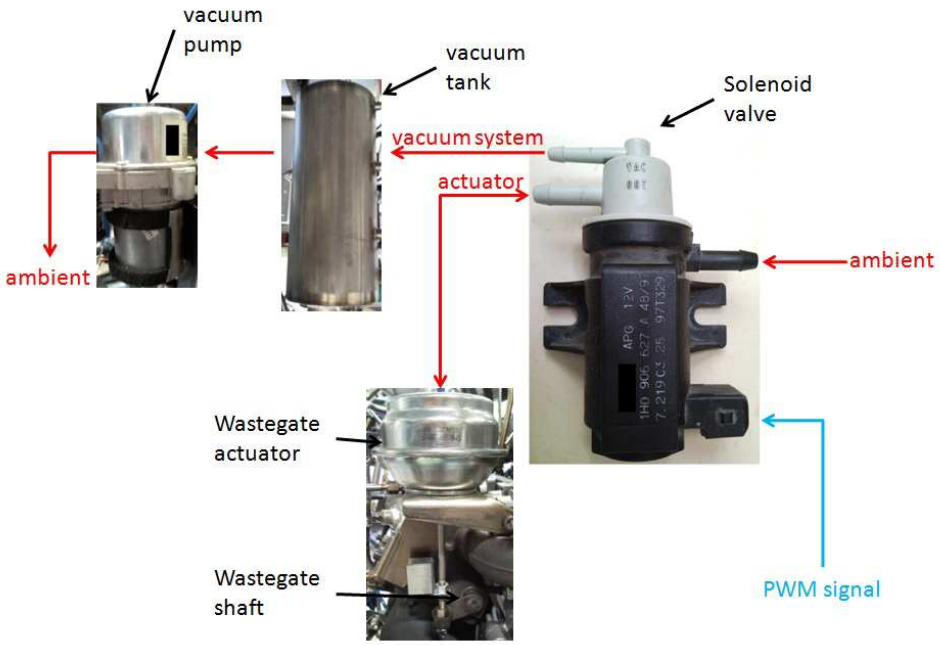

Figure 4.5 Wastegate position control system scheme: the blue line represents the electrical signal, the red lines represent the pipe connections and the direction of the mass flow. The components are not to scale

Further, the membrane is tied to a rod connected to the wastegate shaft on the turbine. The pressure in the vacuum tank should be kept low enough to allow the membrane force to overcome the actuator spring force, allowing a fully opened and closed wastegate valve.

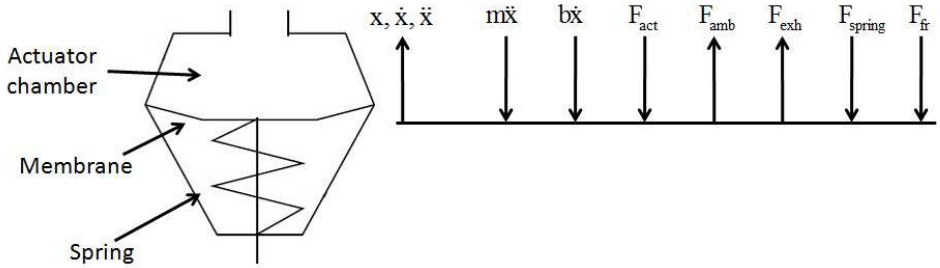

Figure 4.6 Actuator working principle and forces acting on the mechanical system

The vacuum tank pressure is controlled by the control system, that switches on the vacuum pump when the pressure becomes too high. The reasons for tank pressure rises are leakages and plunger movement in the valve. Leakages are due to air infiltration through the ducts of the system

and the elastic membrane in the solenoid valve.

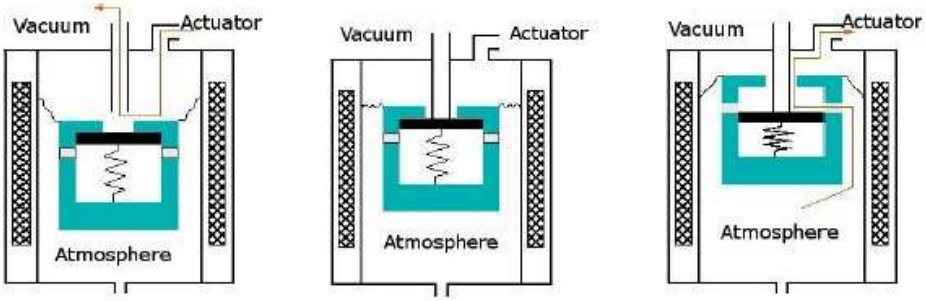

Figure 4.7 Plunger movement inside solenoid valve for the three possible working position. The plunger is drawn in blue color while the component drawn whit squared black-white at extremities of the figure is the solenoid

Further, when the plunger is in the down position, a mass flow from actuator to tank is established increasing the tank pressure, see Figure 4.7. More information on plunger behavior can be found in [46] and [78]. The importance of rejecting the supply voltage disturbances is now evident. A disturbance changes the magnetic field acting on the plunger, its position and the wastegate position, changing the boost pressure. In this work, the frequency of the PWM signal was 300 Hz, while the controller is executed at 80 Hz.

4.2.3. Experimental data

The measurements have been performed in the engine laboratory at the Division of Vehicular Systems, Linköping University. The engine uses a rapid prototyping system from dSpace (RapidPro and MicroAutoBox), connected to a PC running ControlDesk. In addition to the production tank pressure sensor, the system has been equipped with two extra sensors for modeling, a linear position sensor to measure the wastegate position and a sensor to measure the actuator chamber pressure.

4.3 Actuator modeling

The mass flow through the valve can be modeled with the orifice equations for compressible flow [46][117][104]. It should be noted that

this model is valid for steady flows with flow states and boundary geometry being sufficiently smooth functions of a spatial variable [112][102][35]. Defining the pressure ratio as eq. (4.1)

$$\Pi = \frac{p_d}{p_u} \tag{4.1}$$

where p_d and p_u are respectively the pressure downstream and upstream of the restriction and the critical pressure ratio as eq. (4.2)

$$\Pi_{crit} = \left(\frac{2}{\gamma+1} \right)^{\frac{\gamma}{\gamma-1}} \tag{4.2}$$

where γ is the specific heat ratio, the equation becomes

$$\dot{m} = \frac{p_u}{\sqrt{RT}} C_d A \Psi(\Pi) \tag{4.3}$$

Where C_d is the discharge coefficient, A is the flow area, R is the specific gas constant for air, T is the temperature upstream and $\Psi(\Pi)$ is

$$\Psi(\Pi) = \begin{cases} \Pi^{\frac{1}{\gamma}} \left\{ \frac{2\gamma}{\gamma-1} \left[1 - \Pi^{\frac{(\gamma-1)}{\gamma}} \right] \right\}^{\frac{1}{2}} & if\ \Pi \geq \Pi_{crit} \\ \gamma^{\frac{1}{2}} \left(\frac{2\gamma}{\gamma+1} \right)^{\frac{\gamma+1}{2(\gamma-1)}} & if\ \Pi < \Pi_{crit} \end{cases} \tag{4.4}$$

Eq. (4.3) can be applied to describe the leakage in the valve as well as the plunger position when it opens a passage between ambient and actuator and between actuator and tank. With knowledge about the flows to and from the components and using the ideal gas law, we get the following equation:

$$\frac{d(pV)}{dt} = \dot{m}RT \tag{4.5}$$

where the temperature variation is neglected. The tank is of constant volume and the tank pressure is calculated by integrating eq. (4.5). To

calculate the actuator pressure it is necessary to couple it to the model of the actuator, since the membrane motion causes changes in the actuator volume. The model of the actuator, and thereafter of the wastegate position, is based on Newton's second law:

$$m\ddot{x} + b\dot{x} = F_{amb} + F_{exh} - F_{act} - F_{spring} - F_{fr} \tag{4.6}$$

with the force balance as shown in Figure 4.6 and with the submodels described by eq. (4.7):

$$\begin{aligned} F_{act} &= p_{act} \cdot A_{membrane} \\ F_{amb} &= p_{amb} \cdot A_{membrane} \\ F_{spring} &= k(x) \cdot x \end{aligned} \tag{4.7}$$

where m is the system mass, b is the damping coefficient, F_{exh} is the result of the force on the wastegate plate caused by exhaust gases and F_{fr} is the friction. The most popular friction model is the Dahl's model [36] and widely used in literature [84][78][64][100]:

$$\frac{dF_{fr}}{dx} = \sigma\left(1 - \frac{F_{fr}}{F_c} \cdot sign(x \cdot)\right)^{\alpha} \tag{4.8}$$

F_c, σ and α determine the shape of the curve and need to be identified. This model is particularly suitable for hysteresis modeling.

4.3.1. Identification and validation of the model

Due to the lack of plunger position measurements, and thus the passage area across the valve, the effective area $C_d \cdot A$ has been identified as one parameter. The plunger position depends on the force equilibrium between three main elements, force due to actuator pressure, force due to ambient pressure and force due to magnetic field. This means that the actuator pressure is strongly connected to the PWM signal. In order to identify the constants of eq. (4.9) and (4.10), the least squares techniques was used on measured data.

$$C_d \cdot A = k_1 \cdot PWM^2 + k_2 \cdot PWM + k_3 \tag{4.9}$$

$$p_{act} = k_1 \cdot PWM^3 + k_2 \cdot PWM^2 + k_3 \cdot PWM + k_4 \tag{4.10}$$

The value of the parameters k_i can be found in. Table 4.1

Table 4.1 Regression coefficients

	$C_d \cdot A$	p_{act}
k_1	$-4.7625 \cdot 10^{-5}$	$2.8939 \cdot 10^{-2}$
k_2	$7.2000 \cdot 10^{-2}$	-6.5767
k_3	$-5.2300 \cdot 10^{-2}$	$4.4044 \cdot 10^{2}$
k_4		$1.0612 \cdot 10^{5}$

The identified effective area for the passage from ambient to actuator is $8 \cdot 10^{-9}\, m^2$, and the passage area between actuator and tank is $10 \cdot 10^{-7}\, m^2$. Figure 4.8 shows a comparison between model and measurement, where the model is shown to give good agreement. Eq. (4.11) manages the mass flow through the volumes of the system.

$$\dot{m} = \begin{cases} \frac{p_u}{\sqrt{RT}} \cdot C_d \cdot A \cdot \Psi(\Pi) & if\ p_u > p_{PWM} \\ 0 & if\ p_u = p_{PWM} \end{cases} \tag{4.11}$$

where p_{PWM} is the pressure achievable depending the value of the PWM signal.

An analysis of experimental data shows that some approximations in the model can be assumed. In Figure 4.9 a slow up-down ramp was performed to analyze actuator hysteresis effects, and the result was that this effect can be neglected.

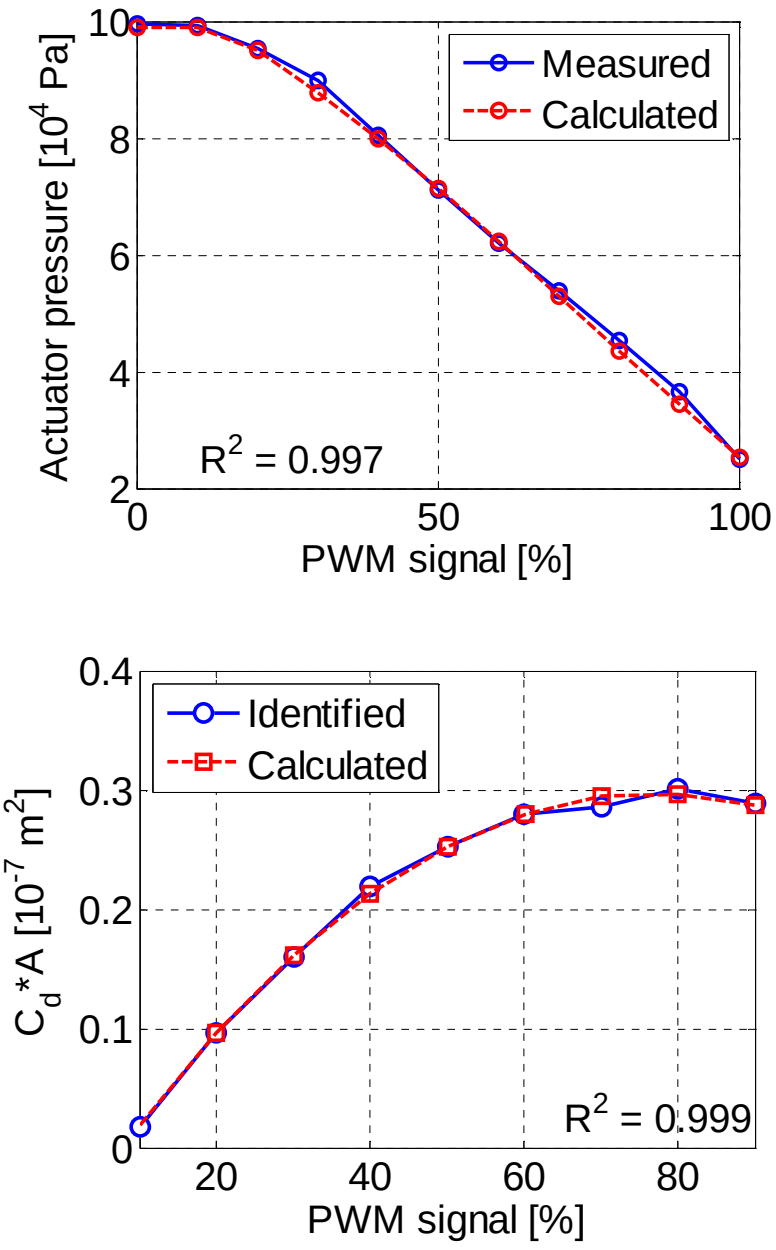

Figure 4.8 Influence of PWM signal on leakage discharge coefficient (upper) and actuator pressure (lower)

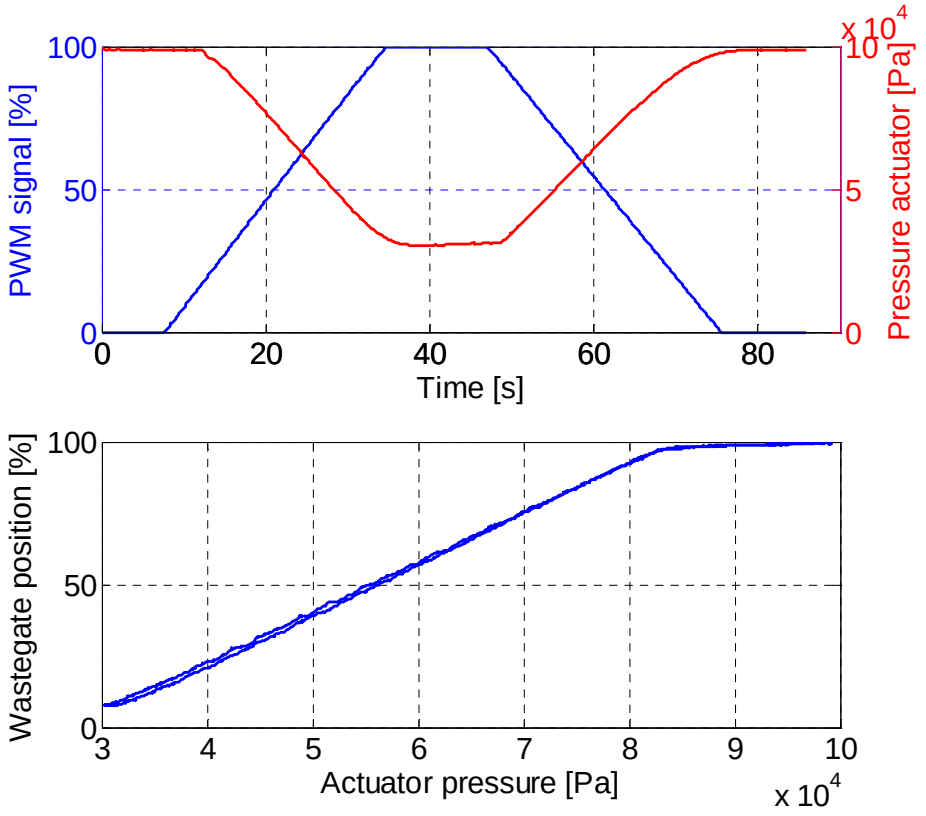

Figure 4.9 Identification of hysteresis phenomenon with a up-down slow ramp in PWM signal

The exhaust gases force is also neglected, because it has a negligible effect on the wastegate position, Figure 4.10. The step in the actuator position between 72.5 s and 82.2 s is due to the switching on of the vacuum pump that produces a supply voltage drop and shows again the phenomenon of the wastegate position changing connected to the supply voltage level.

An analysis of the actuator spring and the vacuum pump is then needed, to complete the model. Figure 4.11 shows that the spring has a nonlinear behavior. The lowest possible actuator pressure is the tank pressure, see lower plot of Figure 4.12, and if the tank pressure is too high, the wastegate valve cannot be fully actuated. To avoid this, the pressure in the tank is kept between 30 and 35 kPa by the control system. In this region the mass flow from tank to ambient when the pump is

switched on can be considered constant.

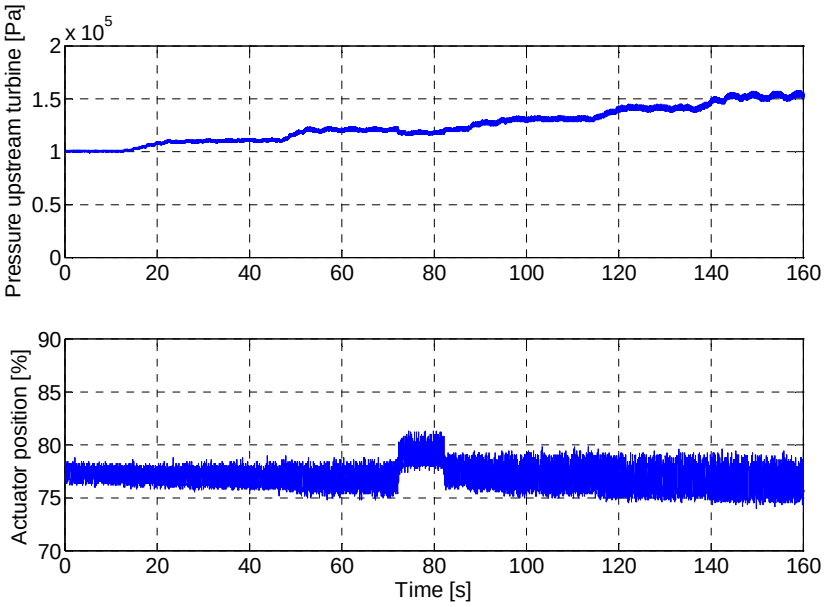

Figure 4.10 Influence of force of the exhaust gases with constant PWM signal

A comparison between model and measurements is shown in Figure 4.12, for a ramp and a step in the PWM signal. Further, the dynamic behavior of the actuator and tank pressure, and actuator position are satisfactorily reproduced by the model.

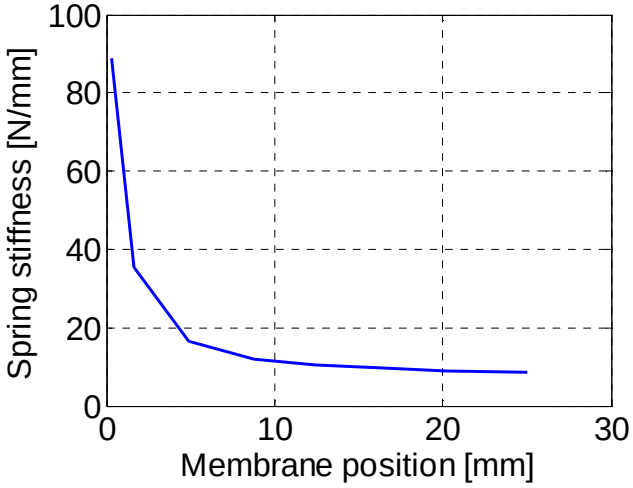

Figure 4.11 Spring stiffness

4.4 Compensator development

The system voltage is expected to affect the magnetic field controlling the plunger position. Further, the plunger movement is expected to be slow compared to fast changes in the magnetic field and the plunger is therefore assumed to follow a moving average of the magnetic field. Based on experimental data the following simple compensator is proposed to handle deviations in supply voltage:

$$PWM_{comp} = \frac{12}{U} \cdot PWM_{12V} \tag{4.12}$$

where PWM_{comp} is the compensated PWM, U is the supply voltage, and PWM_{12} is the PWM value if the voltage is 12 V.

Given a desired value of wastegate position, a corresponding PWM value can be calculated using the inverse of the actuator model. A compensation for supply voltage is then calculated using eq. (4.12). The compensator was tested with a voltage disturbance and the results are shown in Figure 4.13 taking care to repeat the same shape of the voltage disturbance. Despite the voltage disturbance, appropriately modulating the PWM value with the compensator, membrane position is kept constant, verifying the performance of the compensator. The compensated wastegate position is unaffected by the supply voltage disturbance.

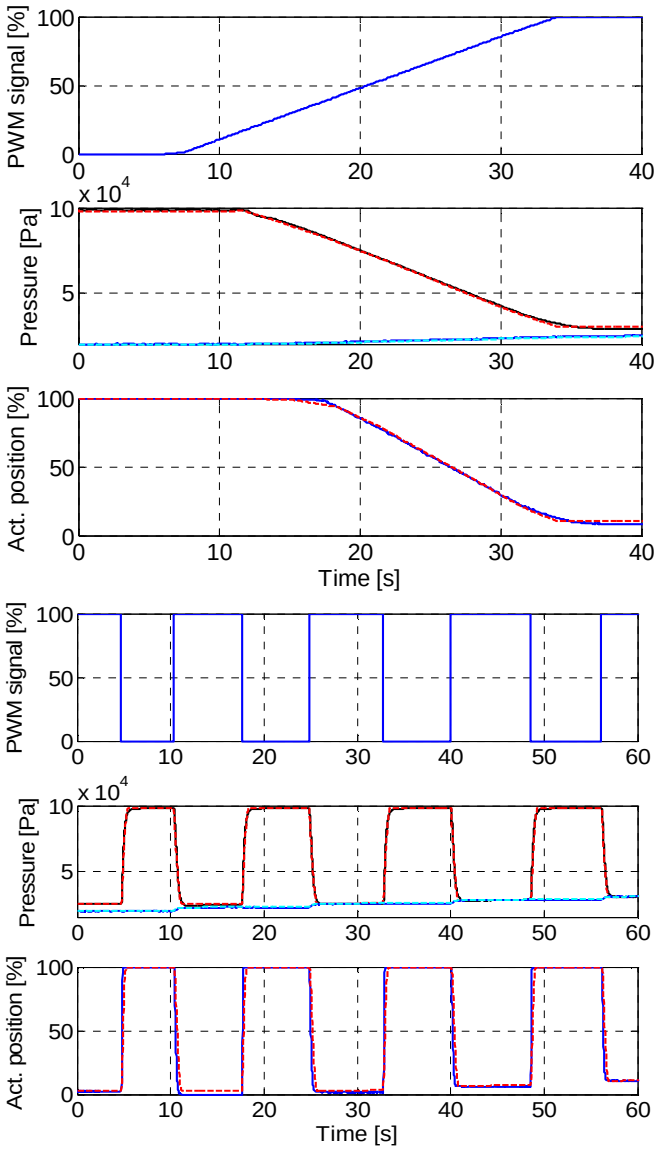

Figure 4.12 Validation of the model. The pressure lines represent: measured actuator pressure (black solid), model actuator pressure (red dashed), measured tank pressure (blue solid) and model tank pressure (light blue dashed). In the actuator position plot, the measured position is in blue solid and the calculated position is in red dashed

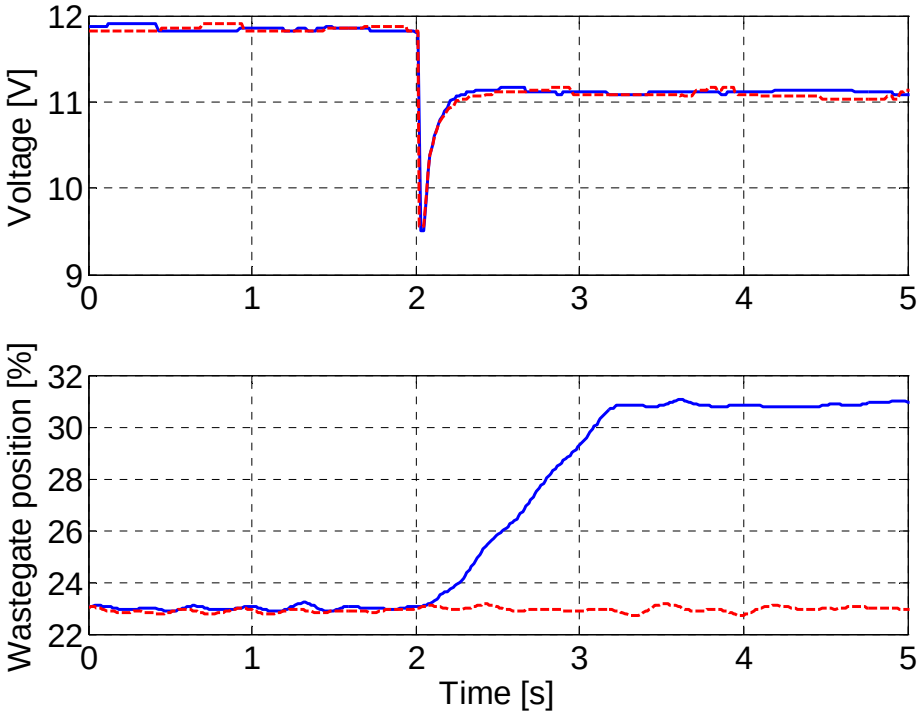

Figure 4.13 Compensator performance for the supply voltage disturbance. The second plot shows the wastegate position without compensator (solid) and with compensator (dashed)

4.5 Boost pressure controller

Before developing the control system, an analysis to find the best turbocharger configuration was carried out using the TSTCSI MVEM [41][40]. Focus was on low engine speed. The maximum boost pressure was set up to 240 kPa to avoid engine damage and in-cylinder knocking. Two configurations, both with the throttle fully opened, were investigated: LP-wastegate fully closed and fully opened. The HP-wastegate was used to maintain constant boost pressure.

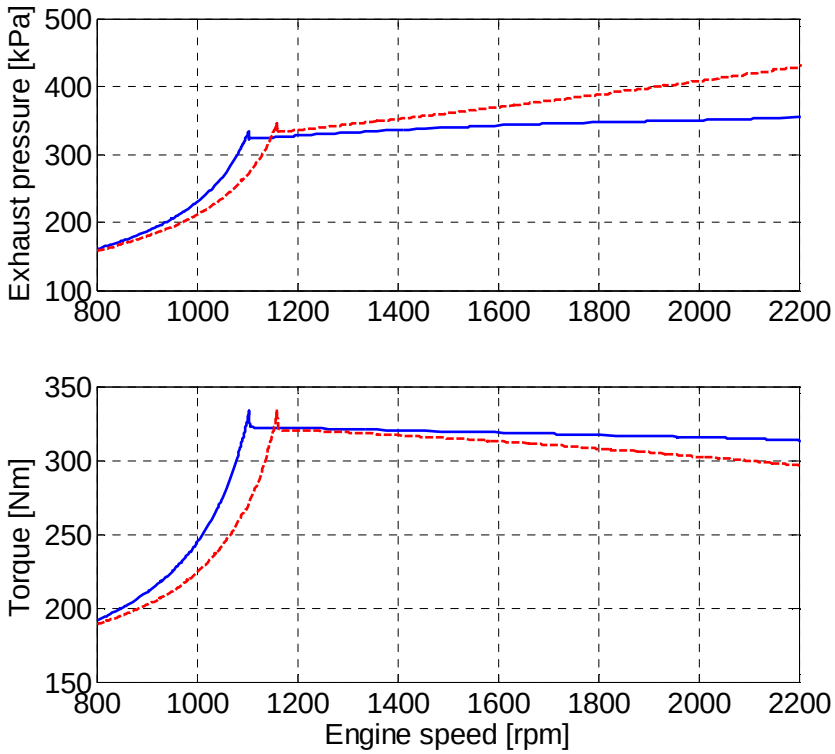

Figure 4.14 Comparison between two different control strategies for low engine speed. HP-wastegate is controlled keeping respectively LP-wastegate fully closed (solid) and fully opened (dashed)

Figure 4.14 shows that running with LP-wastegate fully closed gives maximum torque at lower engine speed. The LP-wastegate fully closed configuration is therefore used up to 2000 rpm, where the torque begins to decrease and the back pressure reaches too high values. The structure of the control system is shown in Figure 4.15, where the feedforward is a static map for PWM depending on desired boost pressure and engine speed [109].

To overcome the nonlinearities of the system, it was linearized across different desired boost pressures and engine speeds. Control signal step responses are then used to identify the parameters of the transfer function, which was modeled as a first order system with time delay model:

$$G(s) = \frac{K_p}{1+T_{tf}s} \cdot e^{-Ls} \tag{4.13}$$

where K_p is the static gain of the system, T_{tf} is the time constant and L is the time delay.

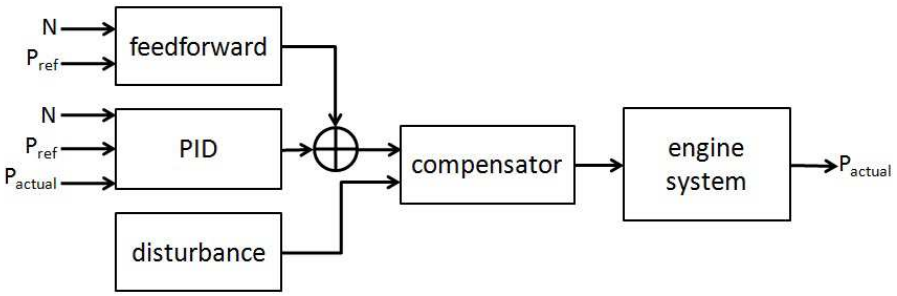

Figure 4.15 Control system structure

The most common version of a transfer function for a PID controller is shown in eq. (4.14)

$$C(s) = K \cdot \left(1 + \frac{1}{s T_i}\right) \cdot (1 + s T_d) \tag{4.14}$$

Where K is the proportional gain, T_i is the integral time and T_d is the derivative time. The design method chosen in this work is the λ-tuning that, for non-interacting PID controllers, provides:

$$\begin{aligned} K &= \frac{1}{K_p} \frac{L/2 + T_{tf}}{L/2 + \lambda} \\ T_i &= T_{tf} + \frac{L}{2} \\ T_d &= \frac{T_{tf} L}{L + 2T_{tf}} \end{aligned} \tag{4.15}$$

where λ is the time constant describing how fast the controller will react to a control error.

The derivative terms deserves a special investigation. In on-board applications instabilities could occur if the signal error, usually defined as the difference between reference and actual value ($e = p_{ref} - p_{act}$) processed by the derivative part is unfiltered due to high-frequency measurements noise. For this reason the signal have been filtered. This

creates problems in the filtered derivative part when the reference value changes quickly. In order to avoid it, for this part only, the signal used is the process variable p_{act} [108][109]. A tracking mode was added to the controller, with tracking time $T_{tr} = \sqrt{T_i T_d}$, to remove the wind-up phenomenon when the control variable saturates [15].

The above procedure was applied for each point of the linearization grid to achieve a gain scheduled feedback loop. A relay type controller was used to maintain the tank pressure between 30 kPa and 35 kPa, where the controller is switched on if the pressure is higher than 35 kPa and switched of when the tank pressure becomes lower than 30 kPa.

4.6 Experimental testing

The performance of the boost pressure control system was tested on both the MVEM model and the engine test stand. Obviously the experimental results are more interesting that the model results so that the experimental results from the test stand will be presented. Once having validated the performances of the voltage compensator, the performance investigation has been divided into two steps:

1. the developed boost pressure controller;
2. the coupling of the voltage compensator with the boost pressure controller.

Figure 4.16 shows the resulting boost pressure for several steps up and down with a constant system voltage. Boost pressure follows the steps in reference value correctly. A small undershoot is present for a positive reference step, but it is limited to 5 kPa. The behavior is better for a reference pressure decrease, and the largest overshoot is only 1 kPa. The saturation of the PWM signal guarantees a fast response. It is worth mentioning that the controller parameters have been tuned using only the model and no retuning is made on the engine test bench.

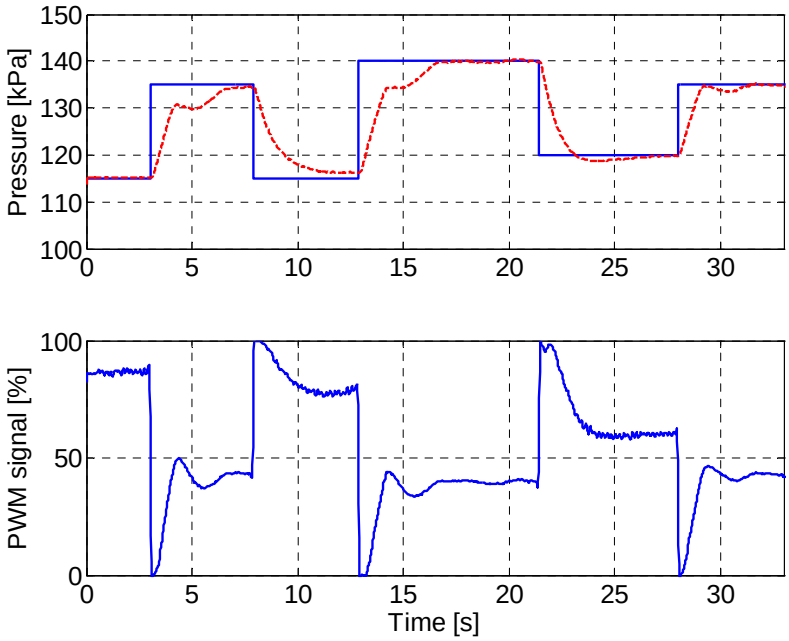

Figure 4.16 Performance of the control system at 1500 rpm subject to steps in reference value with a constant supply voltage. Upper plot: reference (solid) and actual pressure (dashed) are drawn. Lower: Corresponding PWM signal

The voltage compensator is then integrated in the engine control system. The experimental results, shown in Figure 4.17, point out that the simple compensator proposed is effective and the maximum pressure error is 1 kPa (0.8%). Since the boost pressure does not change much for variations in system voltage, this means that the wastegate position is almost constant and there is only a small movement in the membrane, proving the disturbance rejection.

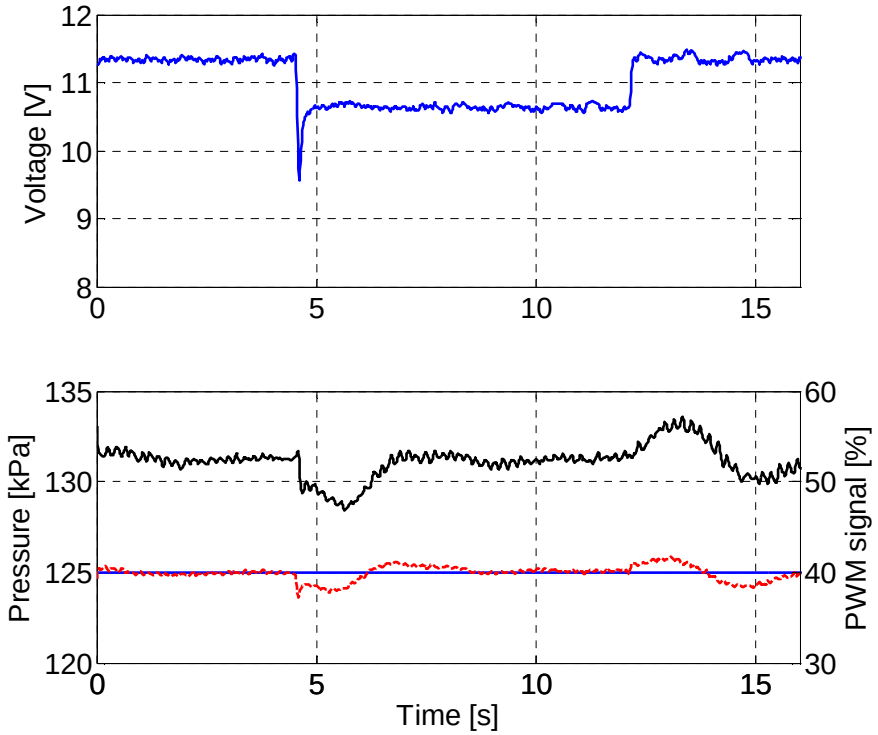

Figure 4.17 Performance of the control system with the developed compensator at 1500 rpm and a pressure set-point of 125 kPa. Upper plot: System voltage. Lower plot: PWM signal (black solid), desired (blue solid) and current (red dashed) boost pressure

CHAPTER 5

Conclusions

In the dissertation, the value of engine system modeling has been discussed. It was shown how modeling in-cylinder processes and turbocharger can aid the development of the control strategies saving time and money efforts. All the developed models were experimentally validated and applied for optimization analysis or real-time control.

Particularly the model based optimization of the engine control variables of an automotive turbocharged Diesel engine has been presented. The model structure is based on a hybrid approach, with a predictive multi-zone model for the simulation of in-cylinder processes (i.e. combustion and emissions formation) integrated with a control-oriented turbocharger model to predict intake/exhaust processes. Model accuracy was tested via comparison between measured and simulated in-cylinder pressure and engine exhaust temperature on a wide set of experimental data, measured at the test bench. Validation results exhibit a correlation index R^2 equal to 0.995 and 0.996 for IMEP and exhaust temperature, respectively. The optimization analysis was aimed at minimizing NO emissions in four steady state engine operating conditions, selected among those of interest for the ECE/EUDC test driving cycle. Constraints were introduced to prevent from increase of soot emissions and low exhaust temperature which would have a negative impact on the efficiency of the after-treatment devices. The optimization results evidence a significant reduction of engine NO emissions by means of increased EGR rate and earlier main fuel injection.

A model-based optimization was also applied for a CNG heavy-duty engine, equipped with turbocharger and EGR. The optimization analysis was addressed to design the set-points of engine control variables, following the implementation of an EGR system aimed at reducing the in-cylinder temperature and preventing from the thermal stress of engine components (i.e. head and valves). A co-simulation analysis was carried out by coupling a 1-D engine commercial code with a classical constrained optimization algorithm. The 1-D model accounts for intake

and exhaust gas flow arrangement, comprehensive of EGR system and turbocharger, while an empirical formulation based on the classical Wiebe function was implemented to simulate the combustion process. An intensive identification analysis was performed to correlate Wiebe model parameters to engine operation and guarantee model accuracy and generalization even in case of high EGR rate. 1-D model and identification results were successfully validated against a wide set of experimental data, measured on the test bench. The results of the optimization analysis, aimed at minimizing fuel consumption while preventing from thermal stress, showed an increase of fuel economy up to 4.5% and a reduction of the thermal load below the imposed threshold, against five engine operating conditions selected among the most critical of the reference European Transient Cycle (ETC). Particularly, the effectiveness of the co-simulation analysis is evidenced in pursuing the conflicting goal of optimizing engine control while reducing the recourse to time consuming and expensive experiments at the test bed. This latter point is becoming more and more critical as the number of control variables is increasing with engine complexity.

Both the presented optimization analyses evidenced the key-role of the turbocharger to face with energy and emissions issues. Particularly the impact of the turbocharger management via wastegate or VGT control was evidenced. Indeed, by acting on these components, the amount of exhaust gases evolving in the turbine can be managed thus regulating the supercharging degree and the boost pressure. This allows keeping the throttle valve fully open with significant decrease of pumping losses. The wastegate position is defined by a pneumatic actuator in which the pressure is regulated by a solenoid valve fed by a PWM signal. The drawback of this system is the dependence of the PWN signal, and afterwards of the performance, from the system supply voltage. During the thesis the development of a wastegate actuator model was carried out in order to compensate the actuator PWM signal to improve boost pressure control. The compressible flow equations were found to be sufficient to describe the actuator system mass flow and both discharge coefficient and static actuator chamber pressure were modeled using polynomials in PWM signal. Furthermore a simple friction model was implemented to simulate the actuator system. The boost pressure controller based on the developed compensator has shown to give limited undershoot and overshoot and is further able to reject the disturbance in

supply voltage. The compensator was incorporated into a boost pressure controller and the complete control system has shown to reject system voltage variations and perform good boost pressure control in both simulations analyses and experimental tests on the engine test stand. Model simulations evidenced the need to ensure low enough vacuum pressure to enable fully closed and open actuator while a switch type controller was proved to be sufficient for vacuum tank pressure control.

Acknowledgements

I wish to address my special thanks to Prof. Ivan Arsie and Prof. Cesare Pianese: with their constant and essential support during this three years, they have represented the “landmark” around which all of my work has been developed.

A thanks goes to Prof. Lars Eriksson who gave me the opportunity to have a great experience at the Institute of Technology in Linköping, being my Swedish supervisor. Moreover I would like to thank the whole staff of the Vehicular Systems Laboratory of the University of Linköping, especially Oskar Leufvén, Andreas Thomasson, Kristoffer Lundahl and Per Öberg for their uninterrupted assistance in Sweden.

The final thanks go to my “roommates” (staff and Ph.D. students) in the Laboratory I5 of the Department of Industrial Engineering at University of Salerno, particularly to Gianpaolo Noschese for his valuable technical support.

References

[1] Andersen J., Lindström F., Westin F., (2008) - Surge definitions for radial compressors in automotive turbochargers, SAE International Journal of Engines, 1(1):218.

[2] Andersson P., (2005) - Air charge estimation in turbocharged spark ignition engines, PhD thesis 989, Department of Electrical Engineering, Linköpings Universitet, Linköping, Sweden.

[3] Arsie I., Criscuolo I., De Cesare M., Pianese C., (2011) - Tuning of the engine control variables of an automotive turbocharged diesel engine via model based optimization, SAE Technical Paper 2011-24-0146, DOI: 10.4271/2011-24-0146.

[4] Arsie I., Criscuolo I., De Simio L., Iannaccone S., (2010) - Ottimizzazione delle leggi di controllo di un motore heavy-duty alimentato a gas naturale, Atti del 65° Congresso Nazionale ATI – Domus de Maria (CA), September 13-17 2010.

[5] Arsie I., Criscuolo I., De Simio L., Iannaccone S., (2011) - Optimization of control parameters for a heavy-duty cng engine via co-simulation analysis, SAE Technical Paper 2011-01-0704, DOI: 10.4271/2011-01-0704.

[6] Arsie I., Di Genova F., Mogavero A., Pianese C., Rizzo G., Caraceni A., Cioffi P., Flauti G., (2006) - Multi-zone predictive modeling of common-rail multi-injection diesel engines, SAE Technical Paper 2006-01-1384.

[7] Arsie I., Di Genova F., Pianese C., Rizzo G., Caraceni A., Cioffi P., Flauti G., (2005) - Thermodynamic modeling of jet formation and combustion in common rail multi-jet diesel engines, SAE Technical Paper 2005-01-1121.

[8] Arsie I., Di Genova F., Pianese C., Sorrentino M., Rizzo G., Caraceni A., Cioffi P., Flauti G., (2004) - Development and identification of phenomenological models for combustion and emissions of common-rail multi-jet diesel engines, SAE Technical Paper 2004-01-1877.

[9] Arsie I., Flora R., Pianese C., Rizzo G., Serra G., (2000) - A

computer code for s.i. engine control and powertrain simulation, SAE Technical Paper 2000-01-0938.

[10] Arsie I., Pianese C., Rizzo G., (1998) - Models for the prediction of performance and emissions in a spark ignition engine, - a sequentially structured approach, SAE Technical Paper 980779.

[11] Arsie I., Pianese C., Rizzo G., (2003) - An integrated system of models for performance and emissions in si engines: development and identification, SAE Technical Paper 2003-01-0993.

[12] Arsie I., Pianese C., Sorrentino M., (2007) - Effects of control parameters on performance and emissions of hsdi diesel engines: investigation via two zone modelling, Oil & Gas Science and Technology - Revue de l'IFP, Vol. 62, No. 4, pp. 457-469.

[13] ASME PTC 10-1997, (1997) - Performance test code on compressors and exhausters, American Society of Mechanical Engineers, New York.

[14] Assanis N. D. e Heywood J. B., (1986) – Development and use of a computer simulation of the turbocompounded Diesel system for engine performance and component heat transfer studies, SAE Technical Paper 860329.

[15] Åström, K.J. and Hägglund, T., (2005) - Advanced PID control, ISA - The Instrumentation, Systems, and Automation Society

[16] Ayoub N. S. and Reitz R., (1995) - Multidimensional computation of multicomponent spray vaporization and combustion, SAE Technical Paper 950285.

[17] Barba C., Burkhardt C., Boulouchos K., Bargende M., (2000) – A phenomenological combustion model for heat release rate prediction in high-speed di diesel engines whit common rail injection, SAE Technical Paper 2000-01-2933.

[18] Bayer J. e Foster D. E., (2003) - Zero-dimensional soot modeling, SAE Technical Paper 2003-01-1070.

[19] Bella G., Rocco V., Ubertini S., (2002) - Combustion and spray simulation of a di diesel engine models, SAE Technical Paper 2002-01-2776.

[20] Belytschko T., Lu Y. Y., Gu L., (1994) - Element-free Galerkin methods, International journal for numerical methods in engineering, Vol. 37,229-256.

[21] Benson R.S., (1982) - The thermodynamics and gas dynamics of internal combustion engines, Vol. 1, Edited by Horlock J.H. and Winterbone D.E., Clarendon Press, Oxford.

[22] Bergström J., Leufvén O., (2007) - Surge modeling and control of automotive turbochargers, Master's thesis LiTH-ISY-EX-3999, Department of Electrical Engineering, Linköpings Universitet, Linköping, Sweden.

[23] Bhaskar T. e Mehta P. S., (1998) - Effect of swirl and fuel injection characteristics on premixed phase of diesel combustion, SAE Technical Paper 980534.

[24] Bi X, Yang M., Han S. and Ma Z., (1999) - A Multi-Zone Model for Diesel Spray Combustion, SAE Technical Paper 1999-01-0916.

[25] Bianchi G. M., Falfari S., Pelloni P., Kong S. C., Reitz R. D., (2002) - Numerical analysis of high-pressure fast-response common rail injector dynamics, SAE Technical Paper 2002-01-0213

[26] Bozza F., Gimelli A., Senatore A., Caraceni A., (2001) - A theoretical comparison of various vva systems for performance and emission improvements of si engine,. SAE Technical Paper 2001-01-0670.

[27] Canova M., Fiorani P., Gambarotta A., Tonetti M., (2005) - A real-time model of a small turbocharged multijet diesel engine: application and validation, SAE Technical Paper 2005-24-065.

[28] Canova M., Midlam-Mohler S., Guezzennec Y. and Rizzoni G., (2009) - Mean Value Modeling and Analysis of HCCI Diesel Engines With External Mixture Formation, ASME Journal of Dynamic Systems, Measurement, and Control, Vol. 131, No. 11.

[29] Casey M.V, Schlegel M., (2010) - Estimation of the performance of turbocharger compressors at extremely low pressure ratios, Proceedings of the Institution of Mechanical Engineers, Part A: Journal of Power and Energy, 224(2):218.

[30] Catalano L. A., Tondolo V. A., Dadone A., (2002) - Dynamic rise of pressure in the common-rail fuel injection system, SAE Technical Paper 2002-01-0210.

[31] Chapman K. S., Shultz J., (2003) - Guidelines for: testing large-

bore engine turbochargers, Technical report, The National Gas Machinery Laboratory, Kansas State University, 245 Levee Drive.

[32] Coppo M., Dongiovanni C., (2007) - Experimental validation of a common-rail injector model in the whole operation field, J. Eng. Gas Turbines Power, Volume 129, Issue 2 DOI: 10.1115/1.2432889

[33] Corcione F.E., Fusco A., Valentino G., Papetti F., (1993) - Numerical and Experimental Analysis of Diesel Air Fuel Mixing, SAE Paper 931948.

[34] Criscuolo I., Leufvén O., Thomasson A., Eriksson L., (2011) - Model-based boost pressure control with system voltage disturbance rejection, Proc. of the 18th IFAC World Congress, August 28 – September 2 2011, Milano, ISBN 9783902661937, DOI: 10.3182/20110828-6-IT-1002.02214.

[35] Cunningham, R., (1951) - Orifice meters with supercritical compressible flow, trans. of the ASME, 73, 625-638.

[36] Dahl, P., (1968) - A solid friction model. Technical Report TOR-0158H3107-18I-1. The Aerospace Corporation.

[37] De Simio L., Gambino M., Iannaccone S., (2009) - A study of different egr routes on a heavy-duty stoichiometric natural gas engine, SAE Technical Paper 2009-24-0096.

[38] Dixon S.L., (1998) - Fluid mechanics and thermodynamics of turbomachinery, Butterworth-Heinemann, fourth edition.

[39] Emmenthal, K., Hagermann, G., Hucho, W., (1979) - Turbocharging small displacement spark ignited engines for improved fuel economy. SAE Technical Paper 790311.

[40] Eriksson L., (2010) - Modeling of turbocharged engines with mvem_lib, University of Linköping.

[41] Eriksson, L., (2007) - Modeling and control of turbocharged si and di engines, Oil & Gas Science and Technology Rev. IFP, 62(4), 523-538.

[42] Eriksson, L., Frei, S., Onder, C., Guzzella, L., (2002) - Control and optimization of turbo charged spark ignited engines, IFAC World Congress.

[43] Eriksson, L., Nielsen, L., (2000) - Non-linear model-based throttle control, SAE Technical Paper 2000-01-0261.

[44] Erlandsson O., (2002) - Thermodynamic Simulation of HCCI Engine Systems, PhD thesis 989, Department of Heat and Power Engineering, Lund Institute of Technology.

[45] Ferguson C.R., (1986) - Internal Combustion Engine, Applied Thermosciences, John Wiley.

[46] Galindo J., Climent H., Guardiola C., Domenech J., (2009) - Modeling the vacuum circuit of a pneumatic valve system, Journal of Dynamic Systems, Measurement, and Control, 131(031011).

[47] Galindo J., Serrano J. R., Guardiola C., Cervelló C., (2006) - Surge limit definition in a specific test bench for the characterization of automotive turbochargers, experimental Thermal and Fluid Science, 30(5):449 - 462.

[48] Galindo J., Serrano J.R., Climent H., Tiseira A., (2008) - Experiments and modelling of surge in small centrifugal compressor for automotive engines, Experimental Thermal and Fluid Science, 32(3):818 – 826.

[49] Galindo J., Serrano J.R., Margot X., Tiseira A., Schorn N., Kindl H., (2007) - Potential of flow pre-whirl at the compressor inlet of automotive engine turbochargers to enlarge surge margin and overcome packaging limitations, International Journal of Heat and Fluid Flow, 28(3):374 - 387.

[50] Gambino M., Corbo P., Iannaccone S., Unich A., (1995) - Comparison between lean-burn and stoichiometric technologies for cng heavy-duty engines, SAE Technical Paper 950057.

[51] Gill P.H., Murray W., Wright M.H., (1984) - Practical optimization, Academic Press, London.

[52] Gravdahl J.T., Egeland O., (1997) - Speed and surge control for a low order centrifugal compressor model, Control Applications, Proceedings of the 1997 IEEE International Conference on, pages 344 –349, 5-7.

[53] Gravdahl J.T., Egeland O., (1999) - Centrifugal compressor surge and speed control, Control Systems Technology, IEEE Transactions on, 7(5):567 - 579.

[54] Gravdahl J.T., Egeland O., Vatland S.O., (2001) - Active surge control of centrifugal compressors using drive torque, proceedings of the 40th IEEE Conference.

[55] Gravdahl J.T., Willems F., de Jager B., Egeland O., (2000) - Modeling for surge control of centrifugal compressors: comparison with experiment, proceedings of the 39th IEEE Conference on, volume 2, pages 1341 –1346 vol.2.

[56] Greitzer E. M., (1981) - The stability of pumping systems, ASME Transactions Journal of Fluids Engineering, 103:193–242.

[57] Gu F., Engeda A., Cave M., Di Liberti J., (2001) - A numerical investigation on the volute/diffuser interaction due to the axial distortion at the impeller exit, Journal of Fluids Engineering, 123(3):475–483.

[58] Guzzella L., Wenger U., Martin R., (2000) - IC-engine downsizing and pressure-wave supercharging for fuel economy, SAE Technical Paper 2000-01-1019.

[59] Hansen K. E., Jorgensen P., Larsen P. S., (1981) - Experimental and theoretical study of surge in a small centrifugal compressor, ASME Journal Fluids Engineering, (103):391 - 395.

[60] Hellström F., (2010) - Numerical computations of the unsteady flow in turbochargers, PhD thesis, KTH, Fluid Physics.

[61] Hendricks E., Sorenson S.C., (1991) - SI engine controls and mean value engine modeling, SAE Technical Paper 910258.

[62] Heywood J. B. (1988) - Internal Combustion Engine Fundamentals, McGraw-Hill.

[63] Hiroyasu H. e Kadota T., (1983) - Development and use of a spray combustion modeling to predict diesel engine efficiency and pollutant emission, Bulletin of the ASME, Vol. 26, No 214.

[64] Hlouvry, B., Dupont, P., (1994) - A survey of models, analysis tools and compensation methods for the control of machines with friction, Automatica, 30(7), 1083-1138.

[65] Jensen J.-P., Kristensen A. F., Sorenson S.C., Houbak N., Hendricks E., (1991) - Mean value modeling of a small turbocharged diesel engine, SAE Technical Paper 910070.

[66] Jiang W., Khan J., Dougal R. A., (2006) - Dynamic centrifugal compressor model for system simulation, Journal of Power Sources, 158(2):1333 - 1343.

[67] Jung D. e Assanis D.N., (2001) - Multi-zone di Diesel spray combustion model for cycle simulation studies of engine

performance and emissions, SAE Technical Paper 2001-01-1246.

[68] Kamimoto T., Kobayashi H. e Matsuoka S., (1981) - A big size rapid compression machine for fundamental studies of diesel combustion, SAE Technical Paper 811004.

[69] Kong S. C., Han Z., Reitz R. D., (1995) - The development and application of a diesel ignition and combustion model for multidimensional engine simulation, SAE Technical Paper 950278.

[70] Kouremenos D. A., Rakopoulos C. D. e Hountalas D.T., (1997) - Multi-zone combustion modelling for the prediction of pollutants emissions and performance of DI Diesel engines, SAE Technical Paper 970635.

[71] Leufvén O., (2010) - Compressor Modeling for Control of Automotive Two Stage Turbochargers, Licentiate thesis, Linköping University, LiU-TEK-LIC-2010:32, Thesis No. 1463.

[72] Leufvén O., Eriksson L., (2008) - Time to surge concept and surge control for acceleration performance, Proc. of the 17th IFAC World Congress, DOI: 10.3182/20080706-5-KR-1001.00350.

[73] Leufvén O., Eriksson L., (2010) – Engine test bench turbo mapping, SAE Technical Paper 2010-01-1232.

[74] Leufvén O., Eriksson L., (2011) - Surge and choke capable compressor model. Proc. of the 18th IFAC World Congress, DOI:10.3182/20110828-6-IT-1002.00694.

[75] Leufvén O., Eriksson L., (in press) - Investigation of compressor correction quantities for automotive applications, International Journal of Engine Research.

[76] Lewis R. I., (1996) - Turbomachinery performance analysis, Arnold.

[77] Lipkea W. H. e DeJoode A. D., (1987) - A model of a direct injection Diesel combustion system for use in cycle simulation and optimization studies, SAE Technical Paper 870573.

[78] Mehemood A., Laghrouche S., El Bagdouri M., (2010) - Nonlinear modeling of the VNT pneumatic actuator with aero-dynamic force, 6th IFAC Symposium Advances in Automotive Control.

[79] Moraal P., Kolmanovsky I., (1999) - Turbocharger modeling for

automotive control applications, SAE Technical Paper 1999-01-0908.

[80] Mueller M., Hendricks E., Sorenson S., (1998) - Mean value modeling of turbocharged spark ignition engines, SAE Technical Paper 980784.

[81] Müller M., Sumser S., Fledersbacher P., Rößler K., Fieweger K., Bauer H. J., (2005) - Using the centrifugal compressor as a cold-air turbine, 8th international conference on turbochargers and turbocharging, Imperial College London.

[82] Naber J. D., Siebers D. L., (1996) - Effects of gas density and vaporization on penetration and dispersion of diesel spray, SAE Technical Paper 960034.

[83] Nellen C., Boulouch K., (2000) - Natural gas engines for cogeneration: highest efficiency and near-zero emissions through turbocharging, EGR and 3-way catalytic converter, SAE Technical Paper 2000-012825.

[84] Olsson H., Åström, K., (1998) - Friction models and friction compensation, European J. of control.

[85] Onorati A., Ferrari G., D'Errico G. (1999) - Fluid dynamic modeling of the gas flow with chemical specie transport through the exhaust manifold of a four cylinders SI engine. SAE Technical Paper 1999-01-0557.

[86] Park J. K., Shenghua L., Hwang J. W., Kim M. H., Chae J. O., (1999) - Multizone model for DI Diesel engine combustion and emissions, SAE Technical Paper 1999-01-2926.

[87] Patankar S.V., (1980) - Numerical heat transfer and fluid flow, Hemisphere, Waschington D.C.

[88] Patterson M. A., Kong S. C., Hampson G. J., Reitz R. D., (1994) - Modeling the effects of fuel injection characteristics on diesel engine soot and NO_X emissions, SAE Technical Paper 940523.

[89] Petitjean D., Bernardini L., Middlemass C., Shahed S., Hurley R., (2004) - Advanced gasoline engine turbocharging technology for fuel economy improvements, SAE Technical Paper 2004-01-0988.

[90] Qiu X., Japikse D., Zhao J., Anderson M. R., (2012) - Analysis and validation of a unified slip factor model for impellers at design and offdesign conditions, proceedings of ASME Turbo Expo,

Glasgow, UK.

[91] Rakopoulos C. D., Rakopoulos D. C., Kyritsis D. C., (2003) - Development and validation of a comprehensive two-zone model for combustion and emissions formation in a DI Diesel engine, International Journal of Energy Research, Vol. 27 pp 1221-1249.

[92] Ramos J. I., (1989) - Internal combustion engine modeling, Hemisphere Publishing Corporation.

[93] Ratkowsky D.A., (1983) - Nonlinear Regression Modeling, Dekker, New York.

[94] Rutland C. J., Eckhause J., Hampson G., Hessel R., Kong S. C., Patterson M., Pierpont D., Sweetland P., Tow T., Reitz R. D., (1994) - Toward predictive modeling of Diesel engine intake flow, combustion and emissions, SAE Technical Paper 94197.

[95] SAE J1826, (1995) - Turbocharger gas stand test code, SAE standard.

[96] SAE J922, (1995) - Turbocharger nomenclature and terminology. SAE standard.

[97] Sato T., Oh J. M., Engeda A., (2005) - Experimental and numerical investigation of the flow in a vaneless diffuser of a centrifugal compressor stage. part 1: Experimental investigation, Proc. of the IMechE, Part C: J. of Mech. Eng. Science, 219(10).

[98] Shrivastava R., Hessel R., Reitz R. D., (2002) - CFD optimization of DI Diesel engine performance and emissions using variable intake valve actuation with boost pressure, EGR and multiple injections, SAE Technical Paper 2002-01-0959.

[99] Silvestri J., Morel T., (1994) - Study of intake system wave dynamics and acoustics by simulation and experiment. SAE Technical Paper 940206.

[100] Singh R., Kunt C., (1990) - A linear time varying model for on-off valve controlled pneumatic actuators, Trans. of the ASME.

[101] Sokolov A. A., Glad S. T., (1999) - Identifiability of turbocharged IC engine models, SAE Technical Paper 1999-01-0216.

[102] Sokolov A., Glad T., (1999) - Identifiability of turbocharged IC engine models, SAE Technical Paper 1999-01-0216.

[103] Sorenson S. C., Hendrick E., Magnusson S., Bertelsen A., (2005) - Compact and accurate turbocharger modelling for engine control,

SAE Technical Paper 2005-01-1942.

[104] Taghizadeh M., Ghaffari A., Najafi F., (2009) – Modeling and identification of a solenoid valve for PWM control applications. Comptes Rendus Mecanique, 337, 131-140.

[105] Tanner F. X., Reitz R. D., (1999) - Scaling aspects of the characteristic time combustion model in the simulation of Diesel engines, SAE Technical Paper 1999-01-1175.

[106] Taylor E. S., (1974) - Dimensional analysis for engineers. Clarendon Press, Oxford.

[107] Theotokatos G., Kyrtatos N.P., (2001) - Diesel engine transient operation with turbocharger compressor surging, SAE Technical Paper 2001-01-1241.

[108] Thomasson A., Eriksson L., (2009) - Model-based throttle control using static compensators and IMC based PID-design. IFAC Workshop on Engine and Powertrain Control, Simulation and Modeling.

[109] Thomasson A., Eriksson L., Leufvén O., Andersson P., (2009) - Wastegate actuator modeling and model-based boost pressure control. IFAC Workshop on Engine and Powertrain Control, Simulation and Modeling.

[110] Thomasson A., Leufvén O., Criscuolo I., Eriksson L., (in press) - Modeling and validation of a boost pressure actuation system for a series sequentially turbocharged SI engine, Control Engineer Practice, Elsevier.

[111] Tirnovan R., Giurgea S., Miraoui A., Cirrincione M., (2008) - Surrogate modeling of compressor characteristics for fuel-cell applications, Applied Energy 85, 394–403.

[112] Ward-Smith A.J., (1979) - Critical flowmetering: the characteristics of cylindrical nozzles with sharp upstream edges, Int. J. of Heat and Fluid Flow, 1(3), 123-132.

[113] Watson N., (1980) - A combustion correlation for Diesel engine simulation, SAE Technical Paper 800029.

[114] Watson N., Janota M. S., (1982) - Turbocharging the internal combustion engine, MacMillan London.

[115] White F.M., (2005) - Fluid mechanics, McGraw-Hill.

[116] Yang M., Zheng X., Zhang Y., Li Z., (2008) - Improved

performance model of turbocharger centrifugal compressor, Proceedings of ASME Turbo Expo, Berlin, Germany.

[117] Ye N., Scavarda S., Betemps M., Jutard A., (1992) - Models of a pneumatic PWM solenoid valve for engineering applications, J. of Dynamic Systems, Measurement, and Control, 114, 680-688.

[118] Yoshizaki T., Nishida K. e Hiroyasu H., (1993) - Approach to low NO_x and smoke emission engines by using phenomenological simulation, SAE Technical Paper 930612.

[119] Zhang D., Di Liberti J. L., Cave M., (2010) - Blade thickness effect on impeller slip factor, Proceedings of ASME Turbo Expo, Glasgow, UK.